

ROLAND PEETZ

**Spectrum of
N=1 Super Yang Mills Theory
on the Lattice with a
Light Gluino**

2003

This version of the thesis differs slightly from the official document. Typos are corrected while results and conclusions are unchanged.

THEORETISCHE PHYSIK

**Spectrum of
N=1 Super Yang Mills Theory
on the Lattice with a
Light Gluino**

Inaugural-Dissertation
zur Erlangung des Doktorgrades
der Naturwissenschaften im Fachbereich Physik
der Mathematisch-Naturwissenschaftlichen Fakultät
der Westfälischen Wilhelms-Universität Münster

vorgelegt von
Roland Peetz
aus Wrexham

2003

Dekan:	Prof. Dr. H. Zacharias
Erster Gutachter:	Prof. Dr. G. Münster
Zweiter Gutachter:	Prof. Dr. M. Stingl
Tag der mündlichen Prüfungen:
Tag der Promotion:

Contents

1	Introduction	1
1.1	Why Supersymmetry?	1
1.2	Why on the Lattice?	4
2	The Physics of N=1 Super Yang Mills Theory	6
2.1	N=1 SYM Theory	6
2.1.1	Non-Zero Gluino Mass	10
2.1.2	Ward Identities	11
2.2	Low Energy Effective Action	12
3	The Numerics of N=1 Super-Yang-Mills Theory	14
3.1	Simulating SUSY on the Lattice	14
3.1.1	The $SU(2)$, $N = 1$ SYM Lattice Action	15
3.1.2	The TSMB Algorithm	18
3.2	Measuring Observables	22
3.2.1	Autocorrelation Times	23
3.2.2	Jackknife Error Estimation	24
3.3	String Tension σ and Sommer Scale R_0	25

3.4	Obtaining Masses of States	27
3.4.1	Fermionic Correlators	29
3.4.2	Glueballs	29
3.4.3	Gluino-Glue Bound States	31
3.4.4	Adjoint Mesons	32
3.5	Matrix Inversion Methods	33
3.5.1	Volume Source Technique	34
3.5.2	Stochastic Estimators	38
3.6	Ward Identities	40
3.7	The Massless Gluino Limit	43
4	Analysis and Results	45
4.1	Simulation Details	45
4.2	Computational Results	48
4.2.1	SET Performance	48
4.2.2	VST Error Analysis	51
4.3	Static Potential	54
4.4	Masses	55
4.4.1	Details of Mass Fits	55
4.4.2	Gluino-Glue Bound States	57
4.4.3	Adjoint Mesons	68
4.4.4	Glueballs	77
4.5	Ward Identities	83

4.6	The Massless Gluino Limit	86
4.6.1	Critical Hopping Parameter from Ward Identities	86
4.6.2	Critical Hopping Parameter from OZI Arguments	88
4.7	Finite Volume Effects	89
4.8	Summary and Discussion	93
5	Conclusions and Outlook	96
A	Conventions and Methods	99
A.1	Gamma Matrices	99
A.2	Majorana Fermions	100
A.3	Smearing Techniques	101
A.4	Combining Estimates	102
B	Overview of Spectrum Results	103
	References	104

Chapter 1

Introduction

In this thesis we study the $N = 1$ supersymmetric Yang Mills theory on the lattice. Supersymmetry extends the symmetries of the Standard Model of elementary particles to include a symmetry between fermions and bosons.

This introductory chapter will first make the case of why one should study supersymmetric theories at all, despite the fact that to this date the existence of supersymmetric partners of the usual particles has not been verified in accelerator experiments. We will then outline the reasons for a lattice investigation. Finally we will give an overview of the structure of this study.

1.1 Why Supersymmetry?

There is a great amount of interest in supersymmetric theories. The reasons for the apparent mismatch to its experimental status are numerous.

To begin with, it has to be clearly stated that the Standard Model (SM) currently faces only two significant challenges from experiment. One, somewhat unrelated to supersymmetry (SUSY), is the existence of dark matter. Up to now there is no clear way how to include any such, possibly only gravitationally interacting fields, in the Standard Model. The second, more exciting experimental challenge in the context of SUSY are the by now famous results from the experiment E821 at the Brookhaven National Laboratory measuring the anomalous magnetic moment of the muon. There is a discrepancy between prediction from theory, i. e. the SM, and the experimental value. However, there still remain uncertainties in the corresponding theoretical calculation, which draws on other experimentally determined input parameters. On some of these the accuracy is not yet sufficient. So the jury still has to decide, whether the SM falsely predicts the outcome of that experiment. Therefore one cannot argue the failure of the

SM on experimental grounds (yet).

Nevertheless, for all the sweeping success the Standard Model has enjoyed, it has several theoretical shortcomings. In some of these cases, supersymmetry is the only proposed solution that has not been ruled out yet. We will give a quick overview of the most important problems.

1. The Standard Model is based on the product of three gauge groups, $SU(3) \times SU(2) \times U(1)$, each with separate gauge coupling. It gives no apparent explanation for the fact that only the electroweak sector is chiral. Also, all particles have quantized charges, multiples of the electric charge $e/3$. Strongly related to this question is the cancellation of anomalies. Possible explanations of these properties can be found by studying *Grand Unified Theories* (GUTs), where the above product of groups is a subgroup of a larger group and the need arises to impose constraints on the values of charges. It turns out that simply taking gauge theories with larger groups such as $SU(5)$ is not a sufficient condition to unify the Standard Model. One needs further constraints, such as SUSY, to make the couplings actually match into a unified one at a higher scale.

2. Another intriguing mystery of the SM is the family structure of fermions. In the low energy regime, most terrestrial matter can be constructed from the first family (ν_e, e^-, u, d). However, in cosmic radiation and especially in high-energy laboratory experiments, two more families with successively higher mass have been shown to exist: (ν_μ, μ^-, c, s) and (ν_τ, τ^-, t, b). The SM gives no explanation for their existence nor does it predict any of the masses and consequently why the members of one family are consistently heavier than the other, on a range that spans at least eleven orders of magnitude ($m_{\nu_e} \lesssim 0.28 \text{ eV}$, $m_t = 174.3 \text{ GeV}$).

3. From considerations of consistency of the SM, one expects the mass of the until now unobserved Higgs particle to be similar to the mass of the W boson, $m_H \sim \mathcal{O}(m_W \approx 10^2 \text{ GeV})$. Additionally, from constraints imposed by theory and laboratory experiments one obtains an upper limit on m_H of $\approx 1 \text{ TeV}$. Unfortunately though, in the SM the bare Higgs mass receives quadratically divergent corrections from loop diagrams with heavy fermions, such that

$$m_H^2 = m_{H,\text{bare}}^2 + \mathcal{O}(\lambda, g^2, h^2)\Lambda^2$$

where Λ is the next higher scale in the theory. The next scale on offer currently would be either that of gravitation (if there is no GUT), such that Λ is of the Planck scale $m_P = G_N^{-\frac{1}{2}} \sim 10^{19} \text{ GeV}$ or that of a GUT-scale, where one expects Λ to be of order of the unification scale, $m_X \sim 10^{14} \text{ GeV}$. So, the natural scale of m_H is $\mathcal{O}(\Lambda)$ which is much higher than the expected value. For this to work, the parameter in front of Λ would have to be extremely finely tuned, in the case of the Planck scale up to 30 decimal places.

To this problem, up to recently [1], supersymmetry was the only viable answer [2]

which would protect the Higgs from receiving renormalization by symmetry-induced cancellations.

4. A second fine tuning problem is the so-called *strong CP problem*. It is entirely possible to add a $\frac{\theta}{32\pi^2}g_s^2 F\tilde{F}$ to the QCD Lagrangian. This extra term breaks \mathcal{P}, \mathcal{T} , and \mathcal{CP} symmetry. Adding this term would lead to a non-zero value for the dipole moment d_N of the neutron. The current experimental upper limit on d_N constrains θ to $|\theta| < 6 \times 10^{-10}$ [3]. Therefore the question is, why θ should be so small, since CP breaking in the weak sector causes it to receive additive renormalization of $\mathcal{O}(10^{-3})$. Hence, one is again faced with an apparently contrived fine tuning problem in order to cancel these corrections against the bare value, which one could assume to be zero. The solution is not well understood. An elegant solution, a massless up-quark [4], currently, does not seem to be the most probable [5].

5. Finally, gravity cannot fundamentally be unified with the other interactions of the standard model. Although it is possible to study quantum field theories on a curved space time (classical general relativity), it is far from obvious how to unify or even merely connect a quantized version of gravity with the standard model. In this context, a second related problem is the cosmological constant, the energy of the vacuum. The energy density calculated by invoking spontaneous symmetry breaking in the SM is 50 orders higher than the observational limit. Yet again, this necessitates excessive fine tuning between generated and bare pieces, which have, a priori, no reason to be related to each other at all. The most elegant solutions to this problem are supergravity theories [2], in which global supersymmetry is promoted to a local symmetry. Renormalizability requirements and the cosmological problem seem to make superstring theories necessary though [6]. Nevertheless these rely on supersymmetry as an essential ingredient.

Finally, one can invoke elegance and esthetics as the often successful guides in theoretical physics, rendering SUSY worthy of study. Haag, Lopuszanski and Sohnius showed in 1974 that the supersymmetry algebra constitutes the only possible non-trivial generalization involving the Poincaré and internal symmetry Lie algebra [7].

In conclusion, SUSY is a strong, if not the leading contender of Standard Model extensions. It is therefore important to study supersymmetric theories with respect to the concrete predictions they make. To this end, the phenomenologically relevant variants have $N = 1$ supercharges [8]. These types, such as the minimally supersymmetric standard model (MSSM), are most interesting, especially with softly broken supersymmetry in the low energy regime, which would be the world we live in. The simplest of these is the $N = 1$ Super Yang Mills theory, which includes the gluons as the bosons of QCD and massless gluinos as their supersymmetric partners. Several non-perturbative assumptions and predictions from analytical calculations are available. From its sim-

ilarity to QCD, color confinement and the spontaneous breaking of chiral symmetry are expected. Important questions include the (non-) existence of a SUSY anomaly and the implications of softly broken SUSY by a massive gluino. A problem open for debate is still the exact breaking mechanism of SUSY. Clarifications on the possibility of spontaneous SUSY breaking are needed. Finally one would like to know what the spectrum of lightest particles is. Predictions are available [9, 10], but an independent check is desirable.

1.2 Why on the Lattice?

Since K. G. Wilson introduced his formulation of QCD on the lattice [11], the field of computational physics has become an industry of its own in modern high energy physics. It is unique in the sense that by performing first principles simulations one can calculate quantities independently from analytical calculations and from experiments. It has delivered important insight into our understanding of the quantum field theories that govern the standard model. Furthermore, since physicists are in full control of the parameters of the computer simulation, it allows the creation of isolated testbeds not found in nature and therefore the independent study of problems.

One of its theoretically most important features is that the lattice is the only known non-perturbative regulator for quantum field theories. Its importance is appreciated if one considers QCD in the low energy regime. Here the coupling becomes large and therefore a meaningful definition of the theory in terms of a perturbation series in the coupling ceases to exist. Nevertheless, the non-perturbative dynamics, such as confinement, are rich and essential to the theory of QCD. So the lack of analytical accessibility to that part of field theories has been largely compensated by lattice field theory.

Also recently, a serious theoretical drawback of lattice gauge theory, the explicit breaking of chiral symmetry in simulations, has been resolved [12, 13], unfortunately at the price of dramatically increasing the computational demands of the simulation. Through these related methods, domain wall fermions and overlap fermions, the largest bottleneck is nevertheless mainly practical: the ever present lack of sufficient CPU power.

However, the success of lattice gauge theory up to now has been remarkable. It has allowed the calculation of, for example, hadronic matrix elements, experimentally unaccessible quark and hadron masses, parts of the phase diagram of QCD, the study of the role of confinement in non-Abelian gauge theories and also the study of the electroweak sector or Higgs models.

Given the interest in the non-perturbative features of supersymmetric theories and the success of the lattice method, it is therefore natural to consider the possibilities of their combination. This has been done by the “DESY-Münster-Roma-Collaboration”. The Curci-Veneziano approach [14] was used which breaks SUSY explicitly on the lattice by using Wilson fermions, but fine tuning of the input fermion mass of the simulation

lets the renormalized mass approach zero. The two step multibosonic algorithm [15] has proven to be a suitable algorithm to simulate light fermions at reasonable cost and stability. So far the main focus of the project has been

- algorithmic studies [15, 17, 18]
- the investigation of the lattice SUSY Ward identities [19, 20, 21]
- spectrum calculations [18, 19, 22, 23]
- chiral symmetry breaking and confinement studies [18, 24]

This thesis represents the continuation of the “SUSY on the lattice” project. We give more accurate results on the spectrum by using larger lattices and lighter gluinos to alleviate some of the systematics effects in the previous results. We will show, that the lattice spectrum is far from being well understood.

The thesis is organized as follows:

- Chapter 2 will review the physics of the $N = 1$ Super Yang Mills theory relevant to us. We will turn our attention to the low energy regime via the effective model by Farrar et al. [10] and give an overview of its predictions with respect to the particle spectrum. The verification of the underlying assumptions and the predictions they produce constitutes the rationale for this thesis.
- Chapter 3 considers the numerical aspects of formulating the model on the lattice. We will briefly explain the algorithm and concentrate on the methods of extracting the relevant masses. A short exposition on calculating the supersymmetric Ward-Identities is also given.
- Chapter 4 presents the numerical results from this study. These include characterization of the ensembles used, algorithmic parameters such as autocorrelations, the spectrum of lightest particles, renormalization factors and computational results.
- Chapter 5, as might be expected, summarizes the results and gives an outlook on viable directions for future research.
- The appendices list issues not immediately relevant to the topics discussed, but nevertheless too important to omit. These mostly include technical details, conventions and notations.

The computational work for this thesis was carried out on the Cray T3E and IBM Regatta at NIC, Jülich, the SunFire-SMP-Cluster at RWTH Aachen and the Linux-PC-cluster at the University of Münster. Partial results were presented at the conferences *Lattice 2001* in Berlin [20] and *Lattice 2002* in Boston [23].

Chapter 2

The Physics of N=1 Super Yang Mills Theory

This chapter will give a brief overview of the model in the continuum. We will first introduce the supersymmetric Yang Mills action in the superfield formalism, write it out in its component fields and verify that it is indeed invariant up to total divergence under supersymmetric transformations. From there on we will investigate the consequences of a non-zero gluino mass and then concentrate on formulating the SUSY-Ward identities. We will then review the low energy features of this model using the effective action approach following the ideas of [14] and finally see what predictions can be extracted from the model, mainly concerning the spectrum of particles.

2.1 N=1 SYM Theory

In four dimensions, one arrives at the simplest SUSY-invariant theory by explicitly extending the Poincaré Lie algebra to become a \mathbb{Z}_2 -graded algebra by adding a Majorana spinor charge with components Q_a , $a = 1, \dots, 4$. Extended ($N > 1$)-supersymmetry can be formulated by adding N Majorana charges. We will confine ourselves to $N = 1$ here, since this is the phenomenologically relevant case and the topic of this thesis. Furthermore, in four dimensions, it is currently the only model viable for a lattice simulation. So for this case, the regular Poincaré algebra becomes the following super-

Poincaré algebra:

$$\begin{aligned}
[P^\mu, P^\nu] &= 0 \\
[P^\mu, M^{\rho\sigma}] &= i(g^{\mu\rho}P^\sigma - g^{\mu\sigma}P^\rho) \\
[M^{\mu\nu}, M^{\rho\sigma}] &= -i(g^{\mu\rho}M^{\nu\sigma} - g^{\mu\sigma}M^{\nu\rho} - g^{\nu\rho}M^{\mu\sigma} + g^{\nu\sigma}M^{\mu\rho}) \quad (2.1) \\
[Q_a, P^\mu] = [\bar{Q}_a, P^\mu] &= 0 \\
[Q_a, M^{\mu\nu}] &= \sigma_{ab}^{\mu\nu}Q_b \\
\{Q_a, \bar{Q}_b\} &= 2\gamma_{ab}^\mu P_\mu \quad (2.2)
\end{aligned}$$

where the P^μ and $M^{\mu\nu}$ s are the generators of displacement and homogenous Lorentz-transformations of space-time, i.e. (2.1) is the regular Poincaré algebra extended by (2.2). Since Q is a Majorana spinor, it obeys the relation

$$Q = Q^c = C\bar{Q}^T \quad (2.3)$$

with the charge conjugation matrix C (please refer to the appendix for γ -matrix notations). In the literature, fermionic degrees of freedom are commonly expressed in terms of Weyl spinors. We will use both notations freely, remembering that a Majorana spinor can be assembled from two Weyl spinors:

$$Q_a = \begin{pmatrix} \theta_A \\ \bar{\theta}^{\dot{A}} \end{pmatrix}. \quad (2.4)$$

Through the introduction of superspace as Minkowski space with the fermionic extension of Weyl spinor variables $(\theta, \bar{\theta})$ and superfields acting on the superspace, one arrives at reducible representations of the algebra. However, to get irreducible representations one has to impose additional covariant constraints, such as

$$\bar{D}_{\dot{A}}\mathcal{F} = 0, \quad (2.5)$$

$$\text{or } D_A\mathcal{F} = 0, \quad (2.6)$$

$$\text{or } \mathcal{F} = \mathcal{F}^\dagger, \quad (2.7)$$

where \mathcal{F} is a generic superfield $\mathcal{F} = \mathcal{F}(x, \theta, \bar{\theta})$ and D is the superspace derivative obeying

$$\bar{D}_{\dot{A}} = -\frac{\partial}{\partial\bar{\theta}^{\dot{A}}} + i(\tilde{\sigma}^\mu\theta)_{\dot{A}}\partial_\mu, \quad D_A = \frac{\partial}{\partial\theta^A} + i(\sigma^\mu\bar{\theta})_A\partial_\mu \quad (2.8)$$

It acts on the Minkowski component x_μ of superspace and its fermionic components $(\theta, \bar{\theta})$. In passing, we define the Pauli matrix vector $\tilde{\sigma}^\mu = (\mathbf{1}, -\sigma^1, -\sigma^2, -\sigma^3)$. The resulting fields are labeled chiral (2.5), anti-chiral (2.6) and vector (2.7) superfields respectively. In terms of these fields, the most general supersymmetric Lagrangian one can write down is

$$\begin{aligned}
\mathcal{L} &= \frac{1}{4g^2}\text{Tr}\{(W^AW_A)_F + (\bar{W}_{\dot{A}}\bar{W}^{\dot{A}})_F\} \\
&\quad + (\Phi^\dagger e^V\Phi)_D + \left(\frac{1}{2}m_{ij}\Phi_i\Phi_j + \frac{1}{2}g_{ijk}\Phi_i\Phi_j\Phi_k\right)_F. \quad (2.9)
\end{aligned}$$

Several explanations are necessary here: Φ is a chiral superfield, Φ^\dagger an anti-chiral and $W_A = W_A(x, \theta, \bar{\theta})$ is the spinorial field strength

$$W_A = -\frac{1}{4}(\bar{D}\bar{D})e^{-V}D_Ae^V \quad (2.10)$$

constructed from the vector superfield $V = V(x, \theta, \bar{\theta})$. The subscripts $(\dots)_D$ and $(\dots)_F$ indicate the selection of the highest non-zero component of the corresponding superfield with respect to the expansion in $(\theta, \bar{\theta})$, so $(\dots)_F = (\dots)|_{\theta\theta\bar{\theta}\bar{\theta}}$ in the case of vector superfields and $(\dots)_D = (\dots)|_{\theta\theta y \rightarrow x}$ in the case of chiral superfields. These transform under SUSY transformations as a total divergence and leave according to Gauss' law the integral

$$\mathcal{S} = \int d^4x \mathcal{L} \quad (2.11)$$

and therefore the action and the physics it describes invariant. This is the behavior we are searching for.

From here on we will concentrate on the Yang-Mills part in eqn. (2.9) and neglect the matter fields described by the chiral superfields Φ_i . If we expand the vector superfield into its components in the Wess-Zumino-gauge

$$V_{WZ}(x, \theta, \bar{\theta}) = \theta\sigma^\mu\bar{\theta}A_\mu(x) + i(\theta\theta)\bar{\theta}\bar{\lambda}_W(x) - i(\bar{\theta}\bar{\theta})\theta\lambda_W(x) + \frac{1}{2}(\theta\theta)(\bar{\theta}\bar{\theta})D(x), \quad (2.12)$$

we see its particle content:

$$\text{a spin 1 boson field} : A_\mu(x) = -igT^a A_\mu^a(x) \quad (2.13)$$

$$\text{a spin } \frac{1}{2} \text{ Weyl spinor field} : \lambda_W(x) = T^a \lambda_W^a(x) \quad (2.14)$$

$$\text{an auxiliary field} : D(x) \quad (2.15)$$

where the T^a are the generators of an $SU(N_c)$ gauge group, $a = 1, \dots, N_c^2 - 1$. One can thus rewrite that part of the Lagrangian in terms of the component fields

$$\mathcal{L} = -\frac{1}{4}F_{\mu\nu}^a F^{a,\mu\nu} + \frac{i}{2}\lambda_W^a \sigma_\mu (D^\mu \bar{\lambda}_W)^a - \frac{i}{2}(D_\mu \bar{\lambda}_W)^a \tilde{\sigma}^\mu \lambda_W^a + \frac{1}{2}D^a D^a \quad (2.16)$$

with the regular gluonic field strength

$$F_{\mu\nu} = \partial_\mu A_\nu - \partial_\nu A_\mu + [A_\mu, A_\nu] \quad (2.17)$$

and the covariant derivative in the adjoint representation

$$(D_\mu \bar{\lambda}_W) = \partial_\mu \bar{\lambda}_W + [A_\mu, \bar{\lambda}_W]. \quad (2.18)$$

Since the auxiliary field $D^a(x)$ has no kinetic term and is therefore uninteresting for the dynamics of the theory, it is integrated out. Finally we rotate (2.16) from Minkowski to Euclidean space and rewrite the fermionic part with massless Majorana fermions

(*gluinos*) in the adjoint representation of $SU(N)$: $\lambda = ((\lambda_W)_A, (\bar{\lambda}_W)^{\dot{A}})$ to arrive at the on-shell Lagrangian of $N = 1$ Super Yang Mills theory:

$$\mathcal{L}_{SYM} = \frac{1}{4} F_{\mu\nu}^a(x) F_{\mu\nu}^a(x) + \frac{1}{2} \bar{\lambda}^a(x) \gamma_\mu D_\mu \lambda^a(x) . \quad (2.19)$$

This will be the basis of our study. The observant reader will have noticed that this Lagrangian looks suspiciously like QCD:

$$\mathcal{L}_{QCD} = \frac{1}{4} F_{\mu\nu}^a(x) F_{\mu\nu}^a(x) + \bar{q}^a(x) \gamma_\mu D_\mu q^a(x) . \quad (2.20)$$

The difference is that in QCD the fermions $q(x)$ (*quarks*) are Dirac fermions with 4 degrees of freedom and they lie in the fundamental representation of the gauge group $SU(3)$ as opposed to the Majorana nature of the gluinos which transform according to the adjoint representation. Nevertheless, the similarity will be heavily drawn upon when transferring the theory to the lattice.

From its explicit construction it is expected that the action

$$\mathcal{S}_{SYM} = \int d^4x \left\{ \frac{1}{4} F_{\mu\nu}^a(x) F_{\mu\nu}^a(x) + \frac{1}{2} \bar{\lambda}^a(x) \gamma_\mu D_\mu \lambda^a(x) \right\} \quad (2.21)$$

is invariant under (global) supersymmetric transformations. Written in the component fields, the supersymmetric variations are

$$\delta A_\mu(x) = -2g \bar{\lambda}(x) \gamma_\mu \varepsilon \quad (2.22)$$

$$\delta \lambda(x) = -\frac{i}{g} \sigma_{\rho\tau} F_{\rho\tau}(x) \varepsilon \quad (2.23)$$

where ε is an infinitesimal continuous Grassmann parameter vanishing outside some bounded region \mathcal{M} . Note the explicit expression of the boson ($A_\mu, F_{\mu\nu}$) to fermion (λ) symmetry in the equations. Plugging (2.22) and (2.23) into the Lagrangian (2.19) and doing a considerable amount of algebra one arrives at

$$\delta \mathcal{L}(x) = \partial_\mu \left(\frac{4}{g} \bar{\lambda}^a(x) F_{\mu\nu}^a(x) \gamma_\nu + \frac{i}{g} \bar{\lambda}^a(x) F_{\rho\tau}^a(x) \gamma_\mu \sigma_{\rho\tau} \right) \bar{\varepsilon} \quad (2.24)$$

confirming that the Lagrangian truly only transforms as a divergence. This gives rise to the construction of the spin- $\frac{3}{2}$ super-current via Noether's theorem:

$$S_\mu = \frac{4}{g} \bar{\lambda}^a(x) F_{\mu\nu}^a(x) \gamma_\nu + \frac{i}{g} \bar{\lambda}^a(x) F_{\rho\tau}^a(x) \gamma_\mu \sigma_{\rho\tau} \quad (2.25)$$

$$= \frac{i}{g} \bar{\lambda}^a(x) F_{\rho\tau}^a(x) \sigma_{\rho\tau} \gamma_\mu \quad (2.26)$$

where again between (2.25) and (2.26) lies a lengthy calculation. This current will be considered later in the lattice formulation.

Also drawing further on the analogy with QCD, (2.19) is invariant under a global $U_A(1)$ rotation¹

$$\lambda' = e^{-i\phi\gamma_5}\lambda, \quad \bar{\lambda}' = \bar{\lambda}e^{-i\phi\gamma_5}. \quad (2.27)$$

This coincides with the so-called R -symmetry of supersymmetry. It is broken by the anomaly, again similar to QCD. The associated current $J_\mu^5 \equiv \bar{\lambda}\gamma_\mu\gamma_5\lambda$ satisfies the anomalous Ward identity

$$\partial^\mu J_\mu^5 = \frac{N_c g^2}{32\pi^2} \epsilon^{\mu\nu\rho\sigma} F_{\mu\nu}^a F_{\rho\sigma}^a. \quad (2.28)$$

The anomaly, however, leaves a residual \mathbb{Z}_{2N_c} -symmetry of the transformation (2.27) with

$$\phi = \phi_k = \frac{k\pi}{N_c}, \quad k = 0, \dots, 2N_c - 1 \quad (2.29)$$

unbroken. The case is again analogous to QCD in that one expects the residual \mathbb{Z}_{2N_c} -symmetry to be spontaneously broken by a non-vanishing gluino condensate $\langle\lambda\lambda\rangle$ to the group \mathbb{Z}_2 .

2.1.1 Non-Zero Gluino Mass

Introducing a mass term for the gluino $m_{\tilde{g}}$ in the Lagrangian (2.19) breaks supersymmetry, albeit softly

$$\mathcal{L} = \mathcal{L}_{SYM} + m_{\tilde{g}}\bar{\lambda}\lambda. \quad (2.30)$$

Soft breaking of supersymmetry in this context means that the breaking vanishes sufficiently fast to retain the advantages of SUSY at high energies, especially the solution of the hierarchy problem. This is evident here, since one can readily approximate the gluino mass, which is not expected to be much larger than the weak scale, to be zero when approaching the unification scale. Note that this leaves the question of *exactly how* supersymmetry is broken in our world completely open. Historically, the concept of the soft breaking of supersymmetry was an essential ingredient in making supersymmetric theories' predictions at low energies compatible with our world [25].

Furthermore, the breaking pattern of the $U_A(1)$ -symmetry (2.27) implies the existence of a first order phase transition at $m_{\tilde{g}} = 0$. For $N_c = 2$ this means that two degenerate ground states exist which have opposite signs of the gaugino condensate $\langle\lambda\lambda\rangle$. Since the breaking is linear in $m_{\tilde{g}}$, these two ground-states coexist at $m_{\tilde{g}} = 0$. The $N_c > 2$ case is more involved.

¹Due to the Majorana nature of gluinos there is no $U(1)$ vector symmetry.

2.1.2 Ward Identities

The expectation value of any operator \mathcal{O} constructed from local field operators $\phi_i(x)$ can be formally calculated by

$$\langle \mathcal{O}(\{\phi_i(x)\}) \rangle = \mathcal{Z}[0]^{-1} \int \mathcal{D}[\phi] \mathcal{O}(\{\phi_i(x)\}) e^{-S[\phi]} \quad (2.31)$$

where we work in Euclidean space and define the partition function $\mathcal{Z}[J]$ to be

$$\mathcal{Z}[J] = \int \mathcal{D}[\phi] e^{-S[\phi] - K[J, \phi]} \quad (2.32)$$

with the generating functional $K[J, \phi] = \int d^4x \phi(x) J(x)$. $\mathcal{D}[\phi]$ in eqn. (2.31) denotes the usual Feynman path integral over all local fields $\phi_i(x)$.

The basic idea of Ward identities is that the expectation value of an operator should be insensitive to a variable change in the path integral under local SUSY transformations,

$$\langle \mathcal{O} \rangle = \langle \mathcal{O} \rangle_\varepsilon, \quad (2.33)$$

therefore assuming the invariance of the measure and the absence of a supersymmetric anomaly. Promoting the Grassmann parameter in equations (2.22) and (2.23) to be local, $\varepsilon \rightarrow \varepsilon(x)$,

$$\delta A_\mu(x) = -2g\bar{\lambda}(x)\gamma_\mu\varepsilon(x) \quad (2.34)$$

$$\delta\lambda(x) = -\frac{i}{g}\sigma_{\rho\tau}F_{\rho\tau}(x)\varepsilon(x) \quad (2.35)$$

and using the Leibnitz chain rule, we formally get

$$\langle \delta\mathcal{O} \rangle - \langle (\delta\mathcal{S})\mathcal{O} \rangle = 0. \quad (2.36)$$

We know $\delta\mathcal{S}$ to be the total divergence of (2.26), i.e.

$$\delta\mathcal{S} = \partial_\mu S_\mu = \partial_\mu \left(\frac{i}{g} \bar{\lambda}^a F_{\rho\tau} \sigma_{\rho\tau} \gamma_\mu \right). \quad (2.37)$$

With a local insertion operator $Q(y)$ the Ward identity then reads

$$\langle \partial_\mu S_\mu(x) Q(y) \rangle = 0, \quad (2.38)$$

where we further assumed that the product of operators \mathcal{O} is localized outside the domain \mathcal{M} of $\varepsilon(x)$, such that the variation $\delta\mathcal{O}$ vanishes. This implies $x \neq y$ in equation (2.38).

As pointed out, $m_{\bar{g}} \neq 0$ breaks the SUSY invariance. So in that case, the additional term in the Lagrangian $\mathcal{L}_m = m_{\bar{g}}(\bar{\lambda}\lambda)$ gives rise to an additional term in eqn. (2.36), labeled χ

$$\chi(x) = \frac{2i}{g} \sigma_{\rho\tau} F_{\rho\tau}^a(x) \lambda^a(x) \quad (2.39)$$

changing the Ward identity to

$$\langle \partial_\mu S_\mu(x) Q(y) \rangle - m_0 \langle \chi(x) Q(y) \rangle = 0 \quad (2.40)$$

where m_0 is the bare gluino mass.

2.2 Low Energy Effective Action

It is natural to assume that at low energies, the degrees of freedom relevant to the dynamics of a theory are different from those at high energies. This is illustrated in the argument made above, that the standard model is believed to exhibit a higher degree of symmetry at some higher energy scale. This implies that the fundamental degrees of freedom at that scale are not seen in our world. Rather, what we currently see in our experiments, we call the “elementary” interactions of the SM. In other words it is believed that the SM is an effective theory of a more unified theory.

So if we are interested in the low energy features of the above theory (2.19), we are naturally led to formulate it as an effective theory which consists of composite fields, but nevertheless retains the important symmetries of the more fundamental theory. This is the approach taken in [9] and developed further in [10].

The effective action is a functional of the superfield S , where

$$S \equiv \frac{\beta(g)}{2g} \langle \text{Tr} W^\alpha W_\alpha \rangle_Q \equiv A(y) + \sqrt{2} \theta \lambda_W(y) + \theta^2 F(y), \quad (2.41)$$

where $\beta(g)$ stands for SYM β -function which is known exactly [26]. In terms of S , the effective Lagrangian proposed in [10], respecting the underlying symmetries and the anomaly structure, has the form

$$\mathcal{L}_{VY} = \alpha^{-1} (S^\dagger S)_D^{\frac{1}{3}} + \gamma \left[(S \log \frac{S}{\mu^3} - S)_F + \text{h.c.} \right] + \delta^{-1} \left(-\frac{U^2}{(S^\dagger S)^{\frac{1}{3}}} \right)_D \quad (2.42)$$

where α, γ, δ are arbitrary positive constants, μ is the dimensionally transmuted scale of the model and U is a real tensor superfield.

Studying the potential of the model one finds that the physical eigenstates fall into two different multiplets. Neither of them contain pure gluino-gluino, gluino-gluon or gluon-gluon bound states. Instead, they are mixed states of these composites, while the mixing occurs between the different multiplets. The contents of the lighter multiplet [10], which appears in addition to the regular multiplet of [9], is

- a scalar meson, which for small mixing becomes the 0^{++} glueball,

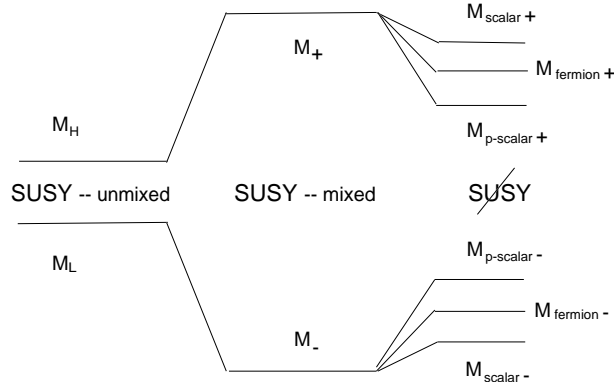


Figure 2.1: Qualitative behavior of the mass spectrum when passing from SYM to the softly broken model. [10]

- a pseudo-scalar state, which is identified as the 0^{-+} glueball for small mixing ,
- a mixed fermionic gluino-gluon state,

while the heavier set of states contains

- a pseudo-scalar meson, which without mixing reduces to the 0^{-+} gluino-gluino bound state, in analogy to QCD, called the $a-\eta'$,
- a scalar meson, that without mixing is a 0^{++} gluino-gluino, in analogy again to QCD, called the $a-f_0$,
- a mixed fermionic gluino-gluon bound state.

The interesting feature to observe here is that through the introduction of the gluino mass term which breaks SUSY softly, the masses, from being degenerate in the multiplets, split into the case which is relevant to us (see Figure 2.1).

Chapter 3

The Numerics of N=1 Super-Yang-Mills Theory

Since we now have a picture of the theory in the continuum, we turn to its formulation on the lattice. Following the Curci and Veneziano approach [14], we will use Wilson fermions to write down the lattice action. We will give an outline of the two-step-multi-boson algorithm (TSMB), describe how we measure the masses of the states and explain how we approach the Ward identities. Also a few remarks on selected numerical techniques are given.

3.1 Simulating SUSY on the Lattice

At first sight, the task of putting SUSY on the lattice seems daunting. The most striking reason is easily appreciated by looking at equation (2.2), namely that

$$\{Q_a, \bar{Q}_b\} = 2\gamma_{ab}^\mu P_\mu .$$

The anti-commutator of the SUSY charges closes with the four-momentum P^μ , the generator of infinitesimal translations. Since there are no infinitesimal translations on the lattice, Poincaré invariance is broken and therefore SUSY is fundamentally broken. Furthermore, SYM is a theory that requires an exact balance of massless bosonic and fermionic degrees of freedom. Until recently [12, 13] a formulation of exactly massless fermions on the lattice was not believed to exist [27].

To address these problems, we follow Curci and Veneziano [14]. Here, SUSY and chiral symmetry is explicitly broken using Wilson's formulation of lattice gauge theory [11]. In this formulation, the gluino acquires a mass which is subject to additive renormalization. The strategy is to fine tune the simulation input parameter of the bare gluino

mass, such that the renormalized mass is close to zero. This limit of zero renormalized gluino mass coincides with the chiral limit in which, when performed, the continuum limit leads to a supersymmetrically invariant theory. However, if we set the coupling β to be in the scaling region, the features of the underlying supersymmetric theory should become apparent in the simulation, for example, by letting the particle spectrum split up from its multiplet form linearly in m_0 .

The possibility of defining the chiral and SUSY limit lies in the Ward identities. When approaching this limit, the additional renormalized SUSY breaking terms vanish and the Ward identities should appear as in their continuum form.

3.1.1 The $SU(2)$, $N = 1$ SYM Lattice Action

The lattice action consists of a gauge and a fermion part

$$S_{lat} = S_g + S_f . \quad (3.1)$$

The gauge field action S_g is the standard action made up from plaquettes of links. A link

$$U_\mu(x) = e^{-aA_\mu(x)} \in SU(N_c) \quad (3.2)$$

is the lattice version of the μ 'th component of the parallel transporter $A_\mu(x)$ from the continuum, where a denotes the lattice spacing and $\mu \in \{0, 1, 2, 3\}$ the Euclidean space-time direction. The smallest gauge invariant object that can be constructed from links is a plaquette in the $\mu\nu$ -plane of the lattice

$$U_{\mu\nu}(x) = U_\nu^\dagger(x)U_\mu^\dagger(x + a\hat{\nu})U_\nu(x + a\hat{\mu})U_\mu(x) . \quad (3.3)$$

Since

$$U_{\mu\nu}(x) = e^{-a^2 G_{\mu\nu}} \quad \text{where} \quad G_{\mu\nu}(x) = F_{\mu\nu}(x) + \mathcal{O}(a^2), \quad (3.4)$$

the plaquette reduces to the regular gauge field strength

$$\text{Re Tr } U_{\mu\nu}(x) = N_c \text{Tr} \mathbf{1} + a^4 F_{\mu\nu}^2(x) + \mathcal{O}(a^5) . \quad (3.5)$$

Thus the gauge action can be written as the sum over all plaquettes

$$S_g[U] = \beta \sum_x \sum_{\mu\nu} \left[1 - \frac{1}{N_c} \text{Re Tr } U_{\mu\nu} \right], \quad (3.6)$$

where $\beta = \frac{2N_c}{g^2}$ for $U_\mu(x) \in SU(N_c)$ is the bare gauge coupling. From here on, we set $N_c = 2$.

The fermion action is more involved. A ‘naive’ discretization would result in $2^d = 16$ fermions on the lattice with equal and opposite chirality. This complies with the well-known Nielsen-Ninomiya theorem [27] which states that, under very general assumptions, it is not possible to formulate massless fermions on the lattice. Wilson solved the

problem [11] by giving the doublers a weight of $\mathcal{O}(a^{-1})$, which decouples them in the continuum limit completely from the theory. Only one fermion, the desired, survives. This method yields the fermion action

$$S_f[U, \bar{\lambda}, \lambda] = \frac{1}{2} \sum_x \bar{\lambda}(x) \lambda(x) + \frac{\kappa}{2} \sum_x \sum_\mu [\bar{\lambda}(x + \hat{\mu}) V_\mu(x) (r + \gamma_\mu) \lambda(x) + \bar{\lambda}(x) V_\mu^T(x) (r - \gamma_\mu) \lambda(x + \hat{\mu})] \quad (3.7)$$

with the Wilson parameter r , which we take to be 1, the hopping parameter $\kappa = (2m_0 + 8r)^{-1}$. We have also rescaled the fermion fields $\lambda \rightarrow \sqrt{\frac{1}{2\kappa}} \lambda$, here in the adjoint representation of the gauge group. This parameterization breaks chiral invariance by introducing a bare gluino mass $m_{\tilde{g},0} \propto \kappa^{-1}$. In order to simulate a massless or sufficiently light gluino, one needs to tune κ to a critical κ_c , such that the renormalized mass $m_{\tilde{g}} \rightarrow 0$. The required determination of κ_c will be explained below.

The above adjoint matrices are defined as

$$[V_\mu(x)]_{ab} \equiv 2\text{Tr}[U_\mu^\dagger(x) T^a U_\mu(x) T^b] = [V_\mu^*(x)]_{ab} = [V_\mu^T(x)]_{ab}^{-1}. \quad (3.8)$$

The trace acts on the color indices of the links in the fundamental representation $U_\mu(x)$. The generators T^a in the $SU(2)$ case are the Pauli matrices $T^a = \frac{1}{2}\tau^a$. Since we are dealing with Majorana fermions here, i.e.

$$\lambda = \lambda^c = \mathcal{C} \bar{\lambda}^T, \quad (3.9)$$

where \mathcal{C} is the charge conjugation matrix, there is a factor of $\frac{1}{2}$ in front of the sum in equation (3.7) when compared to the QCD action. If we now introduce the fermion matrix

$$Q_{y,x}[U] \equiv \delta_{yx} - \kappa \sum_\mu [\delta_{y,x+\hat{\mu}} (1 + \gamma_\mu) V_\mu(x) + \delta_{y+\hat{\mu}} (1 - \gamma_\mu) V_\mu^T(y)] , \quad (3.10)$$

we can write S_f more compactly as

$$S_f = \frac{1}{2} \sum_{xy} \bar{\lambda}(x) Q_{x,y} \lambda(y) \quad (3.11)$$

$$= \frac{1}{2} \sum_{xy} \lambda(x) \mathcal{C} Q_{x,y} \lambda(y) . \quad (3.12)$$

We note that the fermion matrix has the following symmetries:

$$Q^\dagger = \gamma_5 Q \gamma_5, \quad (3.13)$$

$$\mathcal{C} Q \mathcal{C} = Q^T, \quad (3.14)$$

$$\mathcal{C} \gamma_5 Q \gamma_5 \mathcal{C}^{-1} = Q^* . \quad (3.15)$$

Using equation (3.13) we can see, since $\det[\gamma_5 Q] = \det Q$, that

$$\det Q \in \mathbb{R} . \quad (3.16)$$

Furthermore, (3.14) and (3.15) show us after some algebra that $\mathcal{C}Q$ is antisymmetric, that its eigenvalues are doubly degenerate and that the fermion determinant is positive.

Since Grassmann variables cannot be formulated on a computer directly, they are integrated out and the result is written in terms of the fermion matrix Q , which is completely defined by the easily programmable link matrices $U_\mu(x)$ and its space time structure.

If we consider the case of regular Dirac fermions, where the fermionic variables ψ and $\bar{\psi}$ are independent, one gets

$$\int \mathcal{D}[\bar{\psi}, \psi] e^{-S_f} = \int \mathcal{D}[\bar{\psi}, \psi] e^{-\bar{\psi} Q \psi} = \det Q . \quad (3.17)$$

For the following it is instructive to construct the Majorana fields from a Dirac field:

$$\lambda^1 = \frac{1}{\sqrt{2}}(\psi + \mathcal{C}\bar{\psi}^T), \quad \lambda^2 = \frac{1}{\sqrt{2}}(-\psi + \mathcal{C}\bar{\psi}^T) \quad (3.18)$$

Writing down the analog to equation (3.11) with Dirac spinors, we have

$$S_f = \sum_{xy} \bar{\psi} Q \psi = \frac{1}{2} \sum_{k=1}^2 \sum_{xy} \bar{\lambda}^k Q \lambda^k . \quad (3.19)$$

So, integrating the fermions out as advertised above and noting the redundancy (3.9) in λ and $\bar{\lambda}$, we arrive at

$$\int \mathcal{D}[\bar{\psi}, \psi] e^{-\bar{\psi} Q \psi} = \det Q = \prod_{k=1}^2 \int \mathcal{D}[\lambda] e^{-\frac{1}{2} \bar{\lambda}^k Q \lambda^k} = \left(\int \mathcal{D}[\lambda] e^{-\frac{1}{2} \bar{\lambda} Q \lambda} \right)^2 . \quad (3.20)$$

Note here that the fermionic Feynman path integral for Majorana fields is only over $\mathcal{D}[\lambda]$ and not over $\mathcal{D}[\lambda, \bar{\lambda}]$. Putting the pieces together, we see that the $\det Q$ from Dirac fermions is the square of the result we really want:

$$\int \mathcal{D}[\lambda] e^{-S_f} = \int \mathcal{D}[\lambda] e^{-\frac{1}{2} \bar{\lambda} Q \lambda} = \pm \sqrt{\det Q} . \quad (3.21)$$

This relation leaves the sign on the right hand side undetermined. However, a unique definition of the path integral is given by

$$\int \mathcal{D}[\lambda] e^{-\frac{1}{2} \bar{\lambda} Q \lambda} = \int \mathcal{D}[\lambda] e^{-\frac{1}{2} \lambda \mathcal{M} \lambda} = \text{Pf}[\mathcal{M}] \quad (3.22)$$

where the complex antisymmetric matrix \mathcal{M} , defined as

$$\mathcal{M} = \mathcal{C}Q = -\mathcal{M}^T , \quad (3.23)$$

has the same determinant as Q . $\text{Pf}[\mathcal{M}]$ is the so-called *Pfaffian* of \mathcal{M} . Generally, the Pfaffian of a complex antisymmetric matrix of dimension $2N$ can be written as

$$\text{Pf}[\mathcal{M}] \equiv \frac{1}{N!2^N} \epsilon_{\alpha_1 \beta_1 \dots \alpha_N \beta_N} \mathcal{M}_{\alpha_1 \beta_1} \dots \mathcal{M}_{\alpha_N \beta_N} = \int \mathcal{D}[\phi_i] e^{-\frac{1}{2} \phi_\alpha \mathcal{M}_{\alpha\beta} \phi_\beta} \quad (3.24)$$

with $1 \leq \alpha, \beta \leq 2N$ and the totally antisymmetric unit tensor ϵ . The second relation indicates that the Pfaffian can be thought of as a Gaussian integral over Grassmann numbers, which is exactly the form we are interested in. As a side note it should be mentioned that the so-called Witten anomaly problem of the theory, not being defined due to the sign of $\pm\sqrt{\det Q}$ not being gauge invariant [28], does not apply here, since the quantity $\text{Pf}[\mathcal{M}]$ is inherently gauge invariant (see e.g. [19]).

With the formula (3.22), we can proceed to define the generating functional for the theory entirely in terms of the gauge fields U ,

$$\mathcal{Z}[J] = \int \mathcal{D}[U] \text{Pf}[\mathcal{M}[U]] e^{-S_g - \frac{1}{2} \sum_{x,y} J(x) \mathcal{M}^{-1}(x,y) J(y)}, \quad (3.25)$$

and write down expectation values of operators of fermion fields in the standard way of functional differentiation [29]:

$$\begin{aligned} \langle T\{\lambda(x_1) \dots \lambda(x_n) \bar{\lambda}(y_1) \dots \bar{\lambda}(y_n)\} \rangle_{\text{conn.}} &= \langle T\{\lambda(x_1) \dots \lambda(x_n) \lambda(y_1) \dots \lambda(y_n)\} \rangle_{\text{conn.}} \cdot \mathcal{C}^n \\ &= 2^n \left[\frac{\delta^{2n} \ln \mathcal{Z}[J]}{\delta J(x_1) \dots \delta J(x_n) \delta J(y_1) \dots \delta J(y_n)} \right] \cdot \mathcal{C}^n. \end{aligned} \quad (3.26)$$

The gluino propagator then is, for example,

$$\begin{aligned} \langle T\{\lambda(x) \bar{\lambda}(y)\} \rangle &= \langle T\{\lambda(x) \lambda(y)\} \rangle \cdot \mathcal{C} = 2 \left[\frac{\delta^2 \ln \mathcal{Z}[J]}{\delta J(x) \delta J(y)} \right] \cdot \mathcal{C} \\ &= \langle \mathcal{M}^{-1}(x, y) \rangle \cdot \mathcal{C} \\ &= \langle Q^{-1}[U] \rangle. \end{aligned} \quad (3.27)$$

For practical calculations with Majorana fermions it is important to remember that, in contrast to QCD or other theories with Dirac fermions, Wick contractions such as

$$\overline{\lambda(x) \lambda(y)} = \mathcal{M}_{xy}^{-1} = \overline{\bar{\lambda}(x) \bar{\lambda}(y)} \quad (3.28)$$

are allowed and yield a non-zero value.

3.1.2 The TSMB Algorithm

The method of performing simulations of lattice gauge theory on computers centers around the Monte Carlo generation of an ensemble of field configurations with a given equilibrium distribution of the theory. To extract physical information it suffices to produce a relatively small number of configurations and perform measurements on these, i.e. to sample only the important region of configuration space where the probability measure is strongly peaked. To use this method, one needs a positive probability measure to calculate the weight of a single configuration. In gauge theories with Wilson

fermions in the fundamental representation, this is given by

$$f(U) = e^{-\mathcal{S}_{eff}} = e^{-\mathcal{S}_g[U] - \mathcal{S}_f[U]}, \quad (3.29)$$

where $\mathcal{S}_f[U] = -\log [\det Q[U]]^{N_f}$. In our case of the SYM theory with the Curci-Veneziano action, the definition of an \mathcal{S}_{eff} is not as straightforward, since the measure would not be strictly positive (3.21). Here, $\mathcal{S}_f[U]$ is the Pfaffian of \mathcal{CM} . Since calculating the Pfaffian explicitly would lead to enormous storage and CPU requirements [16], the solution is to replace it with the positive square root of the regular determinant. In this case, an effective action can be derived as

$$\mathcal{S} = \beta \sum_{pl} \left[1 - \frac{1}{2} \text{ReTr } U_{pl} \right] + \frac{1}{2} \log \det Q[U]. \quad (3.30)$$

Due to the positivity of the measure, stochastic methods can now be applied to this part of the problem. Effectively, it gives us a theory with $N_f = \frac{1}{2}$ and a light fermion in the adjoint representation. The sign of $\text{Pf}[\mathcal{CM}]$ is then taken into account by reweighting the configurations in the measurement process by

$$\langle \mathcal{O} \rangle = \frac{\langle \mathcal{O} \text{ signPf}[\mathcal{M}] \rangle}{\langle \text{signPf}[\mathcal{M}] \rangle}. \quad (3.31)$$

So what is needed now is an algorithm that easily reproduces fractional powers of the fermion determinant and is capable of simulating at light fermion masses. The most suitable for this function is the two step multi boson algorithm (TSMB) [15]. It relies on the polynomial approximation

$$|\det Q|^{N_f} = [\det(Q^\dagger Q)]^{\frac{N_f}{2}} \approx \frac{1}{\det P_n(Q^\dagger Q)} \quad (3.32)$$

where the polynomial $P_n(x)$ satisfies

$$\lim_{n \rightarrow \infty} P_n(x) = x^{-\frac{N_f}{2}} \quad \text{for } x \in [\epsilon, \lambda], \quad (3.33)$$

where ϵ and λ delimit the interval of validity for the approximation. This interval, however, should cover the spectrum of eigenvalues of $Q^\dagger Q$

$$\epsilon \leq \min\{\text{spec}(Q^\dagger Q)\} \quad (3.34)$$

$$\lambda \geq \max\{\text{spec}(Q^\dagger Q)\}. \quad (3.35)$$

For convenience we define

$$\tilde{Q}^2 \equiv Q^\dagger Q \quad (3.36)$$

and proceed to write $P_n(\tilde{Q}^2)$ in its representation by roots z_j ($j \in \{1, \dots, n\}$) as a product of monomials

$$P_n(\tilde{Q}^2) = z_0 \prod_{j=1}^n (\tilde{Q}^2 - z_j). \quad (3.37)$$

Since the roots z_j come in complex conjugate pairs, an equivalent and manifestly positive form is

$$P_n(\tilde{Q}^2) = z_0 \prod_{j=1}^n \left[(\tilde{Q} - \mu_j)^2 + \nu_j^2 \right] = z_0 \prod_{j=1}^n \left[(\tilde{Q} - \rho_j^*)(\tilde{Q} - \rho_j) \right] \quad (3.38)$$

where we defined $\rho_j \equiv \mu_j + i\nu_j \equiv \sqrt{z_j}$ with $\nu_j > 0$. Every value of ν_j occurs twice and the corresponding μ_j 's have equal magnitude and opposite sign. Now we introduce local, complex boson (pseudo-fermion) fields $\Phi_j(x)$ and can finally write the determinant as a path integral over Φ 's

$$z_0 \prod_{j=1}^n \det \left[(\tilde{Q} - \rho_j^*)(\tilde{Q} - \rho_j) \right]^{-1} \\ \propto \int \mathcal{D}[\Phi] e^{-\sum_{j=1}^n \sum_{xy} \Phi_j^\dagger(y) [(\tilde{Q} - \rho_j^*)(\tilde{Q} - \rho_j)]_{yx} \Phi_j(x)}. \quad (3.39)$$

This form is known as the multi-boson representation of the fermion determinant. However, for any finite polynomial order n , simply updating the pseudo-fermion fields would not be exact and one would have to extrapolate any results to $n \rightarrow \infty$. Here the problem arises that at small fermion mass $m_{\tilde{g}}$ the condition-number $\frac{\lambda}{\epsilon}$ becomes $\mathcal{O}(10^4 - 10^6)$ in turn necessitating a polynomial order of $n \sim \mathcal{O}(10^3)$. This would lead to enormous storage and CPU requirements and additionally to very large autocorrelation times in the simulation. The key to this problem is to use a two-step approximation leading to the introduction of a second polynomial such that

$$\lim_{n_2 \rightarrow \infty} P_{n_1}^{(1)}(x) P_{n_2}^{(2)}(x) = x^{-\frac{N_f}{2}} \quad \text{for } x \in [\epsilon, \lambda]. \quad (3.40)$$

The idea is that $P_{n_1}^{(1)}(x)$ with a relatively low order n_1 can be a crude approximation to the function $x^{-\frac{N_f}{2}}$. This is used in a heat-bath and over-relaxation update sweep with the additional correction as a global accept/reject step (see [18] for details). The correction is obtained through noisy estimation by generating a complex Gaussian random vector η according to the distribution

$$\frac{e^{\eta^\dagger P_{n_2}^{(2)}(\tilde{Q}^2) \eta}}{\int \mathcal{D}[\eta] e^{\eta^\dagger P_{n_2}^{(2)}(\tilde{Q}^2) \eta}} \quad (3.41)$$

and accepting the newly produced field configuration $[U']$ (proposed via $P_{n_1}^{(1)}$) with probability

$$\min\{1, \omega(\eta, U' \leftarrow U)\} \quad (3.42)$$

where the probability measure is defined as

$$\omega(\eta, U' \leftarrow U) = \exp \left[-\eta^\dagger P_{n_2}^{(2)}(\tilde{Q}^2[U']) \eta + \eta^\dagger P_{n_2}^{(2)}(\tilde{Q}^2[U]) \eta \right] \quad (3.43)$$

ensuring detailed balance in the updating process. So now we would have an exact algorithm for fixed n_1 in the limit of $n_2 \rightarrow \infty$. In most cases of practical usage,

however, moderate values of n_2 already give errors which are negligible, when compared to the statistical fluctuations. Only in sporadic cases, when the smallest eigenvalue of the fermion matrix approaches the lower limit of approximation of the polynomial, a final correction must be performed. This can be achieved by the introduction of a third polynomial. So one would then fix, as above, n_1 to be of relatively low order, n_2 to be of high enough order to ensure a good quality Markov chain with the desired distribution and then finally reweight each field configuration while measuring observables according to

$$\lim_{n_3 \rightarrow \infty} P_{n_1}^{(1)}(x) P_{n_2}^{(2)}(x) P_{n_3}^{(3)}(x) = x^{-\frac{N_f}{2}} \quad \text{for } x \in [\epsilon', \lambda]. \quad (3.44)$$

In the limit of $n_3 \rightarrow \infty$ this procedure would be exact on every configuration. But $P_{n_3}^{(3)}$ can be obtained more easily up to a satisfactory order and precision through recurrence relations and by monitoring the changes in the values of the observable in question. So finally the measurement would have to be corrected by

$$\langle \mathcal{O} \rangle = \frac{\langle \mathcal{O} e^{\eta'^{\dagger} (1 - P_{n_3}^{(3)}(\tilde{Q}^2)) \eta'} \rangle_{U, \eta'}}{\langle e^{\eta'^{\dagger} (1 - P_{n_3}^{(3)}(\tilde{Q}^2)) \eta'} \rangle_{U, \eta'}} \quad (3.45)$$

where η' is a simple Gaussian noise vector distributed as

$$\frac{e^{-\eta'^{\dagger} \eta'}}{\int \mathcal{D}[\eta'] e^{-\eta'^{\dagger} \eta'}}. \quad (3.46)$$

In this reweighting step the sign of the Pfaffian can also be included. So then one has

$$\langle \mathcal{O} \rangle = \frac{\langle \mathcal{O} \text{signPf}[Q] e^{\eta'^{\dagger} (1 - P_{n_3}^{(3)}(\tilde{Q}^2)) \eta'} \rangle_{U, \eta'}}{\langle \text{signPf}[Q] e^{\eta'^{\dagger} (1 - P_{n_3}^{(3)}(\tilde{Q}^2)) \eta'} \rangle_{U, \eta'}}. \quad (3.47)$$

Practically, one chooses n_2 high enough such that the subsequent measurement correction has a negligible impact on the values of the measured observables and as such can be omitted altogether, except for the sporadic cases mentioned above.

Now we still have not revealed how to obtain the sign of the Pfaffian. Since we do not want to calculate the Pfaffian itself explicitly, we simply monitor the sign changes of $\text{Pf}\mathcal{M}$ as a function of the hopping parameter κ . The Hermitian fermion matrix for the gluino \tilde{Q}^2 has doubly degenerate real eigenvalues [17] and therefore

$$\det \mathcal{M} = \det \tilde{Q} = \prod_{i=1}^{\Omega/2} \tilde{\lambda}_i^2 \quad (3.48)$$

where $\tilde{\lambda}_i$ are the eigenvalues of \tilde{Q} . So from that we find

$$|\text{Pf}\mathcal{M}| = \prod_{i=1}^{\Omega/2} |\tilde{\lambda}_i| \Rightarrow \text{Pf}\mathcal{M} = \prod_{i=1}^{\Omega/2} \tilde{\lambda}_i. \quad (3.49)$$

The last implication is due to the fact that $\text{Pf}\mathcal{M}$ is a polynomial in κ which cannot have any discontinuities in its derivatives. So when any odd numbers of eigenvalues $\tilde{\lambda}_i$ change sign, so must $\text{Pf}\mathcal{M}$. Additionally, for $\kappa = 0$, we know that $\text{Pf}\mathcal{M} = \mathbb{1}$. The method is then to start from low κ (i.e. large $m_{\tilde{g}}$) and simply count the zero-crossings of eigenvalues, up to $\kappa = \kappa_{\text{simulation}}$ [30]. It is of practical importance that frequent sign changes could possibly cause the performance of the algorithm to deteriorate severely due to large cancellations and a subsequent unacceptably large increase in statistical noise. This is also known as the *sign problem*. The experience of the DESY-Münster-Roma collaboration has been though, that zero-level crossings occur extremely rarely for all practical purposes [18, 21], in particular for $\kappa < \kappa_c$.

This circumstance yields the added benefit of making the complete reweighting step in measurements unnecessary, if one has actually confirmed to be safe from zero crossings and to have a high enough order for the second polynomial. This is typically verified on a representative subset of the ensemble of configurations.

So, having all the machinery in place to produce ensembles of configurations, we now show what to do with them once they have been generated.

3.2 Measuring Observables

Since one of the goals of this study and previous work performed by the collaboration is to elucidate what the lattice has to say about the spectrum of the $N = 1$ SYM, one needs to measure expectation values on the ensemble of configurations of quantities which correspond to the various operators of the continuum theory. A prime property to check is confinement, since it is widely assumed to hold for SYM. This is realized analogously to QCD by measuring the potential between two fermions in the fundamental representation. Closely related to the potential is the Sommer scale R_0 , which characterizes the typical physical length scale of a simulation at the given input parameters. From there one can proceed to measure the masses of bound states with the relevant quantum numbers outlined in Chapter 2. Finally, we want to check the Ward-identities on the lattice which give us an independent estimate on the proximity of the simulation to the supersymmetric point.

Common to all steps of the above measurement program are some general aspects, which are collected in the following. Using the TSMB algorithm, an ensemble of field configurations is created, which will serve as the basis of any physical statements that are made about the theory on the lattice. Any given observable, after fermion integration, is a gauge invariant operator of link variables $U_\mu(x)$. Its expectation value

$$\langle \mathcal{O}([U], x) \rangle_U = \frac{1}{N} \sum_{i=1}^N \mathcal{O}([U]_i, x) \quad (3.50)$$

is an average over all configurations of the ensemble. To give the expectation value any meaning, it is necessary to assess its error which can come from a variety of sources: finite volume effects, discretization effects or statistics. It is desirable to keep the systematic errors below the statistical. This is achieved by choosing the correct setup of the simulation, such as lattice size, action, β and κ . Once the ensemble is created, one has to get a handle on the statistics. Of importance here are the related concepts of autocorrelation times of operators and Jackknife error analysis.

3.2.1 Autocorrelation Times

Let A be a primary quantity with measured values A_1, A_2, \dots, A_N . The average over the sample is, as above,

$$\bar{A} = \frac{1}{N} \sum_{i=1}^N A_i \quad (3.51)$$

where N is the sample size. If the basis of the measurement, i.e. the field configurations, are mutually independent, the regular Gaussian error suffices. However, one is often faced with a correlated measurement series, so the error needs to be adjusted accordingly. The autocorrelation time serves this purpose. The normalized autocorrelation function is defined as

$$C_{AA}(t) = \frac{\langle A_n A_{n+t} \rangle}{\langle A_n A_n \rangle} \quad (3.52)$$

where n denotes the n -th configuration in the Markov chain and t its distance in the update cycle. For large t it typically decays exponentially

$$C_{AA}(t) \rightarrow e^{-\frac{|t|}{\tau(A)}} \quad (3.53)$$

which immediately leads to the definition of the exponential autocorrelation time $\tau_{exp}(A)$:

$$\tau_{exp}(A) \equiv - \limsup_{t \rightarrow \infty} \frac{|t|}{\log |C_{AA}(t)|} . \quad (3.54)$$

This quantity naturally lends itself to the interpretation of being the decay time of the slowest mode in A . The so-called integrated autocorrelation time is defined as

$$\tau_{int}(A) \equiv \frac{1}{2} + \sum_{t=1}^{\infty} C_{AA}(t) \quad (3.55)$$

which in principle is better suited to adjust the error, since one can show that

$$\lim_{N \rightarrow \infty} \sigma^2(A) = \frac{2 \tau_{int}(A)}{N} (\bar{A}^2 - (\bar{A})^2) . \quad (3.56)$$

This relation gives us a direct prescription on how to rescale the Gaussian error ($\bar{A}^2 - (\bar{A})^2$). Conversely, one can also read off that in an ensemble of N configurations, effectively $\frac{N}{2\tau_{int}(A)}$ are independent with respect to the quantity A . In practice, due to low statistics, it is not always possible to compute $\tau_{int}(A)$ reliably. Also, there is no straightforward way of its determination for secondary quantities, such as the masses of mesons, for example. In this case, one can estimate the error independently from Jackknife analysis.

3.2.2 Jackknife Error Estimation

The idea of Jackknife analysis is to treat the process of measurement and subsequent transformation of primary quantities to secondary ones as a black box [29]. From that perspective one can get a more stable estimate of the error by simply deleting one measurement from the sample and determining its impact on the average value. Let $A_j^{(J)}$ be the average over the sample with the j -th measurement removed,

$$A_j^{(J)} = \frac{1}{N-1} \sum_{i \neq j} A_i . \quad (3.57)$$

This yields the jackknife estimators $y_j^{(J)} = y(A_j^{(J)})$ of the secondary quantity $y(A)$ with an average of

$$\bar{y}^{(J)} = \frac{1}{N} \sum_{j=1}^N y_j^{(J)} = \frac{1}{N} \sum_{j=1}^N y(A_j^{(J)}) . \quad (3.58)$$

The variance of the secondary estimators can be obtained as

$$\sigma^2(\bar{y}^{(J)}) = \frac{N-1}{N} \sum_{i=1}^N (y_i^{(J)} - \bar{y}^{(J)})^2 \quad (3.59)$$

which coincides in the case that $y(A) = A$ with the Gaussian standard deviation. So far we have achieved nothing more than getting a stable estimate of the error of secondary quantities, although still implicitly assuming uncorrelated measurements and thus underestimating the true error. The missing enhancement to this method is to aggregate n subsequent measurements into a block and treat the average of that block as one measurement, repeating the same procedure on the blocked data. The block size is then to be increased successively until the measured error approaches a plateau from below. In the limit of an infinite number of measurements, the stabilized error is the correct one for completely uncorrelated measurements. It can easily be seen that this method also serves as an implicit determination of $\tau_{int}(y(A))$. In fact, it can be extracted via

$$\tau_{int}(y(A)) = \frac{1}{2} \frac{\sigma_{n_u}^2(\bar{y})}{\sigma_1^2(\bar{y})} \quad (3.60)$$

where $\sigma_n^2(\bar{y})$ denotes the obtained error at block size n and n_u being the block size at which the blocked data appears uncorrelated.

All errors quoted in this work were obtained by Jackknife analysis.

3.3 String Tension σ and Sommer Scale R_0

The string tension between two color sources in the fundamental representation is defined as a parameter of the potential between these sources. The potential can be determined by measuring rectangular Wilson loops

$$\mathcal{W}(R, T) = \langle \text{Tr} U(\mathcal{C}_{R,T}) \rangle \quad (3.61)$$

as a product of all links $U_\mu(x)$ along the rectangular curve $\mathcal{C}_{R,T}$ with spatial and temporal separation R and T . The potential is defined as the large T behavior of these Wilson loops

$$V(R) = - \lim_{T \rightarrow \infty} \frac{\log \mathcal{W}(R, T)}{T} \quad (3.62)$$

such that

$$\mathcal{W}(R, T) \underset{T \rightarrow \infty}{\sim} C e^{-TV(R)}. \quad (3.63)$$

The coefficient

$$\sigma \equiv \lim_{R \rightarrow \infty} \frac{V(R)}{R} = - \lim_{R, T \rightarrow \infty} \frac{\log \mathcal{W}(R, T)}{RT} \quad (3.64)$$

is the so-called string tension. If the string tension is non-zero, the potential rises linearly with R :

$$V(R) \underset{R \rightarrow \infty}{\sim} \sigma R \quad (3.65)$$

which indicates a constant force σ between two color sources. This in turn is the signal for *static confinement*, which leads to the famous area law for Wilson loops [11]:

$$\lim_{R, T \rightarrow \infty} \mathcal{W}(R, T) = C e^{-\sigma R T}, \quad (3.66)$$

i.e. the loop expectation value falls off with the exponential of the enclosed area of the loop ($A = RT$). To determine the potential from the measured expectation values we proceed as follows. Defining $V(R, T)$ in accordance to the above as

$$V(R, T) \equiv \log \frac{\langle \mathcal{W}(R, T) \rangle}{\langle \mathcal{W}(R, T+1) \rangle} \quad (3.67)$$

we fit $V(R, T)$ to the ansatz

$$V(R, T) = V(R) + a e^{-bT} \quad (3.68)$$

at each spatial separation R with the three fit parameters $\{V(R), a, b\}$. The ansatz is motivated by studying the spectral decomposition of the Wilson loops and expanding the logarithm to lowest order [22]. This allows us to extract $V(R)$ at each R in the $T \rightarrow \infty$ limit. Following [31, 32], we then fit $V(R)$ to the Cornell-potential ansatz

$$V(R) = V_0 + \sigma R - e \left[\frac{1}{\mathbf{R}} \right] \quad (3.69)$$

with three fit parameters $\{V_0, \sigma, e\}$, and where $\left[\frac{1}{\mathbf{R}} \right]$ is the tree-level lattice Coulomb term

$$\left[\frac{1}{\mathbf{R}} \right] = 4\pi \int_{-\pi}^{\pi} \frac{d^3\mathbf{k}}{(2\pi)^3} \frac{\cos(\mathbf{k} \cdot \mathbf{R})}{4 \sum_{j=1}^3 \sin^2\left(\frac{k_j}{2}\right)}. \quad (3.70)$$

The Cornell-potential ansatz was originally motivated by two of the defining properties of QCD: confinement and asymptotic freedom. These aspects are encoded in the σR - and the $e \left[\frac{1}{\mathbf{R}} \right]$ -term respectively. Since it is assumed that these properties also hold in the four dimensional SYM theory, it is the ansatz we employ. The results of the fit to (3.69) allow us to read off the string tension σ . Deviations of the measured potential from that form would indicate false assumptions about confinement.

Closely related to the potential is the Sommer scale R_0 [33]. It is a useful quantity for measuring the typical physical scale in the simulation in units of the lattice spacing a . From it one can in principle determine the lattice spacing itself in physical units, if compared to real-world experimental data. The scale R –motivated by QCD– is defined through the relation

$$F(R)R^2 \Big|_{R=R(c)} = c \quad (3.71)$$

where $F(R)$ is the force between static color sources and $R(c)$ is some hadronic length scale, usually taken to be

$$R(1.65) \equiv R_0 \simeq 0.49 \text{ fm} \quad (3.72)$$

in QCD. For purposes of comparison we use the same convention here. It is important to notice, though, that the physical lattice spacing and therefore the size of the box one simulates is inaccessible in SYM theory, since no connection can be made to experiments. Nevertheless, it is useful as a quantity that can be compared to QCD simulations on a numerical basis since one expects it to be of the same order of magnitude. Following [31], one can use the fits to (3.69) as reliable estimates (up to $\mathcal{O}(a)$) for the parameters of the corresponding continuum version of the potential. Rewriting equation (3.71) we get

$$R_0^2 \frac{dV}{dR} \Big|_{R_0} = 1.65. \quad (3.73)$$

Combining this relation with equation (3.69), where we replace the lattice $\left[\frac{1}{\mathbf{R}} \right]$ with the continuum $\frac{1}{R}$, we can determine from

$$R_0 = \sqrt{\frac{1.65 - e}{\sigma}} \quad (3.74)$$

the value of the Sommer scale R_0 in units of a .

3.4 Obtaining Masses of States

The masses and amplitudes can be computed from zero-momentum two-point correlation functions at the timeslice distance Δt :

$$C(\Delta t) = \langle S^\dagger(t + \Delta t)S(t) \rangle - \langle S^\dagger(t + \Delta t) \rangle \langle S(t) \rangle \quad (3.75)$$

where $S(t)$ is the timeslice sum of an operator $\mathcal{O}_U(x)$ depending on the gauge fields $\{U(x)\}$:

$$S(t) = \frac{1}{\sqrt{V_S}} \sum_{\vec{x}} \mathcal{O}_U(\vec{x}, t), \quad (3.76)$$

while V_S is the spatial volume $(L_S)^3$. Summing over the timeslice projects out the zero momentum component of the operator. Writing out $C(\Delta t)$ in its spectral decomposition we see that

$$\begin{aligned} C(\Delta t) &= |\langle 0|S(t)|0 \rangle|^2 + \sum_n |\langle n|S(t)|0 \rangle|^2 e^{-m_n \Delta t} \pm |\langle n|S^\dagger(t)|0 \rangle|^2 e^{-m_n(T-\Delta t)} \\ &= c_0^2 + \sum_n c_n^2 (e^{-m_n \Delta t} \pm e^{-m_n(T-\Delta t)}). \end{aligned} \quad (3.77)$$

Here we already assume periodic (+) or antiperiodic (−) boundary conditions for the lattice fields. The $(T - \Delta t)$ -term accounts for the fact that the (anti-) periodic lattice implies a symmetry around $\frac{T}{2}$ where T is the maximum time-extent of the lattice. This symmetry can be exploited to reduce the noise of the correlators (time-symmetrization). For this simulation, periodic boundaries in the spatial directions are imposed in order not to break supersymmetry. In the time direction we have antiperiodic boundaries for fermions and periodic for bosonic fields.

For large values of Δt , the states with higher masses m_n for $n > 1$ in the correlator (3.77) die off exponentially, since $m_n > \dots > m_1$, and we are left with only the lightest state

$$C(\Delta t) \rightarrow c_0^2 + c_1^2 (e^{-m_1 \Delta t} \pm e^{-m_1(T-\Delta t)}) \quad (3.78)$$

surviving. This form will be the basic object we will fit to, when determining masses of states created by the various operators from the vacuum as described below. In the case that the operator has the same quantum numbers as the vacuum, it acquires a non-zero vacuum expectation value, i.e. $c_0^2 \neq 0$. This needs to be taken into account when fitting to this function.

The strategy then is to fit the time-symmetrized correlators to (3.78) in an interval $\Delta t \in [0, \dots, \frac{T}{2}]$ where the high- t end of the interval $t_f = t_{final}$ is kept fixed and to increase the starting point of the fit interval $t_i = t_{initial}$, starting from $t_i = 0$. The idea is that by increasing t_i we successively exclude more and more higher states from the measured correlator. From some point t_i onwards, the fit stabilizes to a plateau of

the fit parameters, since the only significant signal from that t_i onwards remaining in $C(\Delta t)$ will be the one from the lightest state.

It is quite possible though, that even at large Δt , the given operator displays a significant overlap with the next higher, i.e. the first excited state. In this case one needs to take that into account by not cutting off the series (3.77) after $n = 1$, but after $n = 2$ and thus fit to

$$C(\Delta t) \rightarrow c_0^2 + c_1^2(e^{-m_1 \Delta t} \pm e^{-m_1(T-\Delta t)}) + c_2^2(e^{-m_1 \Delta t} \pm e^{-m_2(T-\Delta t)}) . \quad (3.79)$$

As we will see, one is faced with various numerical challenges when fitting correlators. The most frequently encountered is the presence of a next higher state while at the same time the noise/signal ratio in the data is too bad to obtain a stable two-mass fit. For the subtleties, the interested reader is referred to the next chapter for the particular subtraction method used for extracting two masses in stable one mass fits.

A second independent method for obtaining mass estimates from correlation functions is the calculation of *effective masses* [29] which are defined at a given T and time-slice pair (t_1, t_2) . Starting from equation (3.78) and assuming $c_0^2 = 0$ and periodic boundaries, we can define c_1^2 and $m(t_1, t_2, T)$ to be the solution to the system of two equations

$$\begin{aligned} \langle S(t+t_1)S(t) \rangle &= c_1^2(e^{-m(t_1, t_2, T)t_1} + e^{-m(t_1, t_2, T)(T-t_1)}) \\ \langle S(t+t_2)S(t) \rangle &= c_1^2(e^{-m(t_1, t_2, T)t_2} + e^{-m(t_1, t_2, T)(T-t_2)}) \end{aligned} \quad (3.80)$$

where $m(t_1, t_2, T)$ is the true mass in the limit of $\{t_1, t_2, T\} \rightarrow \infty$. Defining the ratio

$$r_{12} \equiv \frac{\langle S(t+t_1)S(t) \rangle}{\langle S(t+t_2)S(t) \rangle} = \frac{e^{-m(t_1, t_2, T)t_1} + e^{-m(t_1, t_2, T)(T-t_1)}}{e^{-m(t_1, t_2, T)t_2} + e^{-m(t_1, t_2, T)(T-t_2)}} \quad (3.81)$$

and

$$\tau_i \equiv \left(\frac{T}{2} - t_i\right), \quad x \equiv e^{-m(t_1, t_2, T)} \quad (3.82)$$

one can simply solve

$$r_{12}(x^{\tau_2} + x^{-\tau_2}) = (x^{\tau_1} + x^{-\tau_1}) \quad (3.83)$$

numerically for x , where of course $m(t_1, t_2, T) = -\log x$. The advantage of this approach lies in the implied locality. It allows for a clearer determination of the vanishing influence of higher states in the correlator. It, however, comes at the cost of decreased stability, since one uses less information to extract the mass than when fitting over an entire interval. Note though, that at larger t -values and for good enough data both methods should give a mutually consistent plateau.

We used both methods concurrently as a cross-check where possible. However, final quotes on mass values are mostly obtained from the global fits of correlators since, in most cases, the effective mass estimates become noisier and less stable.

3.4.1 Fermionic Correlators

From equation (3.27) we see that in order to get correlation functions with fermionic content, we need to calculate matrix elements of the inverse fermion matrix $(Q^{-1})_{xa\alpha}^{yb\beta}$. The strategy to tackle this problem is to find solutions to the linear system

$$Qz = \omega \quad \rightarrow \quad z = Q^{-1}\omega. \quad (3.84)$$

The vector ω is referred to as the *source*, while Q^{-1} is of course the propagator. The source can have various forms, the most prominent being delta like in spin, color and space:

$$\omega_{yb\beta}^{[xa\alpha]} = \delta_{xy}\delta_{ab}\delta_{\alpha\beta} \quad (3.85)$$

where (y, b, β) labels the indices of the vector and $[xa\alpha]$ the position of the source, i.e. only this component of the vector set to 1, all others to zero. The solution vector z encodes the propagator from $[x, a, \alpha]$ to any other site, color and spin component, the so-called *sink*. The computation of z is achieved by using iterative solvers, in our case the widely used conjugate gradient algorithm (see e.g. [34] for details). It iteratively minimizes the functional

$$f(z) = \frac{1}{2}\langle z, Qz \rangle - \omega z \quad (3.86)$$

up to a desired precision yielding z as the solution vector.

Other forms of sources include so-called *wall sources*, where a complete timeslice is filled with non-zero entries in the source vector ω , such that the solution vector encodes the time slice sum of propagators from any point in this *wall* to a given end point.

3.4.2 Glueballs

Glueballs are a well known object of investigation in lattice QCD (for a detailed study see [35]). In the continuum they are objects with integer spin J and as such are classified by the irreducible representations \mathbf{D}_J of the group of space rotations $SO(3)$. Additional indices denote their transformational properties under parity \mathcal{P} and charge conjugation \mathcal{C} . As indicated in Chapter 2, we are interested in the glueballs

$$J^{\mathcal{P}\mathcal{C}} = 0^{++} \quad \text{and} \quad J^{\mathcal{P}\mathcal{C}} = 0^{-+}. \quad (3.87)$$

On the lattice, however, continuous rotational symmetry is broken down to the cubic group \mathbf{O}_h . Accordingly, here the states of the (lattice-) Hamiltonian are classified by the irreducible representations of the cubic group, of which there are five, namely

$$A_1, A_2, E, T_1, T_2 \quad \text{with respective dimensions} \quad 1, 1, 2, 3, 3. \quad (3.88)$$

Since \mathbf{O}_h is a subgroup of $SO(3)$, any representation \mathbf{D}_J induces a *subduced representation* $\mathbf{D}_J \downarrow \mathbf{O}_h$ on \mathbf{O}_h . The subduced representation no longer has to be an irreducible representation of \mathbf{O}_h , but is a direct sum of these:

$$\mathbf{D}_J \downarrow \mathbf{O}_h = \Gamma_1 \oplus \Gamma_2 \oplus \dots \quad \text{with} \quad \Gamma_i \in \{A_1, A_2, E, T_1, T_2\}. \quad (3.89)$$

Physically this means that on the lattice one would find different masses, for example, for the E -doublet and the T_1 -triplet, which make up the subduced representation $\mathbf{D}_2 \downarrow \mathbf{O}_h$. Taking the continuum limit, however, their masses should become degenerate, since there we have full rotational symmetry again and they both are the same spin-2 glueball. Of interest for our work is $\mathbf{D}_0 \downarrow \mathbf{O}_h$, since we are only concerned about spin-0 glueballs. Luckily

$$\mathbf{D}_0 \downarrow \mathbf{O}_h = A_1, \quad (3.90)$$

so we only need to look for operators with A_1 -content. Naturally, the basic operators to be taken are Wilson loops, since they are purely gluonic and as such create gluonic excitations from the vacuum. An additional requirement is that the loops should have no temporal extension in order to get a clean signal in the correlation function. The composition of the irreducible representation of the cubic group of all possible Wilson loops up to length 8 was carried out in [36]. It turns out that all loops have A_1^{++} -content while only the loops in Figure 3.1 have A_1^{-+} -content.

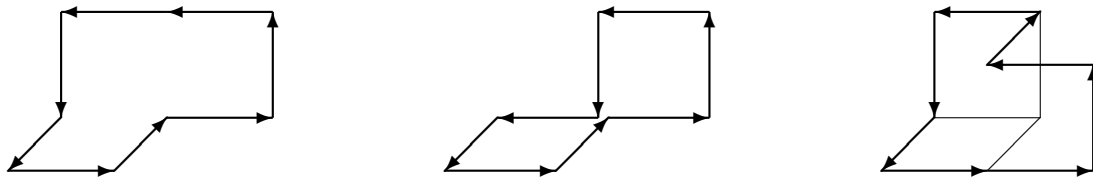


Figure 3.1: Wilson loop operators with A_1^{-+} -content. These correspond to #4, #16 and #18 in [36].

As in previous works by the collaboration, we opted for the single spatial plaquette for the 0^{++} glueball and loop #4 for the 0^{-+} glueball. These basic loops are averaged over every possible cubic rotation such that the composite operator is invariant under transformations of \mathbf{O}_h and therefore represents a spin-0 object. Moreover, in the case of the 0^{-+} , we project out the negative parity part by subtracting out the same, but with respect to x parity transformed, Wilson loop. So

$$\mathcal{O}_{0^{++}}(U, x) \equiv \text{Tr}[U_{12}(x) + U_{23}(x) + U_{31}(x)], \quad (3.91)$$

and

$$\mathcal{O}_{0^{-+}}(U, x) \equiv \sum_{\mathcal{R} \in \mathbf{O}_h} (\text{Tr}[\mathcal{W}(\mathcal{C}_{\mathcal{R}})] - \text{Tr}[\mathcal{W}(\mathcal{P}\mathcal{C}_{\mathcal{R}})]) \quad (3.92)$$

where $U_{\mu\nu}(x)$ again denotes the simple plaquette at x in the (μ, ν) -plane and $\mathcal{W}(\mathcal{C}_{\mathcal{R}})$ the Wilson loop along the line \mathcal{C} ($=$ #4 above) starting at x , rotated by the element \mathcal{R} of \mathbf{O}_h and finally parity-mirrored by \mathcal{P} with respect to the point x . It is immediately clear, that Wilson loops with A_1^{-+} -content cannot be loops, which can be rotated into their parity mirrored loop by elements of \mathbf{O}_h , since then the second sum would be identically zero. Note that here we are working with the gauge group $SU(2)$ while the analysis of [36] was carried out for $SU(3)$. Since any product of elements of $SU(2)$ has a real trace, like the above Wilson lines, the direction of traversing a loop \mathcal{C} becomes irrelevant:

$$\mathcal{W}(\mathcal{C}^{-1}) = \mathcal{W}^\dagger(\mathcal{C}) \stackrel{\mathcal{W} \in SU(2)}{=} \mathcal{W}(\mathcal{C}), \quad (3.93)$$

in contrast to $SU(3)$. Note further that if we add the parity transformed part of $\text{Tr}[U(\mathcal{R}\mathcal{C})]$ instead of subtracting it in (3.92), we get an operator with the same quantum numbers as the 0^{++} . Since this measurement requires no additional computational effort, we use it as a useful independent determination of the mass of the 0^{++} glueball.

3.4.3 Gluino-Glue Bound States

In contrast to QCD, in SYM theory it is possible to construct mixed gluonic and fermionic bound states. A spin- $\frac{1}{2}$ color singlet in particular can be built from the gluino fermion field λ and the gluonic field strength $F_{\mu\nu}$. It is part of the predicted chiral multiplet lined out in Chapter 2. In the continuum, its simplest form is [40]

$$\Sigma(x) = \sigma_{\mu\nu} \text{Tr}[\lambda(x)F_{\mu\nu}(x)]. \quad (3.94)$$

As the operator on the lattice, which projects onto the lightest state, we choose

$$\Sigma^\alpha = \sum_{i,j} \sigma_{ij}^{\alpha\beta} \text{Tr}[P_{ij}(x)\lambda^\beta(x)]. \quad (3.95)$$

Here P_{ij} is the clover plaquette operator around x with only spatial indices $\{i, j\}$ to avoid contact terms in the correlator.

$$\begin{aligned} P_{\mu\nu}(x) &= \frac{1}{8ig} \sum_{i=1}^4 (U_{\mu\nu}^{(i)}(x) - U_{\mu\nu}^{(i)\dagger}(x)) \\ U_{\mu\nu}^{(1)}(x) &= U_\nu^\dagger(x)U_\mu^\dagger(x + \hat{\nu})U_\nu(x + \hat{\mu})U_\mu(x) \\ U_{\mu\nu}^{(2)}(x) &= U_\mu^\dagger(x)U_\nu(x - \hat{\nu} + \hat{\mu})U_\mu(x - \hat{\nu})U_\nu^\dagger(x - \hat{\nu}) \\ U_{\mu\nu}^{(3)}(x) &= U_\nu(x - \hat{\nu})U_\nu(x - \hat{\nu} - \hat{\mu})U_\mu^\dagger(x - \hat{\nu} - \hat{\mu})U_\mu^\dagger(x - \hat{\mu}) \\ U_{\mu\nu}^{(4)}(x) &= U_\mu(x - \hat{\mu})U_\nu^\dagger(x - \hat{\mu})U_\mu^\dagger(x + \hat{\nu} - \hat{\mu})U_\nu(x) \end{aligned} \quad (3.97)$$

where $U_{\mu\nu}^{(1)}(x)$ is the regular plaquette defined in equation (3.3). This choice of the clover plaquette vs. the regular plaquette as the gluonic field strength operator in (3.95) is motivated by the correct behavior under parity \mathcal{P} and time reversal \mathcal{T} transformations

as opposed to just $U_{\mu\nu}(x)$. By “correct” we mean here the exact equivalence between continuum and lattice. This aspect is of importance for the study of the Ward-identities on the lattice, as we will show below.

The correlation function can thus be written as

$$\begin{aligned} C^{\alpha\beta}(\Delta t) &= -\frac{1}{4} \sum_{\vec{x}} \sum_{ij,kl} \sigma_{ij}^{\alpha\alpha'} \text{Tr}[P_{ij}(x)\sigma^a] (Q^{-1})^{yb\beta',x\alpha\alpha'} \text{Tr}[P_{kl}(y)\sigma^b] \sigma_{kl}^{\beta'\beta} \\ &= -\frac{1}{4} \sum_{\vec{x}} \sum_{ij,kl} \sigma_{ij}^{\alpha\alpha'} \chi_{ij}^a(x) \underbrace{(Q^{-1})^{yb\beta',x\alpha\alpha'} \chi_{kl}^b(y)}_I \sigma_{kl}^{\beta'\beta} \end{aligned} \quad (3.98)$$

where, in the second line, we defined $\chi_{ij}^a(x) = \text{Tr}[P_{ij}(x)\sigma^a]$ and naturally $\Delta t = (x_0 - y_0)$. In practice, a source of $\chi(y)$ is constructed on a randomly chosen timeslice covering it completely (*wall source*) on which the fermion matrix Q is inverted. From this, expression I in equation (3.98) is obtained. The complete correlator is then constructed by multiplying and contracting I , $\chi(x)$ and the σ matrices accordingly.

It can be shown [19] that the gluino glue correlator has the simple Lorentz structure

$$C^{\alpha\beta}(\Delta t) = C_1(\Delta t)\delta^{\alpha\beta} + C_2(\Delta t)\gamma_0^{\alpha\beta} \quad (3.99)$$

with $C_i(\Delta t) \in \mathbb{R}$. From time reversal symmetry one also sees that these components have different periodicity

$$\begin{aligned} C_1(\Delta t) &= -C_1(T - \Delta t) \\ C_2(\Delta t) &= C_2(T - \Delta t) \end{aligned} \quad (3.100)$$

giving us the benefit of having two independent ways to measure the mass of the lightest state in this channel.

3.4.4 Adjoint Mesons

To measure the complete predicted multiplet we also have to include operators consisting exclusively of gluinos, which in the sequel will be called a -mesons to remind us of the fact that the gluinos transform according to the adjoint representation of the gauge group. In analogy to QCD,

$$\mathcal{O}_{a-f_0}(x) \equiv \lambda(x)\lambda(x) \quad \mathcal{O}_{a-\eta'}(x) \equiv \lambda(x)\gamma_5\lambda(x) , \quad (3.101)$$

where the f_0 and η' would be the equivalent flavor singlet mesons consisting of quarks in the fundamental representation of $SU(3)$. We will also refer to the $a-f_0$ as the scalar and to the $a-\eta'$ as the pseudo-scalar meson. As in QCD, the two-point functions of the a -mesons have a disconnected and a connected piece

$$C(\Delta t) = \sum_{\vec{x}} \langle \text{Tr}[\Gamma Q_{x,x}^{-1}] \text{Tr}[\Gamma Q_{y,y}^{-1}] \rangle - 2 \langle \text{Tr}[\Gamma Q_{x,y}^{-1}] \text{Tr}[\Gamma Q_{y,x}^{-1}] \rangle \quad (3.102)$$

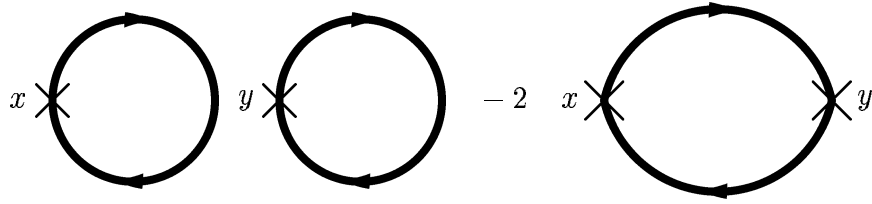


Figure 3.2: The gluino line graphs for the two-point function of the color singlet a -meson operators.

with the difference of a factor of 2, however, which comes from the Majorana property of the gluino. Here the trace is meant to cover color and spin.

The numerical evaluation of the correlator is computationally the most demanding part. The connected piece is obtained by the regular method of choosing a delta-like source on a random site y in spin and color and calculating the propagator $Q_{y,x}^{-1}$ to every point x , color a and spin α . The sink is summed over to project out the zero momentum part.

The disconnected propagator is known as an all-to-all propagator. In theory one would have to compute the full propagator from every lattice point y , spin and color back to itself, which would mean doing $N_{Vol} \times N_{spin} \times N_{color}$ inversions of the fermion matrix on each configuration. Since this is computationally not feasible, one has to resort to one of the various approximations to the problem that are available. In the past, the diagram was calculated by means of the *volume source technique* (VST) by the collaboration, but due to its associated problems which will be explained below, we used stochastic estimators in this work.

3.5 Matrix Inversion Methods

This section explores in detail how to obtain the all-to-all propagators for the a -mesons. We present two techniques, the VST and the use of stochastic estimators. Currently, a third method is also in use by the lattice community, the *truncated eigenmode expansion* [37], which we will not touch on here.

Up to now, we mostly suppressed color and spin indices when referring to the fermion matrix Q . At times, it is necessary to write them out explicitly, as we will see in the

following. Restating equation (3.102), we have the object of investigation

$$C_{\tilde{g}\tilde{g}}(\Delta t) = \frac{1}{V_S} \sum_{\vec{x}} \langle \text{Tr}_{sc}[\Gamma Q_{x,x}^{-1}] \text{Tr}_{sc}[\Gamma Q_{y,y}^{-1}] - 2 \text{Tr}_{sc}[\Gamma Q_{x,y}^{-1} \Gamma Q_{y,x}^{-1}] \rangle \quad (3.103)$$

$$\equiv C_{\tilde{g}\tilde{g}}(\Delta t)_{\text{disc.}} + C_{\tilde{g}\tilde{g}}(\Delta t)_{\text{conn.}} \quad (3.104)$$

where from now on, we focus on the evaluation of the disconnected part. Its time slice sum is

$$S_{\alpha,\beta}(t)_{\text{disc.}} = \sum_{\vec{x}} \text{Tr}_c[Q_{x\alpha,x\beta}^{-1}] \quad (3.105)$$

where Tr_c is the trace over color and $x = (t, \vec{x})$ with spin indices explicit. This is used to construct the correlator

$$C_{\tilde{g}\tilde{g}}(\Delta t)_{\text{disc.}} = \frac{1}{TV_S} \sum_t \sum_{\alpha,\beta} \langle [\Gamma S(t)]_{\alpha,\alpha} [\Gamma S(t + \Delta t)]_{\beta,\beta} \rangle \quad (3.106)$$

where $\Gamma \in \{\mathbb{1}, \gamma_5\}$.

3.5.1 Volume Source Technique

Employing the ‘‘volume source technique’’ [39] we can estimate the disconnected part. For the connected part, we usually perform the inversion of Q with the source $\omega_{yb\beta}^{[x,a,\alpha]}$. In contrast, the VST puts a (real) 1 at every site for every spin and color¹:

$$QZ = \omega_V^{[a,\alpha]} = \sum_x \omega^{[x,a,\alpha]} \quad (3.107)$$

The solution we then get is

$$Z^{[a,\alpha]} = Q^{-1} \omega_V^{[a,\alpha]}, \quad (3.108)$$

more explicitly,

$$QZ = Q_{xa\alpha,yb\beta} Z_{yb\beta} = \sum_z \omega_{xa\alpha}^{[z,c,\delta]} \quad (3.109)$$

$$\Rightarrow \underbrace{Q_{rd\gamma,xa\alpha}^{-1} Q_{xa\alpha,yb\beta}}_{\delta_{rd\gamma,yb\beta}} Z_{yb\beta} = Q_{rd\gamma,xa\alpha}^{-1} \sum_z \omega_{xa\alpha}^{[z,c,\delta]} \quad (3.110)$$

$$\begin{aligned} Z_{rd\gamma} &= Q_{rd\gamma,xa\alpha}^{-1} \sum_x \delta_{xa\alpha,zc\delta} \\ &= \sum_z Q_{rd\gamma,zc\delta}^{-1} \\ &= Q_{rd\gamma,rc\delta}^{-1} + \sum_{z \neq r} Q_{rd\gamma,zc\delta}^{-1} \end{aligned} \quad (3.111)$$

¹This means we have to do $N_{\text{spin}} \times N_{\text{color}}$ inversions per configuration.

with the first piece obviously being the one we are interested in and the second piece being the “error” of the approximation by this method. In their original work, the inventors of the VST claim that the second term is zero when averaged over the ensemble, essentially relying on Elitzur’s theorem [38] stating that any non gauge invariant quantity averages away when measured over the complete ensemble. The basis of this claim is to be checked in the following.

The structure of the time slice sum (after renaming dummy indices) is as follows:

$$S_V(t)_{\alpha,\beta} = \sum_{\vec{x}} \text{Tr}_c \left(Q_{x\alpha,x\beta}^{-1} + \sum_{y \neq x} Q_{x\alpha,y\beta}^{-1} \right) \quad (3.112)$$

$$\equiv S_{gi}(t)_{\alpha,\beta} + S_{ngi}(t)_{\alpha,\beta} \quad (3.113)$$

where gi and ngi denote the gauge-invariant and the supposedly non-gauge-invariant part respectively. The correlator then has the structure (suppressing spin indices)

$$\begin{aligned} & C^{(VST)}(\Delta t) \\ &= \frac{1}{TV_S} \sum_t \text{Tr}_s \left[\Gamma S(t) \right] \text{Tr}_s \left[\Gamma S(t + \Delta t) \right] \\ &= \frac{1}{TV_S} \sum_t \text{Tr}_s \left[\Gamma \text{Tr}_c \sum_{\vec{x}} \left(Q_{x,x}^{-1} + \sum_{y \neq x} Q_{x,y}^{-1} \right) \right] \text{Tr}_s \left[\Gamma \text{Tr}_c \sum_{\vec{x}'} \left(Q_{x',x'}^{-1} + \sum_{y' \neq x'} Q_{x',y'}^{-1} \right) \right] \end{aligned} \quad (3.114)$$

where $t' = t + \Delta t$.

To begin with, we first look at the gauge average of the generic quantity

$$\langle \text{Tr}_c Q_{x,y}^{-1} [V^g] \rangle_g \quad (3.115)$$

where $\langle \dots \rangle_g$ denotes the average over different gauges, which is the same as performing the integral over the group manifold using the Haar measure where V^g is the gauge transformed SU(2) matrix in the adjoint representation defined in (3.8):

$$\begin{aligned} \langle \text{Tr}_c Q_{x,y}^{-1} [V^g] \rangle_g &= \langle g_{x,aa'}^{-1} Q_{xa',yb'}^{-1} [V] g_{y,b'a} \rangle_g \\ &= \langle g_{x,aa'}^{-1} g_{y,b'a} \rangle_g Q_{xa',yb'}^{-1} \end{aligned} \quad (3.116)$$

$$1) \quad x \neq y : \quad \langle g_{x,aa'}^{-1} \rangle \langle g_{y,b'a}^{-1} \rangle = 0 \quad (3.117)$$

$$2) \quad x = y : \quad \frac{1}{3} \delta_{a'b'} \delta_{aa} = \delta_{a'b'} \quad (3.118)$$

$$\stackrel{2)}{=} \delta_{xy} \delta_{a'b'} Q_{xa',yb'}^{-1} [V] \quad (3.119)$$

The results (3.117) and (3.118) were taken from [22] (equation (4.68) for SO(3)). With this result we want to look for non-zero contributions of the correlator with terms coming from $S_{ngi}(t)_{\alpha,\beta}$.

The Cross Term

The cross term is of type

$$Q_{x\alpha,x\beta}^{-1}[V^g] \sum_{y' \neq x'} Q_{x'\beta',y'\alpha'}^{-1}[V^g] \quad (3.120)$$

resulting in the color structure

$$\langle g_{x,aa'}^{-1} g_{x,b'a} g_{y',cc'}^{-1} g_{x',d'c} \rangle_g \quad (3.121)$$

Note the color trace apparent in the indices a and c . We would get non zero contributions from this expression if

1. $x' = y'$: this is by definition excluded
2. $x = x', x = y' \Rightarrow x' = y'$: see 1.

So here we do not get any contributions in the gauge average, i.e. the object has no gauge invariant piece.

The Sum Term

The term involving the two sums looks like

$$\sum_{\substack{y \neq x \\ y' \neq x'}} \text{Tr}_c \left[Q_{x\alpha,y\beta}^{-1}[V^g] \right] \text{Tr}_c \left[Q_{x'\alpha',y'\beta'}^{-1}[V^g] \right], \quad (3.122)$$

yielding the color structure

$$\langle g_{x,aa'}^{-1} g_{y,b'a} g_{x',cc'}^{-1} g_{y',d'c} \rangle_g \quad \text{where} \quad y \neq x, y' \neq x'. \quad (3.123)$$

As above we get (non-zero) contributions if

1. $y = y', x = x'$: can be excluded by requiring $\Delta t = (x_0 - x'_0) \neq 0$ in the correlator.
2. $y = x', y' = x$, this gives (from above):

$$\begin{aligned} \langle g_{x,aa'}^{-1} g_{y,b'a} g_{x',cc'}^{-1} g_{y',d'c} \rangle_g &= \langle g_{x,aa'}^{-1} g_{x',b'a} g_{x',cc'}^{-1} g_{x,d'c} \rangle_g \\ \text{here} &= \langle g_{x,aa'}^{-1} g_{x,d'c} \rangle_g \langle g_{x',b'a} g_{x',cc'}^{-1} \rangle_g \\ &= \langle g_{x,a'a} g_{x,d'c} \rangle_g \langle g_{x',b'a} g_{x',c'c} \rangle_g \\ [22] &= \frac{1}{3^2} \delta_{a'd'} \delta_{ac} \delta_{b'c'} \delta_{ac} \\ &= \frac{1}{3} \delta_{a'd'} \delta_{b'c'}. \end{aligned} \quad (3.124)$$

So plugging this result into (3.122), we get

$$\frac{1}{3} \delta_{a'd'} \delta_{b'c'} Q_{xa',x'b'}^{-1} Q_{x'c',xd'}^{-1} = \frac{1}{3} Q_{xa',x'b'}^{-1} Q_{x'b',xa'}^{-1}. \quad (3.125)$$

In the end, we have for the disconnected piece

$$\begin{aligned} C_{\tilde{g}\tilde{g}}(\Delta t)_{\text{disc.}} &= \left[\Gamma S(t) \Gamma S(t + \Delta t) \right] \\ &= \frac{1}{TV_S} \sum_t \sum_{\vec{x}, \vec{x}'} \left[\text{Tr}_{sc}[\Gamma Q_{x,x}^{-1}] \text{Tr}_{sc}[\Gamma Q_{x',x'}^{-1}] + \frac{1}{3} \text{Tr}_s[\Gamma Q_{x'a',xb'}^{-1}] \text{Tr}_s[\Gamma Q_{xb',x'a'}^{-1}] \right], \end{aligned} \quad (3.126)$$

where again $t' = t + \Delta t$. The second term is clearly a term we have not bargained for. It represents an unwanted gauge invariant contribution that has so far been ignored in applications of the VST. Note that the unwanted term looks suspiciously like the connected piece $C_{\tilde{g}\tilde{g}}(\Delta t)_{\text{conn.}}$, but putting back the spinor indices from (3.103), we see that these do not match up with the connected piece:

$$\text{Tr}_{sc} \left[\Gamma Q_{x,x'}^{-1} \Gamma Q_{x',x}^{-1} \right] \quad \text{vs.} \quad \text{Tr}_c \left[\text{Tr}_s[\Gamma Q_{x,x'}^{-1}] \text{Tr}_s[\Gamma Q_{x',x}^{-1}] \right]. \quad (3.127)$$

Size of the Error

In our case, the zero momentum two point correlator (3.77) works out to be (without the spurious piece)

$$\frac{1}{V_S} \langle \text{Tr}_{sc}[\Gamma S(x_0)] \text{Tr}_{sc}[\Gamma S(x'_0)] \rangle - V_S \left\langle \frac{1}{TV_S} \sum_t \text{Tr}_{sc}[\Gamma S(t)] \right\rangle^2 - \frac{2}{V_S} \sum_{\vec{x}\vec{x}'} \langle \text{Tr}_{sc}[\Gamma Q_{x,x'}^{-1} \Gamma Q_{x',x}^{-1}] \rangle. \quad (3.128)$$

Where the left most term is the disconnected part, the middle piece is the vacuum expectation value of the operator (this is only relevant in the scalar case, since for $\Gamma = \gamma_5$, its vacuum expectation value is zero due to the invariance of the vacuum under parity) and the right most term is the connected part. So we can write relation (3.127) with the exact normalization factors

$$-\frac{2}{V_S} \sum_{\vec{x}\vec{x}'} \text{Tr}_{sc} \left[\Gamma Q_{x,x'}^{-1} \Gamma Q_{x',x}^{-1} \right] \quad \text{vs.} \quad \frac{1}{3V_S} \sum_{\vec{x}\vec{x}'} \text{Tr}_c \left[\text{Tr}_s[\Gamma Q_{x,x'}^{-1}] \text{Tr}_s[\Gamma Q_{x',x}^{-1}] \right]. \quad (3.129)$$

It is hard to theoretically judge the exact size of the error, since the spin structure is not familiar. One can speculate though, that it should be of the same order of magnitude as the connected correlator. We can, however, measure it numerically. On small lattices, for example $L^3 \times T = 6^3 \times 8$, one can calculate the exact all-to-all propagator. On larger lattices one can perform several (volume source) inversions, separated by a random gauge transformation and then compare the correlators configuration-wise by averaging

1. the time-slice sums over gauge transformations, which would let the extra piece in (3.111) disappear from the beginning, up to small, controllable errors. This method we call the *correct*.
2. the correlation functions, which would most closely mimic the classic application of the VST of calculating one inversion per configuration for every configuration in the ensemble and then calculating the average correlator. This is bound to produce the wrong correlator (3.126).

We defer the numerical assessment to the next chapter and note for the protocol here that the original claim [39] of the VST converging to the wanted two-loop correlator in the limit of an infinitely large ensemble is indeed incorrect.

3.5.2 Stochastic Estimators

Since we saw that the VST possibly yields wrong results, it is important to have an independent alternative at hand. The stochastic estimation technique (SET) provides this alternative, as the error of the approximation is purely statistical and as such can be separated from the systematic errors inherent in the VST.

The idea is straightforward: let $\{\eta^a\}$ be an ensemble of complex normalized source vectors with $a \in \{1, \dots, N_{est}\}$. Their random entries are chosen such that in the limit of $N_{est} \rightarrow \infty$,

$$\langle \eta_i^a \rangle \equiv \frac{1}{N_{est}} \sum_{a=1}^{N_{est}} \eta_i^a = 0 \quad (3.130)$$

and

$$\langle \eta_i^\dagger \eta_j \rangle = \delta_{ij}, \quad (3.131)$$

where $\{i, j\}$ label the vector indices of η . In our context this can mean either the site x , color, or spin or their combination. These conditions are fulfilled if the entries of the noise vectors carry, for example, Gaussian or complex \mathbb{Z}_2 noise. In the latter case the entries consist of a randomly chosen $\frac{1}{\sqrt{2}}(\pm 1 \pm i)$. Performing the fermion matrix inversion on each of these sources, we get from the solution of

$$\sum_i Q_{ji} Z_i = \eta_j \quad \Rightarrow \quad Z_i = \sum_j Q_{ij}^{-1} \eta_j \quad (3.132)$$

that

$$\begin{aligned} \langle \eta_j^\dagger Z_i \rangle_{N_{est}} &= \left\langle \sum_k Q_{ik}^{-1} \eta_j^\dagger \eta_k \right\rangle_{N_{est}} \\ &= \sum_k Q_{ik}^{-1} \langle \eta_j^\dagger \eta_k \rangle_{N_{est}} \end{aligned} \quad (3.133)$$

$$= Q_{ji}^{-1} \langle \eta_j^\dagger \eta_j \rangle_{N_{est}} + \sum_{k \neq j} Q_{ik}^{-1} \langle \eta_j^\dagger \eta_k \rangle_{N_{est}} \quad (3.134)$$

$$\stackrel{N_{est} \rightarrow \infty}{=} Q_{ji}^{-1} . \quad (3.135)$$

To calculate the diagonal elements Q_{xx}^{-1} that are needed for the disconnected propagator, we therefore simply have to average the scalar product of the solution vector to the source and the source itself:

$$\langle \eta_i^\dagger Z_i \rangle_{N_{est}} \rightarrow Q_{ii}^{-1} \quad (3.136)$$

for a sufficient number of random sources.

The main advantage of the stochastic method is that, in contrast to the VST, the accuracy of the determination of Q_{ii}^{-1} or, conversely, its errors are entirely separated from the errors coming from the simulation. In principle one could perform $N_{est} = \infty$ estimations to get an exact all-to-all propagator on each configuration. For any finite N_{est} , the error is purely statistical. With the VST, the ordinary² error only averages away over the trajectory in simulation space, therefore an exact determination is only possible for $N_{configs} \rightarrow \infty$.

However, the stochastic method can lead to a big variance

$$\frac{\sigma}{\sqrt{N_{est}}} = \frac{1}{N_{est}} \sqrt{\sum_i (x_i - \bar{x})^2} \quad (3.137)$$

on the observables $\text{Tr}_{s,c,x}[\Gamma Q^{-1}]$. The goal is to suppress this variance while still maintaining statistical correctness. As one standard enhancement we use the so-called *spin-explicit method* (SEM): the statistical error of $\text{Tr}[\Gamma Q_{ii}^{-1}]$ receives contributions from off-diagonal elements (the second term in equation (3.134)), which are only suppressed in the $N_{est} \rightarrow \infty$ limit

$$\sigma(Q_{ii}^{-1}) \sim \sum_{j \neq i} Q_{ji}^{-1} \langle \eta_j^\dagger \eta_i \rangle . \quad (3.138)$$

For Wilson fermion matrices we have

$$\text{Tr}[Q_{ii}^{-1}] \gg \text{Tr}[Q_{ij}^{-1}] \quad \text{with } i \neq j, \quad (3.139)$$

where $i, j = (x, \text{spin})$ here. So the evaluation of off-diagonal elements of Q_{ij}^{-1} with $i \neq j$, such as $\text{Tr}[\gamma_5 Q^{-1}]$, is also influenced by the greater diagonal elements

$$\sigma(Q_{ij}^{-1}) \sim Q_{ii}^{-1} \langle \eta_i^\dagger \eta_i \rangle . \quad (3.140)$$

²as opposed to the ‘‘extra’’ error we determined above, that does not average away,

Therefore their relative statistical error is greater than that of $\text{Tr}[Q_{ii}^{-1}]$. Using the SEM, one performs stochastic inversion in the spin subspaces. This is achieved by \mathbb{Z}_2 noise on only one spin-component. For regular Dirac fermions, it introduces a factor of four more fermion matrix inversions; for the Majorana case considered here, the number of inversions doubles, see Appendix A.2. On the other hand it reduces the error terms contributing in (3.140) by a half (by four for Dirac fermions). This reduces the error of $\text{Tr}[\gamma_5 Q_{ii}^{-1}]$ approximately by a factor of $\frac{1}{\sqrt{2}}$, as we will see in the following chapter, where the numerical results are collected. One has to note, though, that for the same reasons the error of $\text{Tr}[Q_{ii}^{-1}]$ increases, albeit by less than $\sqrt{2}$. We consider this to be an acceptable trade-off.

3.6 Ward Identities

We finally turn to the derivation of the lattice formulation of the SUSY Ward identities. We will keep this section brief and blatantly brush over various subtleties since we do not want to rehearse the exercise but to provide the reader with the relevant tools and concepts needed to understand the numerical work in the following chapter. For a thorough discussion of these issues, please see [19] and [21] where the original work was developed. Here we will mostly follow [21] and the continuum equivalent in Chapter 2, cutting a few corners in the process.

Supersymmetry is explicitly broken on the lattice by a non-zero gluino mass $m_{\tilde{g}}$, the Wilson action and by the lattice discretization $a \neq 0$ itself. However, when taking the $a \rightarrow 0$ continuum limit, it should be restored. One can nevertheless derive the lattice SUSY Ward identity corresponding to (2.40) if one takes the symmetry-breaking terms into account. If the corresponding Ward identity is then satisfied in the simulation, albeit up to $\mathcal{O}(a)$ -effects, it gives a good indication for the restoration of supersymmetry in the continuum limit at the chosen simulation parameters.

A lattice transcription of the SUSY continuum transformations (2.22) and (2.23) is not unique. Their only requirement is that they have to reproduce the continuum transformations in the $a \rightarrow 0$ limit. Therefore one can aim to minimize the SUSY breaking at $\mathcal{O}(a)$ by choosing appropriate irrelevant operators. Requiring the lattice operators to transform as their continuum counterparts with respect to time reversal

and parity, one finds that a particular choice is

$$\begin{aligned}
\delta U_\mu(x) &= -\frac{iga}{2}(\bar{\epsilon}(x)\gamma_\mu U_\mu(x)\lambda(x) + \bar{\epsilon}(x + \hat{\mu})\gamma_\mu\lambda(x + \hat{\mu})U_\mu(x)) \\
\delta U_\mu^\dagger(x) &= \frac{iga}{2}(\bar{\epsilon}(x)\gamma_\mu\lambda(x)U_\mu^\dagger(x) + \bar{\epsilon}(x + \hat{\mu})\gamma_\mu U_\mu^\dagger(x)\lambda(x + \hat{\mu})) \\
\delta\lambda(x) &= \frac{1}{2}P_{\mu\nu}(x)\sigma_{\mu\nu}\epsilon(x) \\
\delta\bar{\lambda}(x) &= -\frac{1}{2}\bar{\epsilon}(x)\sigma_{\mu\nu}P_{\mu\nu}(x) ,
\end{aligned} \tag{3.141}$$

where $P_{\mu\nu}$ is the clover plaquette as defined in equation (3.97) and $\epsilon(x)$ an infinitesimal local Majorana parameter. Using the same strategy as in the continuum, these transformations lead us to the bare lattice Ward identity

$$\langle (\nabla_\mu S_\mu(x)) Q(y) \rangle = m_0 \langle \chi(x) Q(y) \rangle + \langle X_S(x) Q(y) \rangle - \left\langle \frac{\delta Q(y)}{\delta \bar{\epsilon}(x)} \right\rangle , \tag{3.142}$$

where we used the symmetric lattice derivative

$$\nabla_\mu = \frac{f(x + \hat{\mu}) - f(x - \hat{\mu})}{2a} \tag{3.143}$$

and with $\chi(x)$ the same as in equation (3.95)

$$\chi^\alpha(x) = \sum_{\mu\nu} \sigma_{\mu\nu}^{\alpha\beta} \text{Tr}[P_{\mu\nu}(x)\lambda^\beta(x)]. \tag{3.144}$$

This leads to the definition of the supercurrent

$$S_\mu(x) = -\sum_{\rho\sigma} \sigma_{\sigma\rho}\gamma_\mu \text{Tr}[P_{\sigma\rho}(x)\lambda(x)]. \tag{3.145}$$

The last term in equation (3.142) is a contact term, which vanishes on-shell ($x \neq y$) and is therefore ignored in the following. All SUSY breaking terms in (3.142) were collected in the operator $X_S(x)$. The explicit form is rather complicated [41, 42]. Important here is only its behavior towards the continuum limit, namely that of an operator of dimension $d = \frac{11}{2}$

$$\mathcal{O}(x) \equiv \lim_{a \rightarrow 0} X_S(x) . \tag{3.146}$$

A different possibility is to use the lattice backwards derivative $\nabla_\mu^b = \frac{f(x) - f(x - \hat{\mu})}{a}$ instead of the symmetric, appropriate for a point-split definitions for operators. The Ward identity remains formally unchanged by such a redefinition. See [19, 21] for details. Here we only work with point-like currents.

In order to study the renormalized Ward identity, one needs to investigate the mixing pattern of the operator X_S . The analysis is similar to that of the axial Ward identity on the lattice for QCD [43, 44]. Operator mixing occurs with operators of dimensions $d \leq \frac{11}{2}$ with the same quantum numbers (i.e. the same transformation properties

under equations (3.141) as $\mathcal{O}(x)$. The on-shell mixing pattern involving operators with $\frac{7}{2} \leq d \leq \frac{11}{2}$ is given by

$$\begin{aligned} \mathcal{O}_{11/2}^R(x) &= Z_{11/2}[\mathcal{O}_{11/2}(x) + a^{-1}(Z_S - 1)\nabla_\mu S_\mu(x) + a^{-1}Z_T\nabla_\mu T_\mu(x) + a^{-2}Z_\chi\chi(x)] \\ &\quad + \sum_j Z_{11/2}^{(j)}\mathcal{O}_{11/2}^{(j)R}(x). \end{aligned} \quad (3.147)$$

The mixing current $T_\mu(x)$ is

$$T_\mu(x) = 2 \sum_\nu \gamma_\nu \text{Tr}[P_{\mu\nu}(x)\lambda(x)]. \quad (3.148)$$

So now, one can substitute $\mathcal{O}_{11/2}(x)$ by means of (3.147) into the bare Ward identity of equation (3.142), yielding

$$Z_S\langle(\nabla_\mu S_\mu(x))Q(y)\rangle + Z_T\langle(\nabla_\mu T_\mu(x))Q(y)\rangle = m_S\langle\chi(x)Q(y)\rangle + \mathcal{O}(a), \quad (3.149)$$

with the subtracted gluino mass

$$m_S = m_0 - a^{-1}Z_\chi, \quad (3.150)$$

and the supposedly renormalized SUSY current can then be written as

$$\hat{S}_\mu(x) = Z_S S_\mu(x) + Z_T T_\mu(x). \quad (3.151)$$

In principle the identity is satisfied for any insertion operator Q . To investigate this in a numerical study, we need to choose a specific one to test. Since trivial cases are uninteresting, a gauge invariant $Q(y)$ with the same quantum numbers as $\chi, S_\mu, \nabla_\mu T_\mu$ is needed. Otherwise the expectation values $\langle \dots \rangle = 0$ would fulfill the WI trivially. So $Q(y)$ needs to have spin- $\frac{1}{2}$. Examples of the lowest possible $d = \frac{7}{2}$ operators are S_0, T_0, χ and also

$$\chi^{(sp)}(y) = \sum_{i<j} \sigma_{ij} \text{Tr}[P_{ij}(y)\lambda(y)] \quad (3.152)$$

with i, j spatial. However, at $d = \frac{7}{2}$, there can only exist two independent spin- $\frac{1}{2}$ operators. Indeed one finds that

$$\chi(y) = \gamma_0 T_0(y) - 2\chi^{(sp)}(y) \quad (3.153)$$

$$S_0(y) = 2\gamma_0(\gamma_0 T_0(y) - 2\chi^{(sp)}(y)). \quad (3.154)$$

For our work we take $\chi^{(sp)}$ as the insertion operator. The other possible independent insertion operator T_0 turns out to be very noisy [21].

We now turn to the strategy of numerical evaluation. Considering the zero momentum Ward identity

$$\sum_{\vec{x}} \langle \nabla_0 S_0(x) Q(y) \rangle + \frac{Z_T}{Z_S} \sum_{\vec{x}} \langle \nabla_0 T_0(x) Q(y) \rangle = \frac{m_S}{Z_S} \sum_{\vec{x}} \langle \chi(x) Q(y) \rangle + \mathcal{O}(a), \quad (3.155)$$

we focus on the correlator containing the SUSY current (the following analysis holding for the other correlators analogously). We see its structure, with spin indices explicitly written out, is

$$C_{\alpha\beta}^{S,Q}(\Delta t) = a^{d_Q+9/2} \sum_{\vec{x}} \langle (\nabla_0 S_0)_\alpha(x) \bar{Q}_\beta(y) \rangle \quad (3.156)$$

Consider its expansion in the basis of Dirac matrices Γ ,

$$C_{\alpha\beta}^{S,Q}(\Delta t) = \sum_{\Gamma} C_{\Gamma}^{S,Q}(\Delta t) \Gamma_{\alpha\beta} \quad (3.157)$$

where

$$C_{\Gamma}^{S,Q}(\Delta t) \equiv \text{Tr}_{sc}[\Gamma C^{S,Q}(\Delta t)] \in \mathbb{R} . \quad (3.158)$$

Using the discrete lattice symmetries, one finds that only two of these coefficients are non-zero:

$$C_{\mathbb{1}}^{S,Q}(\Delta t) \equiv \sum_{\vec{x}} \langle (\overline{\nabla_0 S_0}(x)) Q(y) \rangle \quad (3.159)$$

$$C_{\gamma_0}^{S,Q}(\Delta t) \equiv \sum_{\vec{x}} \langle (\overline{\nabla_0 S_0}(x)) \gamma_0 Q(y) \rangle . \quad (3.160)$$

So with these two equations we can solve a system of equations for the ratios of the renormalization factors:

$$\begin{aligned} C_{\mathbb{1}}^{S,Q}(\Delta t) + \frac{Z_T}{Z_S} C_{\mathbb{1}}^{T,Q}(\Delta t) &= \frac{am_s}{Z_S} C_{\mathbb{1}}^{X,Q}(\Delta t) \\ C_{\gamma_0}^{S,Q}(\Delta t) + \frac{Z_T}{Z_S} C_{\gamma_0}^{T,Q}(\Delta t) &= \frac{am_s}{Z_S} C_{\gamma_0}^{X,Q}(\Delta t) , \end{aligned} \quad (3.161)$$

with the insertion operator that was chosen above. This is the agenda for the numerical check of the fulfilled Ward identities. In particular, their study allows us to determine the quantity $am_s Z^{-1}$ for the gluino mass and the soft breaking of SUSY on the lattice.

3.7 The Massless Gluino Limit

The only theoretically founded method to assess the massless gluino limit is the investigation of the Ward identity (3.155). The massless gluino limit corresponds to $m_S \rightarrow 0$. By determining $am_s Z_s^{-1}$ at different κ 's and under the assumption that it behaves linearly in $1/\kappa$,

$$am_s \rightarrow a \left(\frac{1}{\kappa} - \frac{1}{\kappa_c} \right) , \quad (3.162)$$

one can make an extrapolation to $m_S = 0$ and read off κ_c .

A second method, though not completely rigorous, is based on the OZI approximation. It has been suggested in [9] that in this approximation, where only the connected

piece of the correlator is retained, the $a-\eta'$ should behave like the pion in QCD. This means that in this approximation the $a-\pi$, as we shall call it, should become massless at some critical value of the bare gluino mass m_c or κ_c respectively. In this limit, the disconnected part of $C_{a-\eta'}(\Delta t)$ should give the particle its non-zero mass and the mass degeneracy between members of the multiplet should be restored in the continuum limit, since chiral symmetry and supersymmetry are restored simultaneously at m_c [14]. It is important to realize that “the $a-\pi$ ” is not a physical state of the theory, since we only have one flavor of gluino and cannot construct flavor non-singlets like the pions of QCD. Because of this, only a “pseudo”-chiral limit can be defined. In short, one expects within the OZI approximation the mass of the $a-\pi$ -mode to behave according to the PCAC relation. Using the methods of Section 3.4 one can determine the mass of this mode at different κ 's and extrapolate it to the $m_{a-\pi}^2 = 0$ case, giving an estimate for κ_c .

Comparison of the first estimate with the latter should give a good indication of the internal consistency of the lattice formulation of the theory.

Chapter 4

Analysis and Results

In the following we present the numerical results of our study. Its agenda for the investigation was outlined in the previous chapter. Starting by the characterization of the individual ensembles we used by simulation parameters and quantities such as the potential and the Sommer scale, we move onto results from tests of the stochastic estimation method and converge on the results of the mass spectrum. The numerical results for the Ward identities will be discussed and, finally, we will give some comments on the finite volume effects we believe are present.

Our objective is to give a coherent picture of the numerical results concerning the $N = 1$ SYM model on the lattice. This entails at some points using results not determined here, but in previous studies. These numbers will be flagged appropriately.

4.1 Simulation Details

A summary of the ensembles we used for this investigation is displayed in Table 4.1. Of these, the 12c-ensembles of lattice size $12^3 \times 24$ were previously produced and partially analyzed [19, 20], while the larger 1940.16c of size $16^3 \times 32$ was newly generated and the 1955.16c is a current production run. From the table one observes a gradual progression to lighter gluino masses, i.e. larger κ , and larger lattices, while maintaining a constant bare coupling β . The reason for this is twofold. Obviously, the goal is to approach the massless gluino limit as close as numerically possible. As the gluino becomes lighter we simulate in the region, where the symmetry breaking effects occur linearly in $m_{\tilde{g}}$. A big problem is that a lighter gluino mass causes the algorithm to exhibit critical slowing down, i.e. the computational effort to generate an independent configuration grows as a large power of the gluino mass. So the $\kappa \rightarrow \kappa_c$ limit must be approached gradually in order to keep the systematic errors of the algorithm under

control. Secondly, in order not to suffer from finite volume effects, such as unnaturally constraining bound state correlation functions, the lattice size must suitably increased. The question of suitability of a given lattice size will be addressed in the course of our analysis.

Originally, the choice of β was based on the observation that for pure $SU(2)$ Yang Mills theory, $\beta = 2.3$ lies in the scaling region, where the continuum limit leaves the physics of the theory invariant. For $SU(2)$ -SYM, this is also expected to hold.

label	κ	lattice size	β	N_{config}	$N_{updates}$	N_{lat}
1925.12c	0.1925	$12^3 \times 24$	2.3	4320	216000	9
1940.12c	0.1940	$12^3 \times 24$	2.3	2034	42030	9
1940.16c	0.1940	$16^3 \times 32$	2.3	3890	25650	4
1955.12c	0.1955	$12^3 \times 24$	2.3	4272	65832	8
1955.16c	0.1955	$16^3 \times 32$	2.3	~ 520	~ 3500	2

Table 4.1: Overview of the ensembles used and/or produced in this work.

To give an idea of the algorithmic parameters, we summarized those of the new runs of the 1940.16c and 1955.16c ensemble in Table 4.2, where the parameter notation refers to that of Section 3.1.2. Here we see that for lighter gluino masses, higher orders of the polynomials are needed in the simulation. Simulations at hopping parameters closer to the critical κ_c entail a lower bound on the smallest eigenvalues of the fermion matrix Q . Therefore the interval of approximation must be enlarged to a smaller ϵ , creating the need for higher order polynomials. So in addition to the need for larger lattices, the simulation algorithm needs to be more refined in the polynomials.

	ϵ	λ	n_1	n_2	n_3
1940.16c	0.0001	4.0	28	420	500
1955.16c	0.00002	4.0	40	800	700

Table 4.2: Algorithmic parameters of ensembles 1940.16c and 1940.16c.

Figure 4.1 shows the history of the production run for the 1940.16c ensemble with respect to the plaquette and the smallest eigenvalue of the fermion matrix. From the experience of previous simulations performed by the collaboration [20], we conclude that we can skip the reweighting with respect to the correction factors in the measurement process (3.45), if the lowest eigenvalue stays above the lower limit of approximation, which is the case for almost the entire simulation run here. The few configurations that do not pass this criterion are simply excluded from the measurements, since they only contribute with negligible weight in the statistical average.

Similarly, on the set of configurations with smaller lattices, the sign of the Pfaffian was determined in [20] on sub-samples consisting of $\sim 10\%$ of the total ensemble by the use of the spectral flow method. It was found that in the region relevant

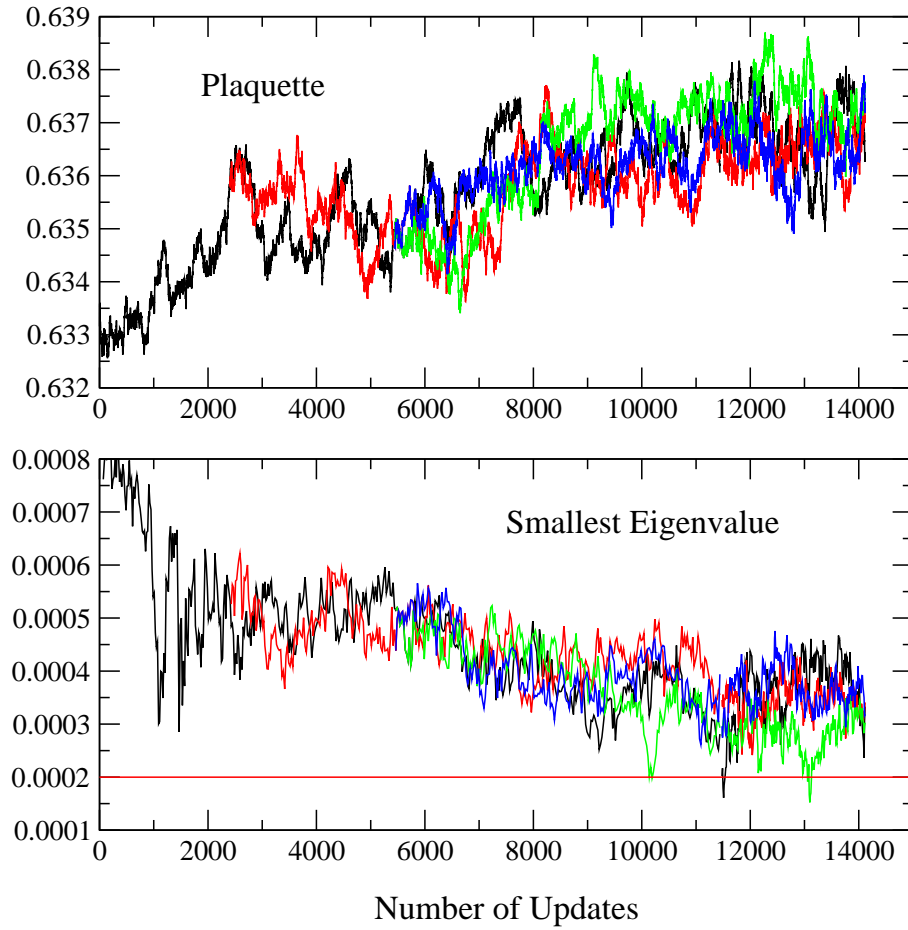


Figure 4.1: Run history of ensemble 1940.16c for the plaquette and the smallest eigenvalue up to $N_{\text{update}} \sim 14000$. The horizontal line in the lower panel shows the lower limit of approximation by the polynomial.

to the study, $\kappa \leq 0.196$, no zero-level crossings occurred. If we relate that to the findings of [18], where some negative signs were detected on a considerably smaller lattice ($6^3 \times 12$) with a lighter gluino of $\kappa = 0.196$, we conclude that for the 1940.16c ensemble, we are safe from zero level crossings. As hinted in the previous chapter, we therefore skip the measurement correction process entirely and take expectation values of operators at face value. It should, however, be noted that the closer one simulates to the critical κ_c , the more one should be alert to the negative signs. Therefore, when enough configurations are accumulated for the 1955.16c sample, an explicit check of negative Pfaffian signs should be performed.

4.2 Computational Results

In the following section we present two issues of computational interest. The first is the estimation of a sufficient number N_{est} of stochastic estimators for use in the determination of the a-meson masses. Secondly we will give a rather brief assessment of the numerical error we discovered for the VST in the previous chapter. Both analyses are based on a subset of the ensemble 1940.16c. The subset was chosen to obtain a maximum number of decorrelated configurations with respect to the smallest eigenvalue (see Section 4.4.3 for details).

4.2.1 SET Performance

With the use of stochastic estimators one needs to assess the number of estimates N_{est} sufficient to produce the desired matrix elements up to a given numerical accuracy. There are two considerations that need to be taken into account here, namely the convergence of the average value as the number of estimates increases and, secondly, the sufficient statistical suppression of the error. We explained in Section 3.5.2 our use of the spin explicit method, which is applied here throughout. So in studying the plots, one needs to remember that in fact one estimation is equivalent to two inversions of the fermion matrix (cf. Section 3.5.2). Since this was the first serious commitment of computational resources to the SET, being cost-conscious, we chose single (as opposed to double) precision for this study, i.e. our variables are declared as `float` (32bit) rather than `double` (64bit). As will be elaborated on later, this might have proven to be a mistake.

In Figure 4.2 the average value of the estimated quantity of interest $\text{Tr}[\Gamma Q^{-1}]$ for $\Gamma \in \{\mathbf{1}, \gamma_5\}$ is plotted for a single, randomly chosen configuration of the ensemble. We observe that after, approximately one hundred estimates, the value of each of the traces converges to a plateau within error bounds. This already gives us a good idea of the

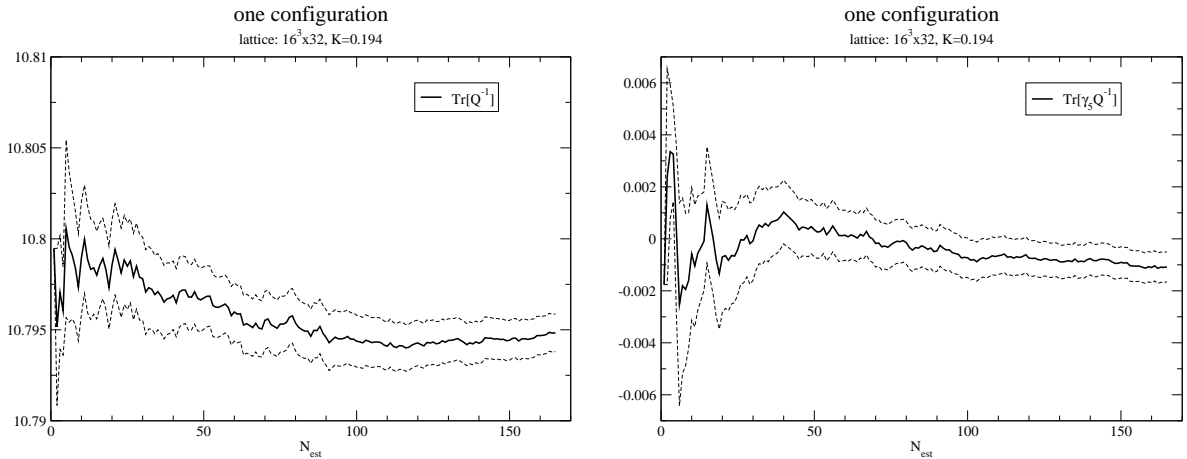


Figure 4.2: Evolution of the average value of $\text{Tr}[Q^{-1}]$ and $\text{Tr}[\gamma_5 Q^{-1}]$ as a function of N_{est} on single configuration. The dashed lines represent the error bounds.

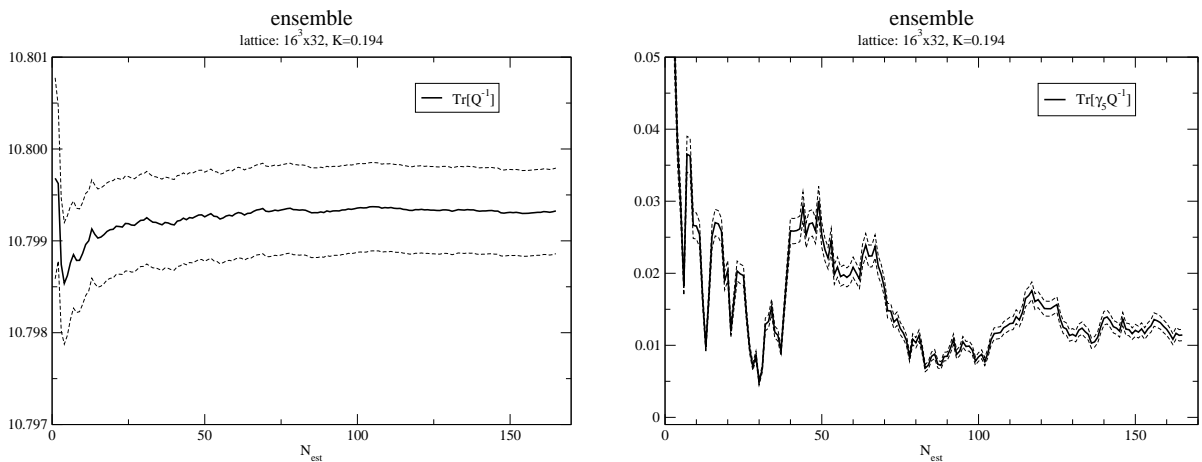


Figure 4.3: Evolution of the average value of $\text{Tr}[Q^{-1}]$ and $\text{Tr}[\gamma_5 Q^{-1}]$ as a function of N_{est} averaged over the complete ensemble 1940.16c. The dashed lines represent the error bounds.

order of magnitude N_{est} has to be. Note that the operator $\text{Tr}[\gamma_5 Q^{-1}]$ as a sum over time slices has a vanishing vacuum expectation value, since the vacuum is parity even. Yet this expectation does not apply here, since we are investigating a single configuration and a single configuration does not have to be representative of the physics of the whole ensemble. Only after averaging over the ensemble and therefore performing the path integral over different configurations, can one make use of the physical intuition, if available. In this light, it is entirely acceptable that the average value over stochastic estimates in the right panel of Figure 4.2 does not converge to zero, but in fact here to a value below zero, within the given statistical error.

When studying the average over the ensemble as a function of N_{est} in Figure 4.3, we can observe a different behavior between the $\Gamma = \mathbb{1}$ and $\Gamma = \gamma_5$ cases. Note in particular the different scales for the left and right panel. The former reaches a plateau within errors very quickly after about 50 estimates, while the latter takes considerably

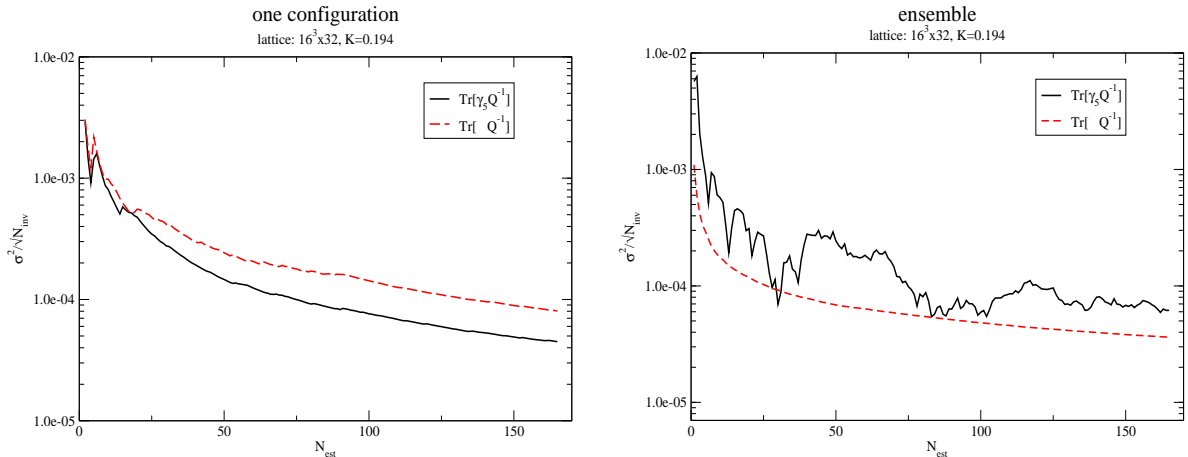


Figure 4.4: Evolution of the statistical error (3.137) of $\text{Tr}[Q^{-1}]$ and $\text{Tr}[\gamma_5 Q^{-1}]$ as a function of N_{est} for a single configuration (left) and averaged over the complete ensemble 1940.16c (right).

longer to converge. The most probable explanation of this mismatch is that for $\Gamma = \mathbf{1}$, the average value is a sum, while for $\Gamma = \gamma_5$, it is a sum of differences which relies on cancellations in order to converge to its expected value of zero. As such, it is drastically more sensitive to possible numerical inaccuracies. In an equivalent study with increased precision (i.e. double precision) it would be worthwhile to study this effect more closely. Nevertheless, we observe that after about 150 estimates, the value of the pseudo-scalar trace converges, albeit to a non-zero value. We see the failure to reach the theoretical value of zero as a further argument for the interpretation that, even in the ensemble average, the necessary cancellations are possibly impaired by insufficient numerical accuracy.

Focusing on $\Gamma = \mathbf{1}$, we see very clearly that the measured error is more or less of constant size. This demonstrates beautifully the property of the SET that in the limit of $N_{\text{est}} \rightarrow \infty$, the estimation error is suppressed and we are left with an error that is completely generated by the fluctuations of the ensemble itself. This property of the disentanglement of systematics and statistics was our original motivation for the use of this method.

Finally, we compare the average error reduction per estimate (3.137) in Figure 4.4. Again, we first look at a single configuration (left panel). As one might expect from the use of the SEM, the relative error in the pseudo-scalar case performs slightly better than the scalar, but both are of comparable size. One could expect that, since the relative precision of 32bit variables is approximately 10^{-6} , we would observe that the error approaches approximately this value. But due to limited computational resources we chose to break off beforehand. When viewing the ensemble average, we are again confronted with the relative instability of the pseudo-scalar case. However, both errors stay of $\mathcal{O}(10^{-4})$, which we regard as acceptable.

In conclusion, we fix the N_{est} to be 150, which we expect will deliver us an error by and large independent from the statistical fluctuations of SET. It should be noted that for stochastic estimation techniques in this context, there are in fact more advanced techniques for variance reduction on the market [45] which could be tested in the future.

4.2.2 VST Error Analysis

The spurious piece detected in the two-loop correlator (3.126) when applying the volume source method warrants a numerical investigation, since it is unclear how to assess its size or its impact on the actual object of our interest, the masses of the relevant particles. The classical algorithm for the VST is to generate one estimate $\mathcal{E} [\text{Tr}[\Gamma Q^{-1}]]$ for every field configuration, calculate a correlator from that estimate and average correlators over the ensemble, i.e.

$$C^{VST} = \langle C \rangle_{\Omega} = \left\langle C(\mathcal{E} [\text{Tr}[\Gamma Q^{-1}]]) \right\rangle_{\Omega}, \quad (4.1)$$

where $\langle \dots \rangle_{\Omega}$ denotes the average over the ensemble Ω . For the analysis, our strategy is to compare the method of generating K estimates of one configuration $\mathcal{E}_k [\text{Tr}[\Gamma Q^{-1}]]$, each separated by a random gauge transformation, calculating a correlation function for each individual estimate and then averaging those correlation functions over gauge transformations and the ensemble:

$$C_{wrong}^{VST} \equiv \left\langle \langle C(\mathcal{E}_k [\text{Tr}[\Gamma Q^{-1}])) \rangle_g \right\rangle_{\Omega}, \quad (4.2)$$

where $\langle \dots \rangle_g$ denotes the average over K random gauge transformations. This is contrasted with first averaging the estimates of one configuration over random gauge transformations, *then* calculating a correlator, and finally averaging these correlators over the ensemble

$$C_{correct}^{VST} \equiv \left\langle C(\langle \mathcal{E}_k [\text{Tr}[\Gamma Q^{-1}]] \rangle_g) \right\rangle_{\Omega}. \quad (4.3)$$

Note in particular the difference in the order of averaging and calculating correlations between (4.2) and (4.3). By using the correct version, the extra piece is averaged away from the beginning, while in the wrong version it should appear. In passing, we remark that, indeed, (4.3) is a novel way of thinking about the VST and in consequence applying it. Seen in this way, it is more akin to the SET, since we could choose to apply the above SET analysis in exactly the same fashion, replacing repeated stochastic estimates with repeated random gauge transformation and subsequent VST estimates. From that perspective, one could separate the statistical and the systematic error by the same logic. It is then merely a question of numerical performance in terms of noise suppression that would make one method preferable to the other.

As in the SET analysis, we first compare average correlators of a randomly chosen, single configuration (i.e. not taking the average over Ω in (4.2) and (4.3)) and then

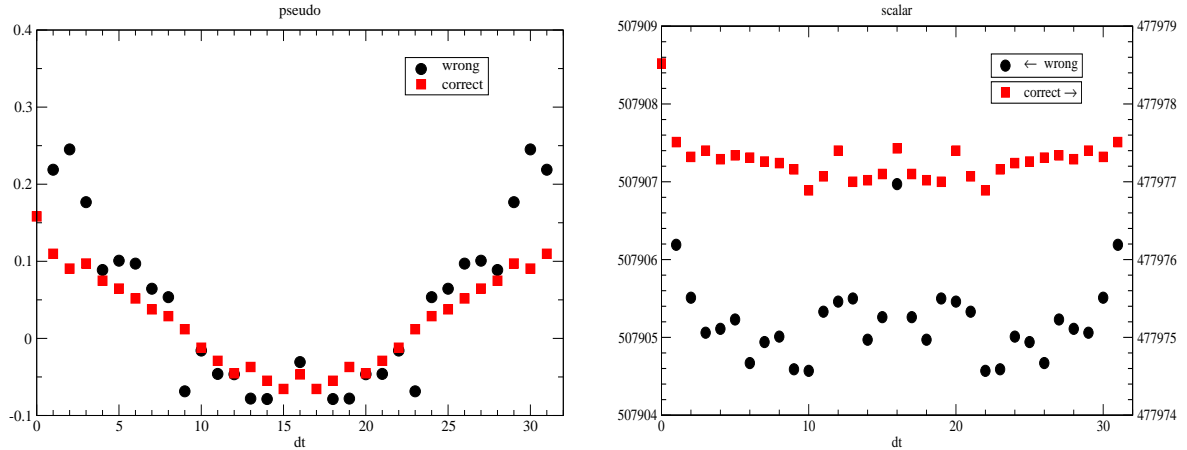


Figure 4.5: Comparison of the disconnected correlator $C_{\bar{g}g}(\Delta t)_{disc.}$ in (3.103) for $\Gamma = \gamma_5, \mathbb{1}$ on a single configuration. For the definitions of correct (boxes) and wrong (circles) see text. Note the different scales on the y-axes in the right panel.

look at the ensemble average to see, whether the erroneous piece might average away due to yet unfound symmetries that only become apparent in the ensemble average. Finally we assess its impact on the mass determination. The number of random gauge transformations and estimates applied was fixed to $K = 15$.

We can see from Figure 4.5 that the correlators for a single configuration are indeed different. In the pseudo-scalar channel (left panel) it is not as pronounced as in the scalar (right panel), where we chose to have different scales to make them comparable. In both cases, the wrong version produces a “noisier” signal that deviates markedly from a clean correlation function. In the scalar case, the offset is –purely numerically– quite consistently ~ 25531 which is approximately of the order of the volume $\mathcal{O}(L^3 \times T) = \mathcal{O}(10^4)$ of the lattice.

In the ensemble average, the “noisiness” of the wrong method has averaged away, most strikingly for the pseudo-scalar (see Figure 4.6, left panel). The statistical errors are similarly large for the pseudo-scalar case, while for both cases, generally, at low time separation the wrong method produces higher correlations than the correct. In addition, for the scalar, we observe that the offset we saw on the single configuration has manifested itself. However, from $\Delta t = 5$ onwards, both correlations are virtually the same, modulo the offset and the size of the error in the scalar case. This implies that the error is a constant for large Δt . But interpreting the pseudo-scalar correlator seems to suggest that the difference is absorbed into a larger amplitude.

A separate remark concerning the error of the scalar correlator needs to be made here. We see that, disregarding other discrepancies, the wrong method produces an offset and an enormous difference for the statistical error. To get the true correlation, we need to subtract the non-zero vacuum expectation value (VEV) from the correlator, $v = \langle \text{Tr}[Q^{-1}] \rangle$. The definition of the VEV itself implies though that it cannot be

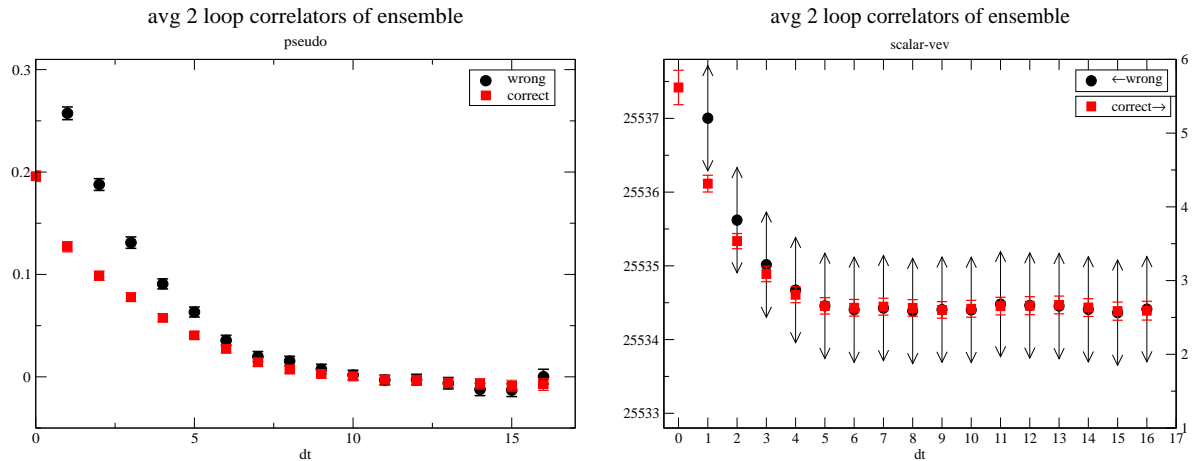


Figure 4.6: Comparison of the disconnected correlator $C_{\bar{g}g}(\Delta t)_{disc.}$ in (3.103) for $\Gamma = \gamma_5, \mathbb{1}$ averaged over the complete ensemble 1940.16c. For the definitions of correct (boxes) and wrong (circles) see text. Note the different scales on the y-axes in the right panel.

calculated wrongly in the above sense, since the error term only appears in correlation functions, i.e. the estimate of the VEV is the same for the two methods. This has two implications for the wrong method. Firstly, as we witness from the plot 4.6, it produces the familiar offset. Secondly, the correct subtraction of the VEV within a Jackknife error analysis reduces the variance of the subtracted correlator significantly, since the VEV and the non-subtracted correlator are strongly correlated. Within the incorrect framework, this numerical effect is completely missed. Moreover, it is turned into its opposite, since the correct VEV is subtracted from the wrong correlator, increasing the already very large variance. The result can be seen in the markedly different size of the error bars in the right panel of Figure 4.6.

Somewhat surprisingly, the larger values of the correlations do not greatly influence the mass calculations, see Figure 4.7. We will concentrate on the pseudo-scalar case, since the data simply is not good enough to extract a viable $a-f_0$ mass, as can be clearly seen in Figure 4.7, right panel. To get better data, one would have to increase the number of estimates per configuration and possibly the number of independent configurations.

The largest deviations between the two methods occur at the high t_i -end for the global fits and the high t for effective masses respectively. Except for some sporadic cases, the values agree with each other within errors. But one still needs to be cautious before arguing the irrelevance of the mismatch of the two methods for the masses for this particle. The comparison was made for only a relatively low number of estimates per configuration. It might well be possible that with higher quality of the data we would detect a measurable impact. It might also be possible, though, that the erroneous piece in (3.126) with $\Gamma = \gamma_5$ is not invariant under other non-trivial symmetries of the vacuum that manifest themselves in the ensemble average and therefore might not play a role for the $a-\eta'$.

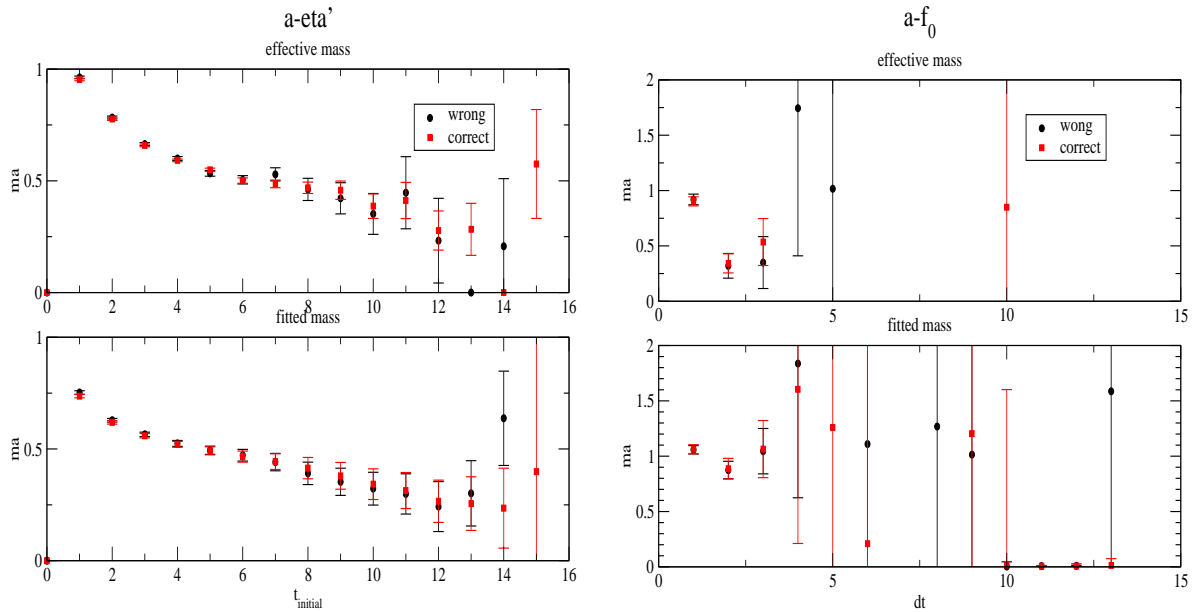


Figure 4.7: Comparison of masses obtained from the combined correlator in (3.103) for $\Gamma = \gamma_5, \mathbf{1}$ for the ensemble 1940.16c by global fits and effective masses. For the definitions of correct (boxes) and wrong (circles) see text.

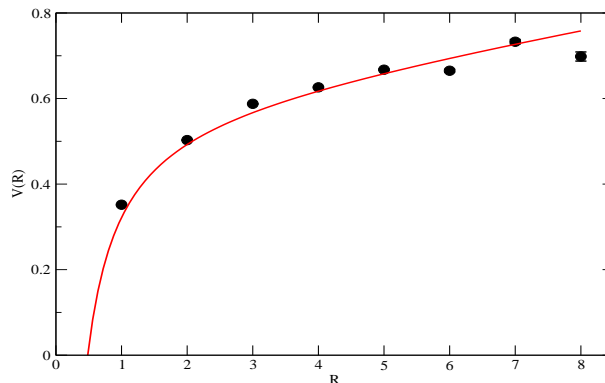


Figure 4.8: Static potential and fit of ensemble 1940.16c.

4.3 Static Potential

As explained previously, it is assumed that the property of confinement holds also for the four dimensional $N = 1$ SYM theory. This amounts to the conjecture that the adjoint fermion loops have no substantial screening effect on fundamental sources. As can be seen in Figure 4.8, there is no plateau at high R for the ensemble 1940.16c, which could be interpreted as screening. The line is the corresponding fit to (3.69), resulting in the R_0 and string tension shown in Table 4.3. This judgment is perfectly in line with the previous experience of the collaboration [22, 18]. The values for the 12c ensembles were determined in [21] and are recorded here for reference and comparison. Of particular interest is the possibility to directly compare the 1940.12c with the 1940.16c ensemble. We observe almost identical values for R_0 and $\sqrt{\sigma}$, which leads

us to the conclusion that, at least for gluonic quantities, we are free of finite volume errors from 12c onwards.

ensemble	Sommer scale R_0/a	L_x/R_0	string tension $a\sqrt{\sigma}$
1925.12c	6.71(19)	1.79(5)	0.176(4)
1940.12c	7.37(30)	1.63(7)	0.160(6)
1940.16c	7.16(25)	2.2(1)	0.165(9)
1955.12c	7.98(48)	1.50(9)	0.147(8)
1955.16c	7.3(5)	2.2(15)	0.161(11)

Table 4.3: Sommer Scale and string tension results for the investigated ensembles.

From a numerical point of view, one can compare these scales with QCD. It has to be stressed, though, that the analogy should not be pushed too far, since after all, we are comparing two different theories. With that in mind, in QCD the experimental value of R_0 as defined in (3.72) is $R_0^{QCD} = 2.53 \text{ GeV}^{-1}$. This would give us a rough estimate for the lattice spacing of $a \sim (3.15 \text{ GeV})^{-1} \approx 0.06 \text{ fm}$ for $\kappa = 0.1955$, and therefore the size of the box is roughly 0.7 fm across, which for QCD would be rather small. Common lattice lore requires a sufficient size to be $\sim 2 \text{ fm}$. But as we saw for the gluonic sector, we are likely to be free from finite volume effects.

4.4 Masses

We finally turn to the determination of the masses for the measured operators. As we know from Section 3.4, the simulation generates a Monte Carlo estimate $\overline{G_{\mathcal{O}}(\Delta t)}$ of the correlator for a given operator \mathcal{O} at a finite number of time separations $0 \dots N_t$. From theory, the exact form of a correlator is a sum of exponentials (3.77). The goal in fitting the data is to find a t_{min} and a t_{max} , where the higher states have died off (t_{min}) but where there still is a good signal for the (second) lightest (t_{max}) so that in the following mass fits one hopefully gets a plateau, where the lightest mass (or both masses in two mass fits) stabilizes.

4.4.1 Details of Mass Fits

Fitting a function to a set of data is a minimization procedure, which seeks to minimize the quantity known as χ^2 . Its definition is

$$\chi^2 = \sum_{i=1}^N \frac{(y_i - y(x_i; a_j))^2}{\sigma_i^2} \quad (4.4)$$

where $y(x_i; a_j)$ represents the fit to a function $y(x)$ depending on the fit parameters a_j . Further, $y_i \pm \sigma_i$ are the measured values at points x_i , in this case the correlation $C(x_i)$ with $x_i = (\Delta t)_i$ and N the number of data points. Probability theory tells us that, at the minimum of χ^2 , lie the most probable values for the fit parameters [46]. For reference, the fitting routines were implemented with the help of the *GNU Scientific Library* [47] using a Levenberg-Marquardt solver with derivatives.

In order to reduce the freedom of possible parameters for the fitter and thus numerically stabilize the fits, the amplitudes and masses were parameterized as $a_n = \sqrt{A_n}$ and $\varepsilon_n = \sqrt{E_n}$ to enforce their positivity. The resulting fitting function then is

$$G(t) = \sum_{n=1}^N a_n^2 \left(e^{-\varepsilon_n^2 t} \pm e^{-\varepsilon_n^2 (T-t)} \right) \quad (4.5)$$

with $N = 1, 2$ for one mass and two mass fits respectively. Other parameterizations are found in the literature, notably $a_n = \log A_n$ and $\varepsilon_n = \log(E_n - E_{n-1})$ and variants thereof. These were found to render the minimization routine unstable due to the large gradients that were computed during the fit. The same behavior was found for $\varepsilon_n = \sqrt{E_n - E_{n-1}}$.

As we will see below, often enough we are faced with the situation where a one mass fit produces a hopeless result, i.e. no plateau is visible and a two mass fit is unreliable due its freedom to choose four, or even five, if the correlator has an offset from zero, different values for the fit parameters. The failure of a fit to produce a plateau can have a number of reasons. First and foremost, the correlator can contain a considerable signal for another, higher state. In this case, we expect the gradual reduction of the fit interval to higher time separations to produce masses that are consistently too large, because the sum of N exponentials falls off faster than a single one, since

$$\partial_t(e^{-mt} + \frac{a_1^2}{a_n^2} e^{-Mt} + \dots) < \partial_t(e^{-mt}) . \quad (4.6)$$

This will fail to produce a plateau, if the signal of the higher state(s) is strong enough at large t . Furthermore, we expect the overestimate of the mass to decrease for higher t_i , as the higher states die off successively. Within this scenario it is also quite possible that the next higher state is not far off from the lightest, thus its fall off is delayed, nevertheless giving bad results for one mass fits. Secondly, the signal/noise ratio at larger time separation may decrease faster than the suppression of higher states in the correlator, such that any signal is lost completely and reliable conclusions cannot be drawn. In the second case, the smearing of operators has proven to be a helpful tool (for details, see the appendix A.3). The idea is to improve the signal by increasing the overlap of the operator with the wave function of the lightest state. Essentially, one seeks to maximize the amplitude c_1 in (3.77) relative to the other amplitudes.

Our strategy in dealing with first case is the following. From the unstable two mass fit, we take hints for the possible mass of a higher state, which naturally has some

detectable signal, since it was a result of the fit. We then feed this information back by subtracting the contribution of the supposed second exponential from the actual measured correlation function. Let the mass M and the amplitude A be the a priori untrusted suggestions from the two mass fit. We then attempt to fit

$$\overline{G(\Delta t)'} \equiv \overline{G(\Delta t)} - A(e^{-M\Delta t} \pm e^{-M(t-\Delta t)}) \rightarrow c(e^{-m\Delta t} \pm e^{-m(t-\Delta t)}) \quad (4.7)$$

which will either produce some signal or almost none, depending on the quality of the guess. Repeating this procedure over the range of suggested M and A , we single out the best signal and subject it to a stress test by automatically scanning below and above the chosen values of M and A . If the results are stable under this test, we read off the lowest mass from the one mass fit. As a cross-check, we then subtract the exponential with the lower mass from the measured correlator to see whether the higher mass M is reproduced. This procedure might seem cumbersome at first sight. Nevertheless we found it to produce the most reliable results in this study.

4.4.2 Gluino-Glue Bound States

We begin with the investigation of the gluino-gluon particle. As we already saw, we can split up the correlation function into a part that is proportional to $\mathbb{1}$ and one that is proportional to γ_0 (3.99),

$$C^{\alpha\beta}(\Delta t) = C_1(\Delta t)\delta^{\alpha\beta} + C_2(\Delta t)\gamma_0^{\alpha\beta} \quad (4.8)$$

where the two parts have different periodicity. To exemplify this behavior for all ensembles, we show the two corresponding correlation functions of the 1940.16c ensemble in Figure 4.9. Note here especially the excellent signal/noise ratio, as indicated by the tiny error on these points and the exact symmetry as predicted by equation (3.100). For the corresponding plot with symmetrized correlation functions in Figure 4.10, we chose a logarithmic scale to again highlight the good quality of the signal. Of interest here is also the non-linear character which indicates that we indeed do not have a single exponential, but a sum of two or more, reflected at T . This can be seen from the pronounced deviation of the linear behavior in the log-plot at large time separation Δt .

The structure of the following section is such that we first analyze the small lattices ($L_x = 12$) while going from small κ to larger, i.e. from heavier to lighter bare gluino mass. This is followed by the large lattice ($L_x = 16$), for which up to now we only have a viable ensemble at $\kappa = 0.194$.

On all lattices we used both APE and Jacobi smearing for the sink and the source. The primary point of reference was the previous analysis [19]. We found exactly the

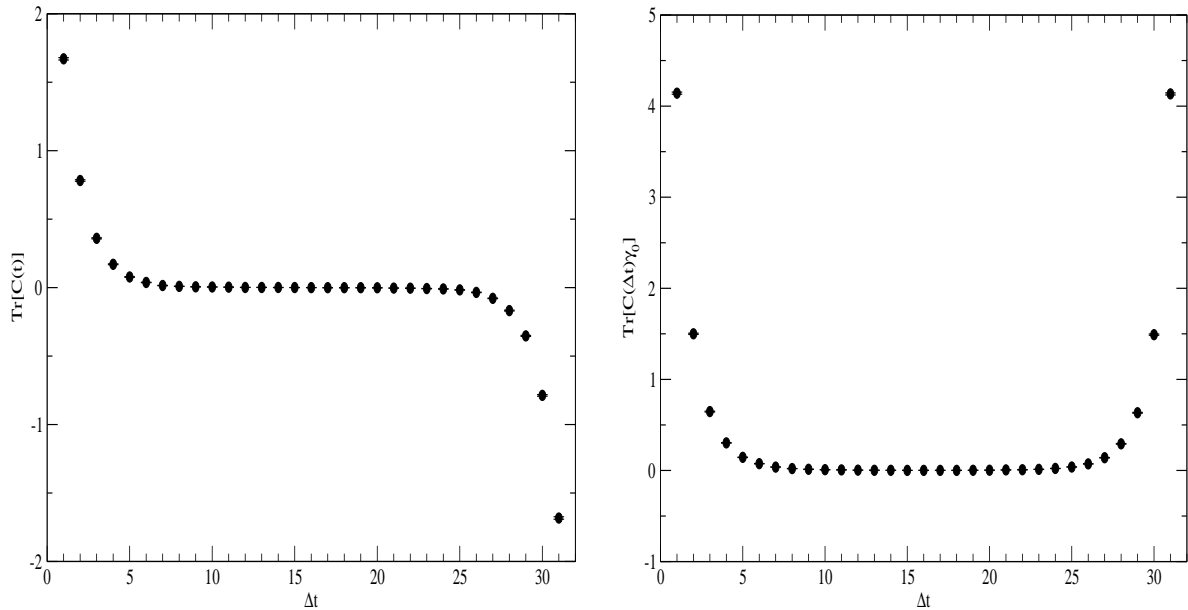


Figure 4.9: Gluino-gluon correlation function for $C_1(\Delta t)$ and $C_2(\Delta t)$, as defined in the text.

same parameters for APE and Jacobi smearing to produce the best signal. So for the complete analysis of the gluino glue, we used

$$N_{APE} = 9, \quad \epsilon_{APE} = 0.5 \quad \text{and} \quad N_{Jacobi} = 18, \quad \kappa_{Jacobi} = 0.2, \quad (4.9)$$

just as [19]. As a general observation, pertaining to all of the studied ensembles, the $C_{\gamma_0}(\Delta t)$ data seems to give a better signal than the $C_{\mathbb{1}}(\Delta t)$. We do not have a sound explanation for that fact. However, in [19] the same was found to be true. A possible reason for this could be that the smearing procedure creates a larger overlap of the wave function with one spin-Lorentz structure than the other. Nevertheless, it is an open question.

Ensemble 1925.12c

This ensemble was already analyzed with respect to the gluino-gluon in [19]. We used it as a reference and cross-check in order to fine tune our own fitting procedures. It should be mentioned that we are unable to reproduce the two-mass fit quoted there.

Fitting the $C_{\gamma_0}(\Delta t)$ data to the one mass ansatz, we see the definite influence of other states, hindering the emergence of a plateau (see Figure 4.11). Neither does the effective mass ansatz help here (cf. equations (3.83) and (3.83)). But since the effective mass is a more local property, one could optimistically say that there is something akin to a plateau in the high Δt region. This picture shows almost exactly, what was found in the analysis in [19].

By subjecting the $C_{\gamma_0}(\Delta t)$ correlator to a two mass fit, we get extremely unstable

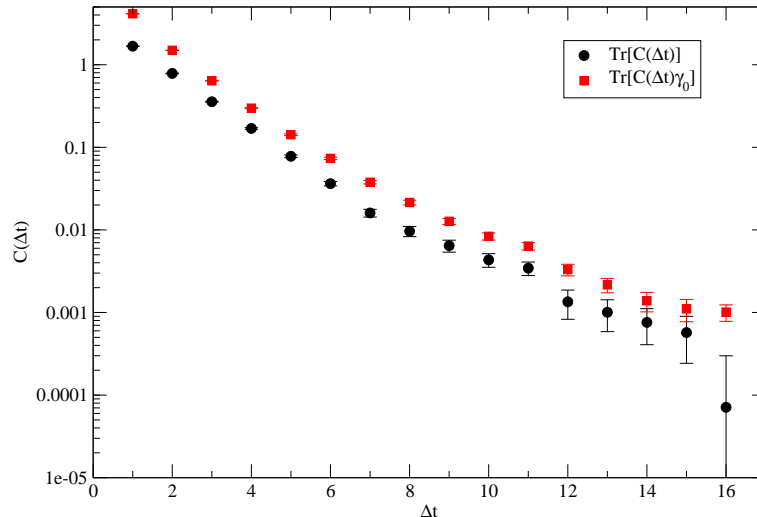


Figure 4.10: Symmetrized gluino-gluon correlation functions $\text{Tr}[C_{\tilde{g}g}]$ and $\text{Tr}[C_{\tilde{g}g}\gamma_0]$ for the 1940.16c ensemble.

results, as might be expected, when judging the quality of the data from Figure 4.11. This is the first instance where we apply our subtraction procedure outlined above. It is found that when subtracting a higher mass of

$$am_{high} = 0.949(\dots) \quad (4.10)$$

we get a stable fit. This becomes particularly evident from Figure 4.12, where we witness a plateau on the lower mass (circles) over a wide range of fit intervals, starting from $t_i = 2$. Moreover, when repeating the procedure, as indicated above, by subtracting the contribution of the small mass from the correlator, we indeed regain the signal for the higher mass (boxes). Consistent with our above discussion of the fitting routine, one also sees that for fit intervals with larger t_i , the signal of the higher mass is fading, as indicated by the increasing error. Thus we quote the lightest mass on this ensemble as

$$am_{low} = 0.33(4) . \quad (4.11)$$

Comparing with [19], and therein Table 3.7 at $t_i = 9$, we indeed find a weak signal for a value of the mass in this region which we take to be a corroboration of our result. We interpret the slight fall off of the subtracted mass fit in Figure 4.12 as a statistical effect, since those values are still, within their respective error, compatible with the clear plateau. As the value for the higher mass we find

$$am_{high} = 0.95(3) . \quad (4.12)$$

Unfortunately, in the case of the $C_{\mathbb{1}}(\Delta t)$ component (Figure 4.13), we already find a clear signal in the one mass fits, which is not compatible with the value obtained for the $C_{\gamma_0}(\Delta t)$ correlator, i.e. it is much higher. The effective masses and the global fitted

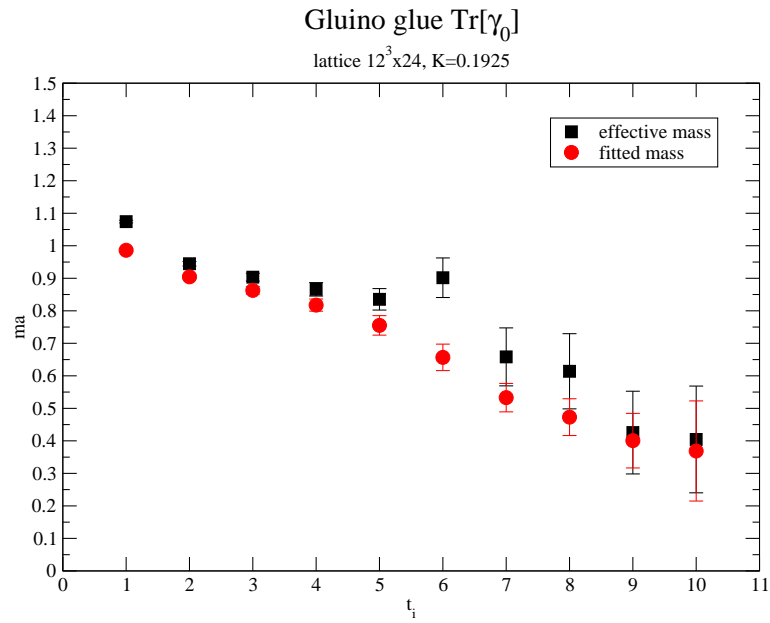


Figure 4.11: Effective mass and one mass fit to the $\text{Tr}[C_{\bar{g}g}\gamma_0]$ correlator for the 1925.12c ensemble.

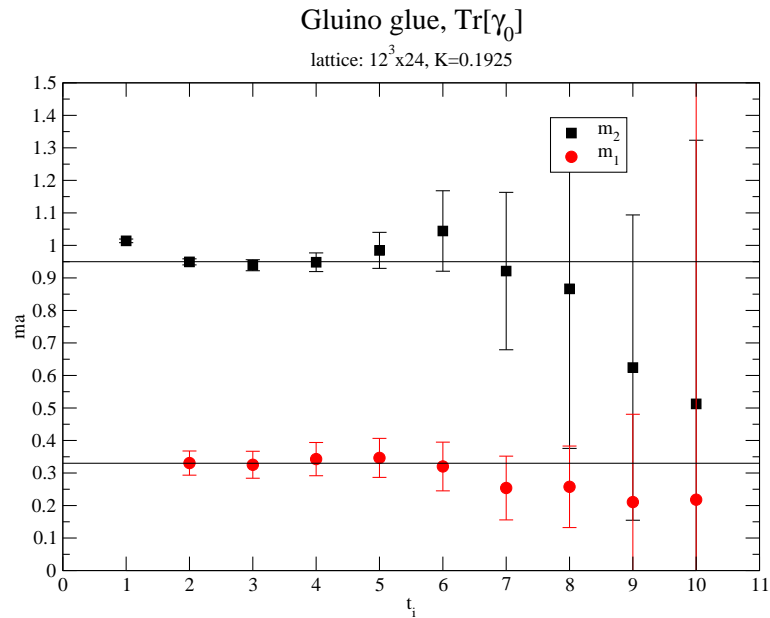


Figure 4.12: One mass fit to the subtracted $\text{Tr}[C_{\bar{g}g}\gamma_0]$ correlator for the 1925.12c ensemble.

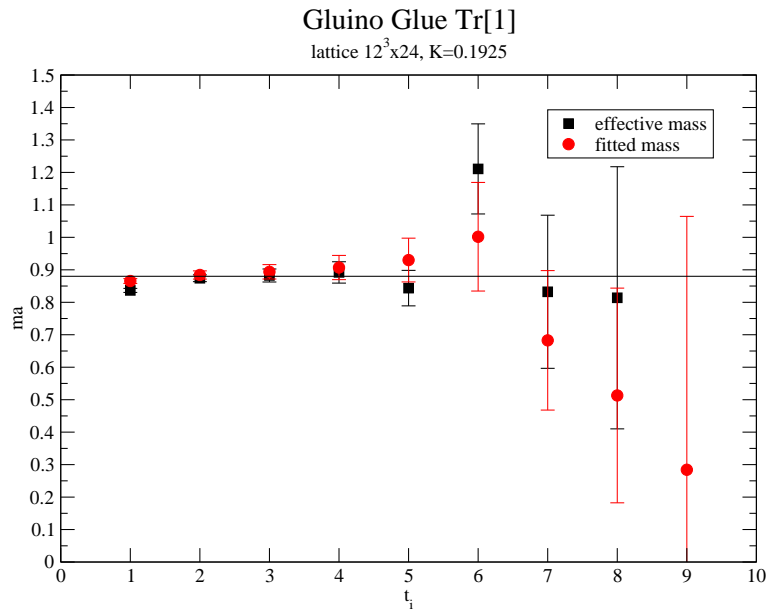


Figure 4.13: Effective mass and one mass fit to the $\text{Tr}[C_{\tilde{g}\tilde{g}}]$ correlator for the 1925.12c ensemble.

masses agree on this too. However, we notice from $t_i = 7$ onwards, that the results from the mass fits begin to drop. This could be evidence for the fall-off of the heavier mode in the correlator. This would lead us to the suspicion that the lattice extent is too small, since it is possible that a plateau will emerge beyond these values of t_i . So failing to extract a lighter mass in this channel, we quote as our best estimate

$$am = 0.88(1) . \quad (4.13)$$

We see here the first instance of the general observation we described above, namely that the quality of the $C_{\gamma_0}(\Delta t)$ correlator data is substantially better than that for the $C_{\mathbb{1}}(\Delta t)$.

Ensemble 1940.12c

As we move to a lighter gluino, we find that the $C_{\gamma_0}(\Delta t)$ correlator on this data set behaves similarly to the $C_{\mathbb{1}}(\Delta t)$ on the previous. The one mass fit of Figure 4.14 shows that the fits over large intervals, i.e. from t_i to $t_f = 12$, produce a significant signal at $am \simeq 0.82$. Again, the fitted mass drops considerably for higher t_i , hinting at the existence of a lower mass in the correlator. If we take the high mass at face value and eliminate its contribution from the correlation, we find what is plotted in Figure 4.15.

We see that we are in fact able to extract a signal for a lower mass, although it vanishes from $t_i > 7$. This might be due to the fact that here the higher mass also starts to drop as the signal fades and one is only left with the lowest mass. The approximation

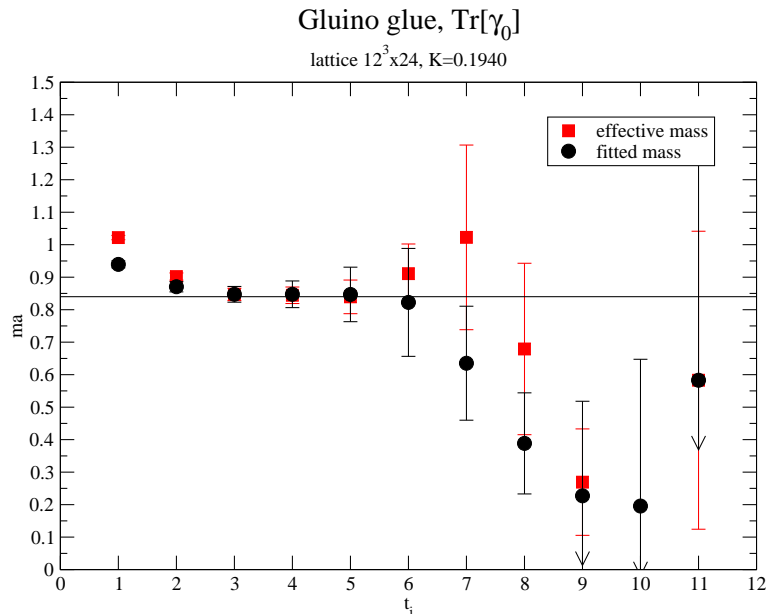


Figure 4.14: Effective mass and one mass fit to the $\text{Tr}[C_{\tilde{g}g}\gamma_0]$ correlator for the 1940.12c ensemble.

one makes by subtracting the higher mass from the correlator necessarily goes astray. Nevertheless, as above, the fit results shown in Figure 4.15 reproduce each other. So we are confident that these are the relevant masses and estimate them to be

$$am_{low} = 0.49(4) \quad \text{and} \quad am_{high} = 0.85(2) . \quad (4.14)$$

For the second component of the correlator, $C_1(\Delta t)$, we find a similar outcome. Figure 4.16 displays the results of its one mass fit. As in the 1925.12c case, it was not possible to extract a lower mass by our subtraction procedure. This can be attributed to the fact, that we do not observe the typical fall-off like for the $C_{\gamma_0}(\Delta t)$, which would suggest a lighter mass. Effective mass determination and fitted mass give consistent results. Keeping in mind that this might not be the lowest mass for this correlator, we estimate it to be

$$ma = 0.80(2) \quad (4.15)$$

which seems more in line with the higher mass found for the $C_{\gamma_0}(\Delta t)$ component.

Ensemble 1955.12c

By now, the reader is familiar with our approach in extracting the masses of the lightest states in the correlation functions for the gluino-gluon particles. So for this ensemble we simply show in Figure 4.17 the result of an unconstrained one mass fit and in Figure 4.18 the result, as obtained by the elimination of the contribution of a higher mass,

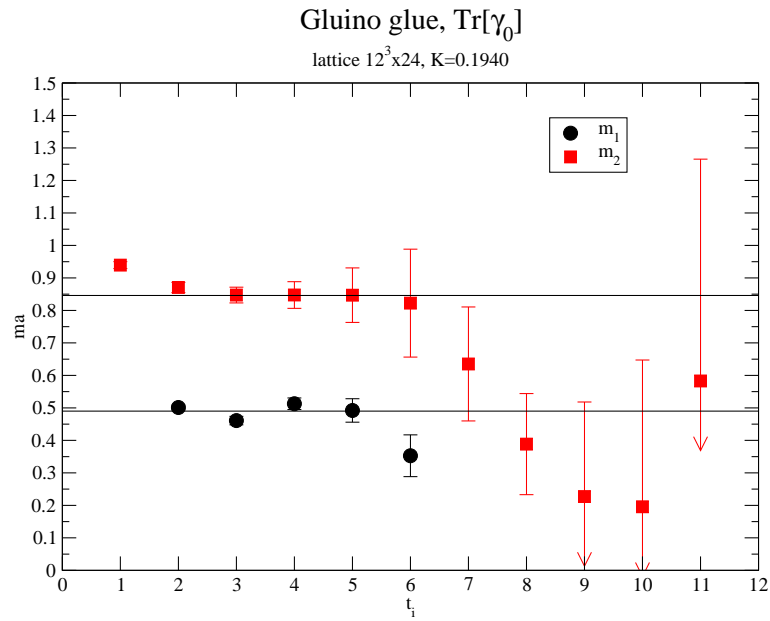


Figure 4.15: One mass fit to the subtracted $\text{Tr}[C_{\bar{g}g}\gamma_0]$ correlator for the 1940.12c ensemble.

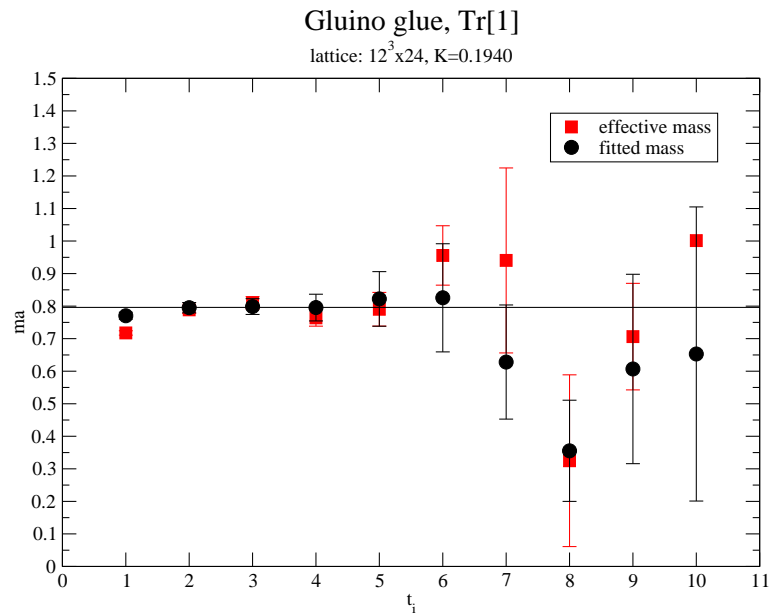


Figure 4.16: Effective mass and one mass fit to the $\text{Tr}[C_{\bar{g}g}]$ correlator for the 1940.12c ensemble.

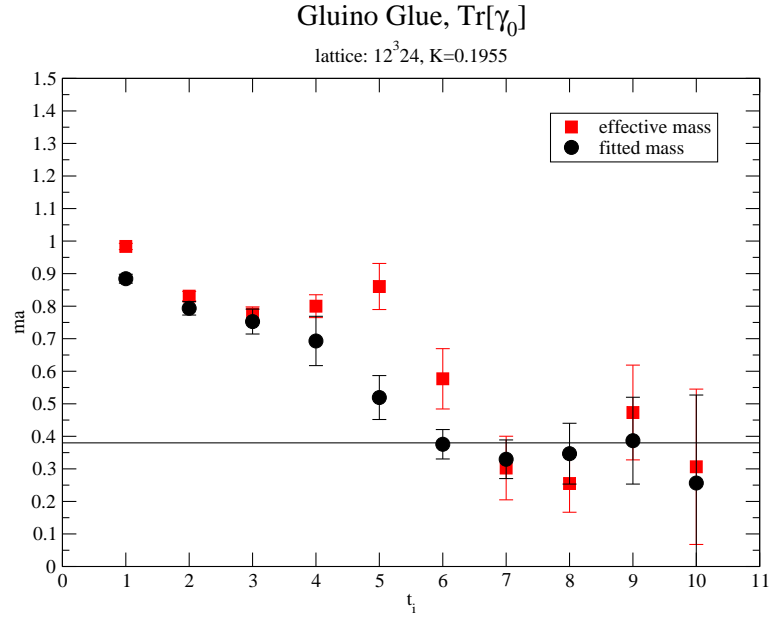


Figure 4.17: One mass fit and effective mass of the $\text{Tr}[C_{\bar{g}g}\gamma_0]$ correlator for the 1955.12c ensemble.

$am_{high} = 0.984(\dots)$, which is the approximate value one expects from the experience above. Unfortunately, the mutual cross-check of subtracting the contribution of the lighter mass in this case is inconclusive, most probably due to the fact that the heavier mode dies off very quickly. Nevertheless we get a result that stays impressively stable over a wide range of fit intervals, leading to an estimate of

$$am_{low} = 0.35(4) . \quad (4.16)$$

For the $C_{\perp}(\Delta t)$ channel, a rather intriguing result is found (see Figure 4.19). Just trying a one mass fit, one finds an extremely stable plateau (within errors) right from the start of $t_i = 1$. This is insofar intriguing, as the value for this mass is higher than the range for the lower masses we found in the cases above, but the hope of finding a low mass here is clearly faint, as is confirmed by numerical analysis. Thus, our best estimate for the gluino-gluon mass for this component of the correlator is

$$am = 0.66(4) , \quad (4.17)$$

where we again judiciously omitted the index $(\dots)_{high}$ or $(\dots)_{low}$ for this quote.

Ensemble 1940.16c

We now turn to the larger lattice, which without doubt produces the cleanest results for the gluino-gluon in this study. For the $C_{\gamma_0}(\Delta t)$ correlator, the primary result is

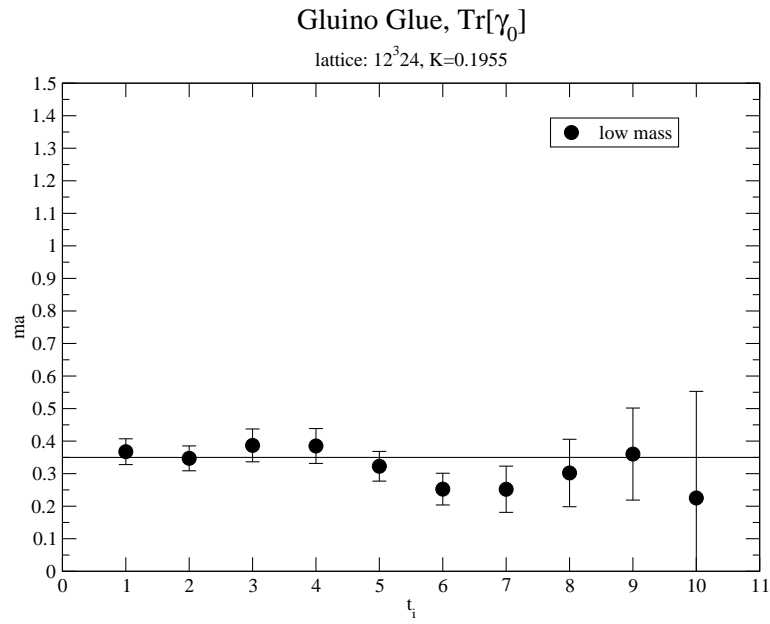


Figure 4.18: One mass fit to the subtracted $\text{Tr}[C_{\tilde{g}g}\gamma_0]$ correlator for the 1955.12c ensemble.

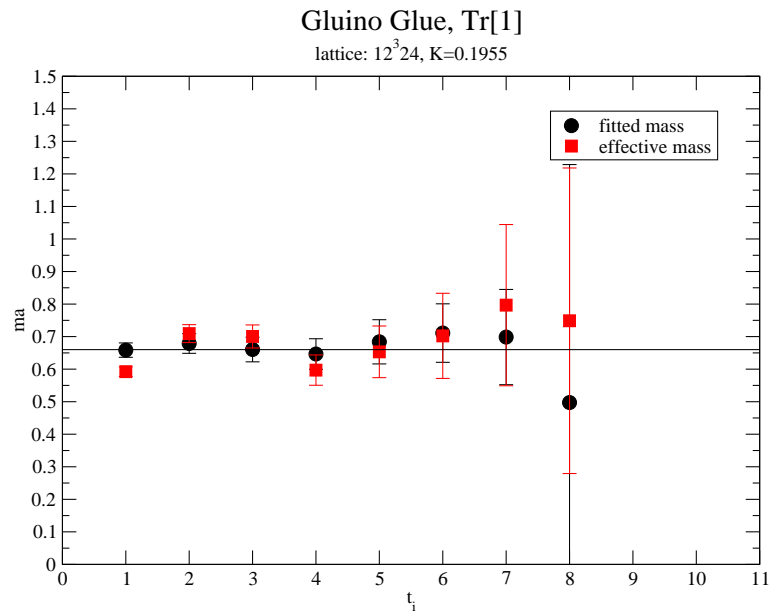


Figure 4.19: Effective mass and one mass fit to the $\text{Tr}[C_{\tilde{g}g}]$ correlator for the 1955.12c ensemble.

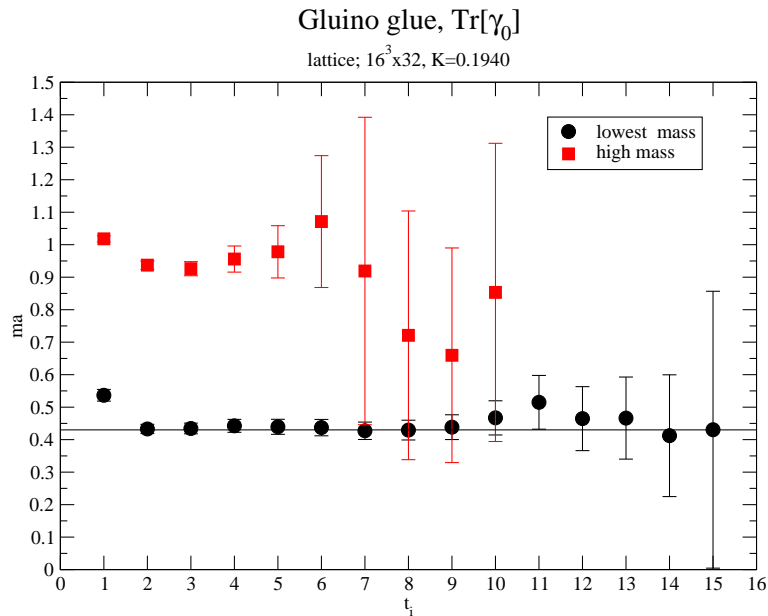


Figure 4.20: One mass fit to the subtracted $\text{Tr}[C_{\tilde{g}g}\gamma_0]$ correlator for the 1940.16c ensemble.

shown in Figure 4.20. By identifying the higher mass to be

$$am_{high} = 0.85(2) \quad (4.18)$$

and again subtracting its contribution from the correlation function we find the lower mass to exhibit a plateau over almost all possible fit ranges of the lattice. As an estimate, we get

$$am_{low} = 0.43(1) . \quad (4.19)$$

This result is beautifully confirmed for the plain one mass fit shown in Figure 4.21. Here we most clearly see the fall-off of the mass fits until the higher states have died off and only the lightest mode survives, resulting in a plateau (as usual within errors). The estimate from this plateau

$$am_{plateau} = 0.49 \quad (4.20)$$

is only slightly higher than the above, which we believe is firmer due to its stretched out plateau of Figure 4.20. By virtue of the high quality of the data, another interesting effect can be noticed in Figure 4.21. We see that before the plateau emerges, the global mass fit consistently produces a lower mass than the effective local mass. Looking at $t_i = 1$ or $t_i = 2$, the global fit uses the full interval from this t_i onwards up to $t = T/2 = 16$ to get an estimate while the local mass essentially computes the logarithm of the ratio $C(t_i)/C(t_{i+1})$. This means that in the global fit, the contribution of the lightest state is fully taken into account, while the local mass completely ignores it. So it becomes clear that the local mass results in a higher estimate than the global, since at small time separations, the correlator is dominated by the higher states.

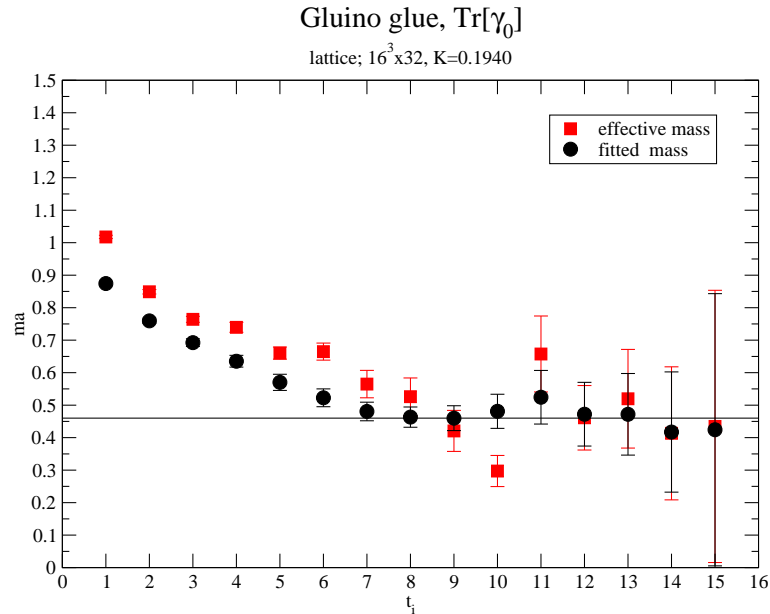


Figure 4.21: One mass fit to the full $\text{Tr}[C_{\tilde{g}g}\gamma_0]$ correlator for the 1940.16c ensemble.

Turning our attention to the $C_{\perp}(\Delta t)$ part of the correlation function (see Figure 4.22), the data exhibits the same emergence of a plateau by simple application of the one mass fit algorithm, albeit not as cleanly. It should be remarked that also here, as in the previous cases of the $C_{\perp}(\Delta t)$, we were not able to use a tentative estimate for a higher mass to improve the fits.

From that we can draw two conclusions. First, the perception that the data quality of the two correlation functions $C_{\gamma_0}(\Delta t)$ and $C_{\perp}(\Delta t)$ differ, also holds on the large lattice. So there is a systematic effect, which one might want to explore in the future. However, by going to larger lattices, we can circumvent the drawback, since we can simply wait for the correlator to reach a plateau at high t_i . This was not possible on the smaller lattices. The second conclusion is that, since our mass estimate for the $C_{\perp}(\Delta t)$ component is

$$am = 0.40(7) , \quad (4.21)$$

the two components describe the same particle, as their mass estimates are compatible with each other. One could have been inclined to doubt that, based on the results for small lattices. So obviously, the case for going to a larger lattice is strong in the case of the gluino glue particle.

We conclude the analysis of the gluino glue by summarizing our results, where we apply a somewhat draconian filter. We finally only quote masses in table 4.4, for which we were able to extract a lower mass, nevertheless saving the higher masses for the discussion later.

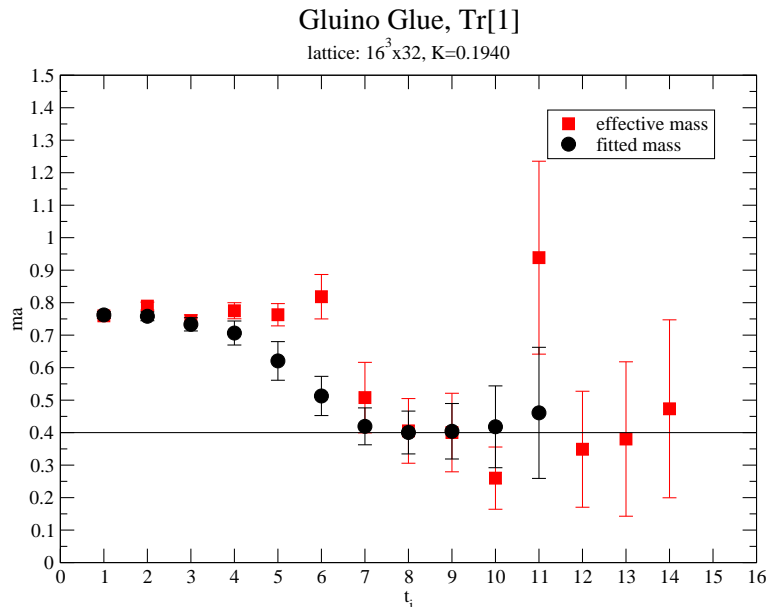


Figure 4.22: effective mass and one mass fit to the $\tilde{g}g$ correlator at $\kappa = 0.1940$.

	$am_{C_{\gamma_0}}(\Delta t)$	$am_{C_{\mathbb{1}}}(\Delta t)$
1925.12c	0.33(4)	
1940.12c	0.49(4)	
1940.16c	0.43(1)	0.40(7)
1955.12c	0.35(4)	

Table 4.4: Summary of results for the lightest masses of the gluino glue bound state.

4.4.3 Adjoint Mesons

The second large block of analysis and certainly the most computational work involved the study of the adjoint mesons $a-\eta'$ and $a-f_0$. The structure of the correlations function is, as reported in Section 3.4.4,

$$C(\Delta t) = C_{2\text{loop}}(\Delta t) - 2C_{1\text{loop}}(\Delta t) . \quad (4.22)$$

The one-loop correlation functions are obtained by inverting Q on randomly chosen point sources, while, as we have discussed at length, for the two-loop correlators we use stochastic estimators.

In comparison with the gluino glue, there is one ensemble missing from this analysis, 1925.12c. On this ensemble, the analysis was already performed in [19]. We will compare those results with our own, as they provide a useful guide. For reference, it was found that

$$am_{a-\eta'} = 0.52(5) \quad \text{and} \quad am_{a-f_0} < 1.0(1) . \quad (4.23)$$

In the following, we will first justify our choice of subsamples from the complete en-

semble by the use of the autocorrelation time. We will then proceed to analyze these subsamples in the same format as for the gluino glue, i.e. in the order 1940.12c, 1955.12c, 1940.16c.

Autocorrelations

Since we opted for SET estimation techniques for the computationally demanding two-loop graph, we need to cut down the number of configurations that are to be evaluated. In Section 4.2.1 we determined the number of necessary estimates to be $N_{est} \approx 150$. Clearly, it is computationally impossible and not even useful to use every available configuration. So we need to find the maximal set of uncorrelated configurations in an ensemble with respect to the quantity we want to estimate. Since we want to estimate the lightest purely fermionic particle, it makes sense to use the smallest eigenvalue of the fermion matrix λ_{min} as a reference. This choice is popular in the literature, as it is an easily accessible primary quantity, for which the measurement of the integrated autocorrelation time is straightforward. By determining a set of decorrelated configurations with respect to the smallest eigenvalue, we ensure keeping the number of configurations that need to be evaluated to a minimum while at the same time we do not waste any physical information. Using the defining equation (3.55) of the integrated autocorrelation time $\tau_{int}(\lambda_{min})$, we perform the analysis on the ensembles listed above.

Ensemble 1940.12c

For this set of configurations, the measured autocorrelation time with respect to λ_{min} is $\tau_{int}(\lambda_{min}) \sim 240$ updates. As a practical matter, therefore, on average only every 12th configuration was used, since each configuration is separated by 20 updates. This fixes the number of configurations to analyze at ~ 320 . As an example of such an estimate we show in Figure 4.23 a typical measurement of the autocorrelation on one of the eight lattices updated in parallel.

For the actual mass determination we first measure the one-loop and two-loop correlation functions separately on each configuration of our subsample. Next, we combine the two configuration-wise to form the physical correlation (4.22). Then we proceed as for the gluino-gluon particle by fitting the correlator to the expected exponential form. Figure 4.24 shows in the same manner the one-mass fits, each with the other's contribution from the state subtracted. As can be clearly seen, the lower mass provides an excellent fit, giving a plateau from $t_i = 2$ up to $t_i = 10$, almost the entire possible range of fit intervals. This leads us to estimate the mass of the $a-\eta'$ for this ensemble

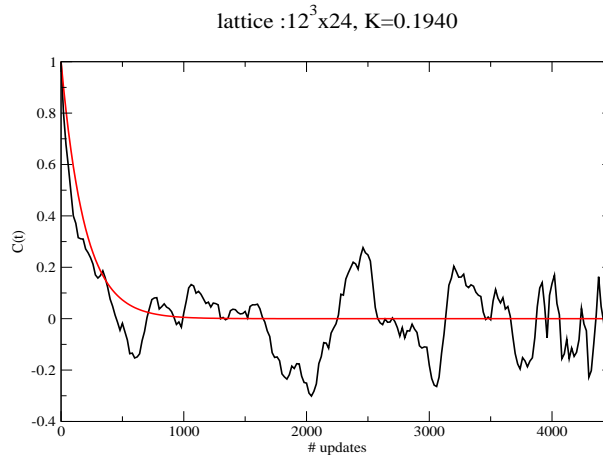


Figure 4.23: Autocorrelation of the minimal eigenvalue on lattice 1 (of a total of 8) run in parallel with an exponential fit.

to be

$$am_{low} = 0.421(9) . \quad (4.24)$$

Unfortunately, the $a-f_0$ is not so friendly. The core of the problem does not lie in the bad quality of the data, but in the fact that its two-loop correlator has a vacuum expectation value, which needs to be subtracted to arrive at a combined correlation function which approaches zero in the $\Delta t \rightarrow \infty$ limit. In other words, the actual correlator sits on a huge numerical mountain that needs to be taken care of. In principle, the information is provided by simply calculating

$$\langle \text{Tr}[Q^{-1}] \rangle^2 \quad (4.25)$$

on the ensemble from the available data and subtracting it from the correlation. However, it turns out that when subtracting the measured constant from the symmetrized scalar correlator, one gets an acceptable correlator except for the fact that it does not go to zero for large Δt , but, for this ensemble, to a value of ~ 5 . The most probable explanation is that through the repeated application of the stochastic estimates, numerical inaccuracies accumulate to produce the offset. To verify this speculation, one would have to repeat the same study, using improved precision, most notably 64bit variables and more advanced summing techniques to ensure accuracy throughout. A second possibility could be that N_{est} for the SET is still too low to suppress the noise sufficiently for this operator. In view of our above analysis of the SET method though, this does not seem to be the case.

In practice, the most obvious solution, to fit to the function (3.78) with $c_0^2 \neq 0$, fails to render stable results. However, if we fit to (3.78) with a manually fixed c_0^2 , i.e. subtracting out a constant from the correlation data, stable fits emerge. The apparent question then becomes, which non-arbitrary subtraction constant one should choose. Here we proceeded by noting two (purely numerical) observations. First, using the

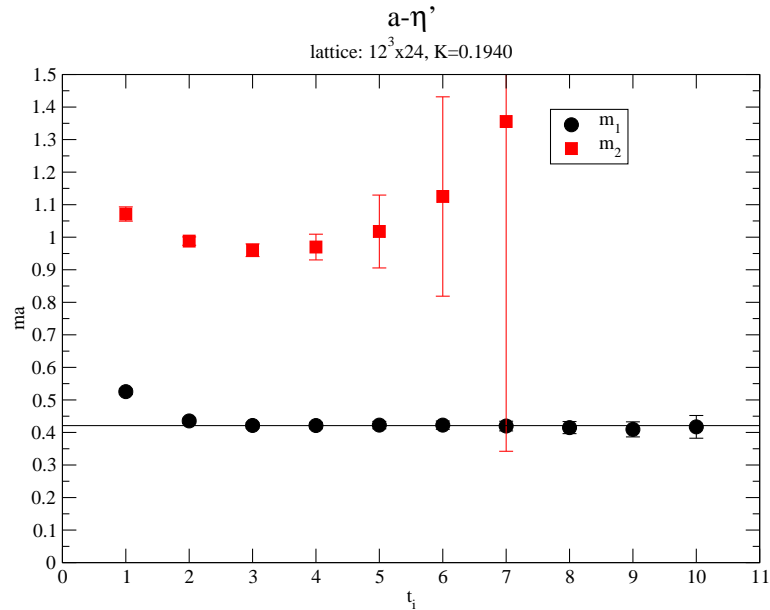


Figure 4.24: One mass fit to the subtracted $a-\eta'$ correlation function on the 1940.12c ensemble.

form of (3.78) as the correlation function, we notice that in the high Δt region for $\Delta t = T/2 = 12$ and $m \sim 0.2$, taking the mass of the $a-\eta'$ as our first guess, the numerical value of the expected correlation ($e^{-m\Delta t} + e^{-m(T-\Delta t)}$) is $\sim \mathcal{O}(0.1)$. Secondly, if we normalize the correlator, such that the correlation is 1 at $\Delta t = 1$, we conclude that all amplitudes for the various states in (3.77) should be less than 1, specifically $0 < c_n^2 < 1 \ \forall n$. This holds in particular for $n = 1$ which is the case we are looking for. Therefore we see that in an ideal world, where all the heavier modes have died off at large Δt , the value of the normalized correlator at $\Delta t = T/2$ and with $ma > 0.2$ would numerically have to be smaller than 0.1. So we can take this number as a reference point and scan the constant space systematically to search for a subtracted correlation that gives a plateau, i.e. where a stable and physically meaningful fit emerges.

This method is not the most elegant solution. From a theoretical point of view, it has the disadvantage of being ambiguous, since it does not lead to a definite result, rather to a collection of possible ones. It does enable us to extract a rough estimate for the $a-f_0$ for this ensemble though, as presented in Figure 4.25. The large error bars reflect the fact that a number of possible candidates give reasonable fits here. This estimate represents the weighted average over these, obtained via (A.19). So finally, as an estimate for the $a-f_0$, we quote

$$am = 0.3(3) . \quad (4.26)$$

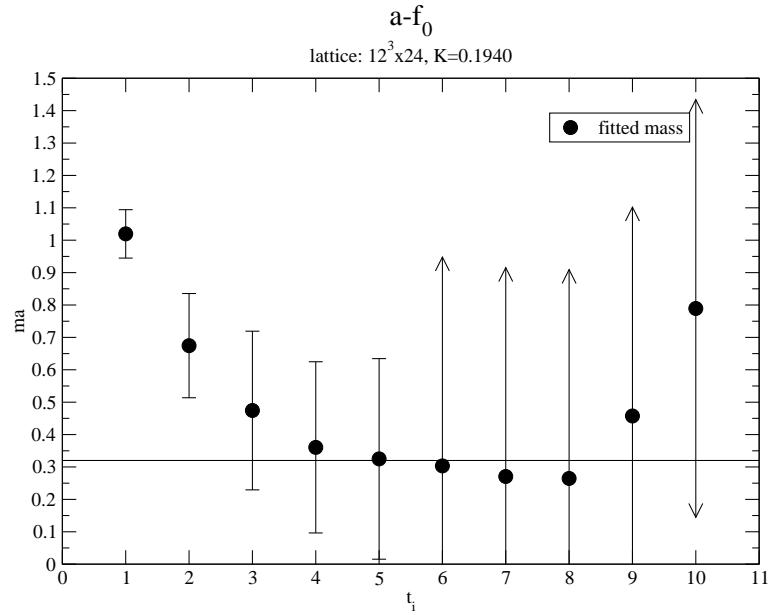


Figure 4.25: Estimate of the $a-f_0$ mass for the 1940.12c ensemble.

Ensemble 1955.12c

On this ensemble the measured autocorrelation time with respect to the smallest eigenvalue is $\tau_{int}(\lambda_{min}) \sim 330$ updates. Therefore, on average, only every 24th configuration of the total ensemble was used, making a total of 224 configurations. Again, we show the corresponding exponential fit in Figure 4.26.

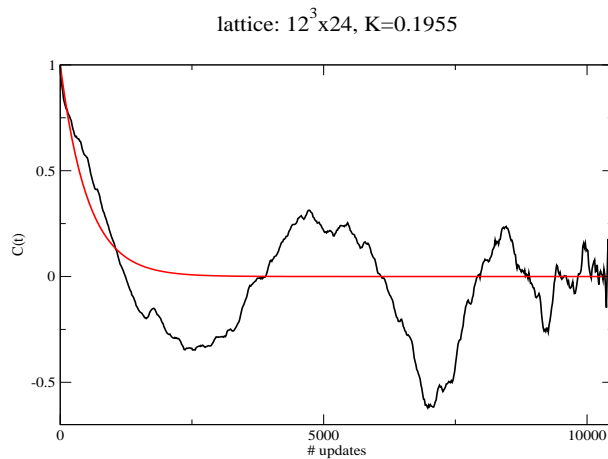


Figure 4.26: Autocorrelation of the minimal eigenvalue on lattice 1 (of 8) run in parallel with an exponential fit.

As in the previous case, we find that the $a-\eta'$ gives a very good signal and therefore produces a fit that is constant over an extremely wide range of fit intervals (see Figure 4.27). The higher mass present in this correlation, which was extracted by the above methods, displays a similar stability over a long range of fit intervals, although

with larger errors. This suggests, that it indeed might be the next higher state in this channel¹. As best estimates on this ensemble, we find

$$am_{low} = 0.24(2) \quad \text{and} \quad am_{high} = 0.81(6) . \quad (4.27)$$

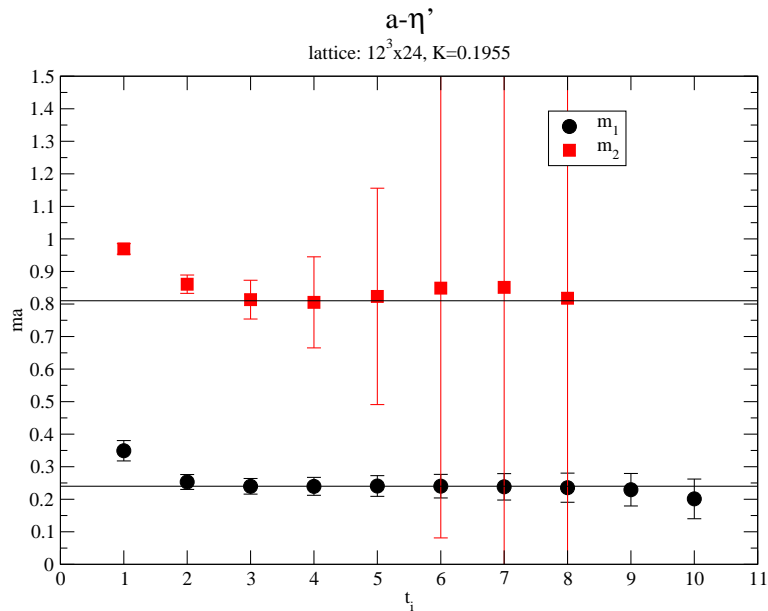


Figure 4.27: One mass fit to the subtracted $a-\eta'$ correlation function on the 1955.12c ensemble.

In the scalar channel we are confronted with somewhat the same problems we saw for the previous ensemble. The correlator, after subtracting the vacuum contribution, is still plagued by an offset. Applying the method described above, we nevertheless find a surprisingly good and unique signal with respect to the subtraction constant (see Figure 4.28). The large errors, especially at larger t_i , underline our observation that this channel is characterized by a low signal/noise ratio.

For the $a-f_0$, we quote as our best estimate on this ensemble

$$am = 0.24(9) . \quad (4.28)$$

Ensemble 1940.16c

Finally, on the large lattice we measured the autocorrelation to be $\tau_{int}(\lambda_{min}) \sim 130$ updates. Since we ran four lattices in parallel with each ~ 6400 updates, we end up choosing every 18th configuration, giving us a subset of a total of 218 configurations

¹This conclusion is not always possible to draw, since we merely single out one higher state with a large amplitude, not necessarily the next highest.

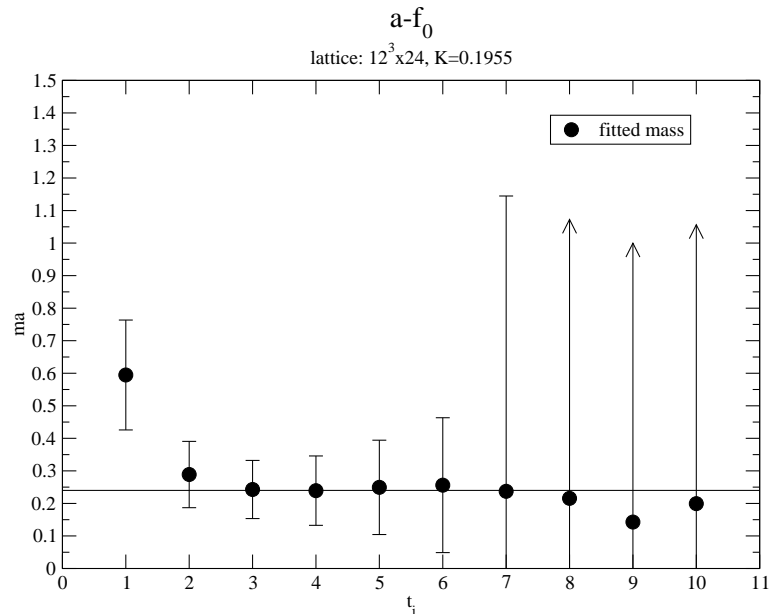


Figure 4.28: Mass estimate for the $a-f_0$ on the 1955.12c ensemble.

On this ensemble, the pseudo-scalar adjoint meson provides us again with an unequivocal signal for a fit. Using the familiar subtraction scheme² we find two masses, of which the lower concerns us the most (see Figure 4.29). It generates a clear plateau starting from $t_i = 4$, continuing within error up to $t_i = 13$. For the higher t_i we see a systematic drop in both masses. We attribute this to statistical effects. Notice also that for $t_i = 12$ the higher mass estimate and the lower coincide, indicating the fading of the higher mass in the sum of exponentials. Therefore our best estimate for the ensemble in this channel is

$$am_{low} = 0.24(1) \quad \text{and} \quad am_{high} = 0.65(2) . \quad (4.29)$$

During the course of our error analysis of the volume source method, this ensemble was the basis of our study. Therefore we take the opportunity to compare the result above with the one obtained by estimating the two-loop graph by $15 \times N_{spin} \times N_{adj.color} = 90$ VST inversions of the fermion matrix, using the *correct* version, as defined above. As can be seen from Figure 4.30, this gives a comparable estimate, somewhat larger than the SET version,

$$am_{low}^{VST} = 0.29(5) \quad (4.30)$$

with a larger error. We therefore conclude that one would need to increase N_{est}^{VST} to lower the error bar and possibly approach the estimate obtained by the stochastic method. As a side note let us compare the costs of the two estimates. The SET

²The determination of the effective masses for the $a-\eta'$ on this ensemble gives a clear indication for the presence of higher states. The corresponding plot, Figure 4.46, is to be found in the finite volume analysis.

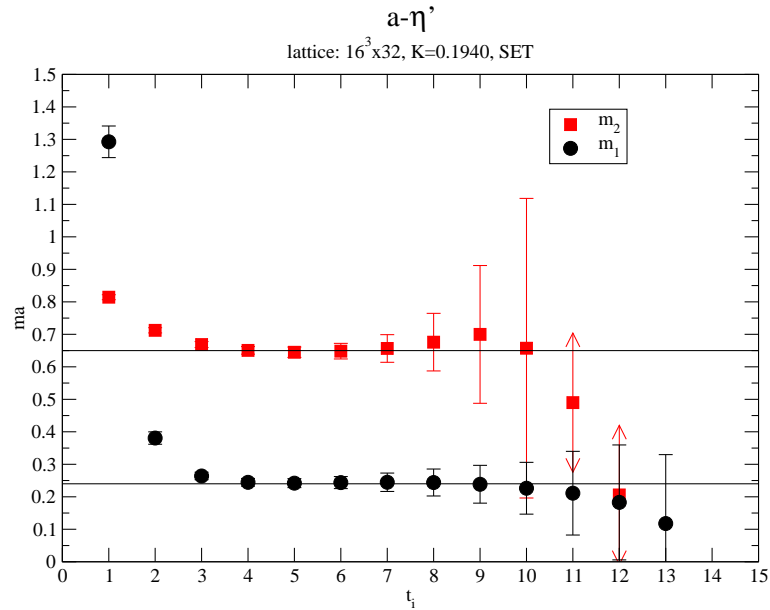


Figure 4.29: One mass fit to the subtracted $a\text{-}\eta'$ correlation function on the 1940.16c ensemble.

value (4.29) was computed, as described above, by 150 stochastic estimates and therefore 300 inversions in total (using the spin explicit method) per configuration. In computational cost, it was therefore roughly three times as expensive as the VST estimate.

We finally turn to the scalar channel. On the larger lattice it was not possible to extract any meaningful estimate for the lowest mass, due to the problems described above. Even subtracting the constant “by hand” did not produce a reliable signal. We see the main problem, insufficient numerical accuracy, as the most probable reason. In addition to the problems outlined for the previous ensembles, on the larger lattice we simply have larger global sums, which amplify the problem. We nevertheless attempt to extract an upper limit on the lowest mass of the $a\text{-}f_0$. Since we experienced the signal to be washed rather fast for larger time separations, we fixed t_i here instead and varied the other side of the fit interval, t_f , thus fitting to the higher states still present at low time separations. The results are presented in Figure 4.31 as a function of t_f . Thus, we simply get an upper bound on the lowest mass, which in this case amounts to

$$am < 0.78 . \quad (4.31)$$

Concluding this section, we present a summary of the reliable estimates for the lowest mass on the a-mesons in Table 4.5.

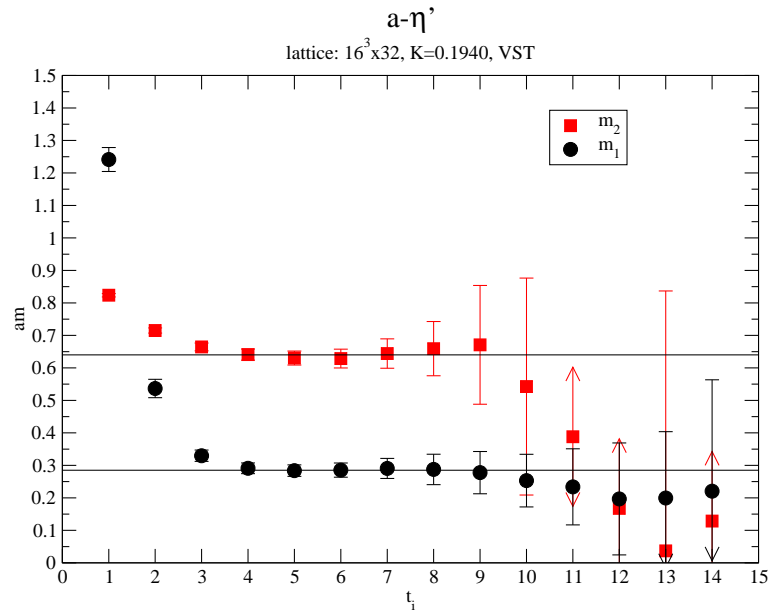


Figure 4.30: One mass fit to the subtracted $a-\eta'$ correlation function on the 1940.16c ensemble using the volume source technique correctly.

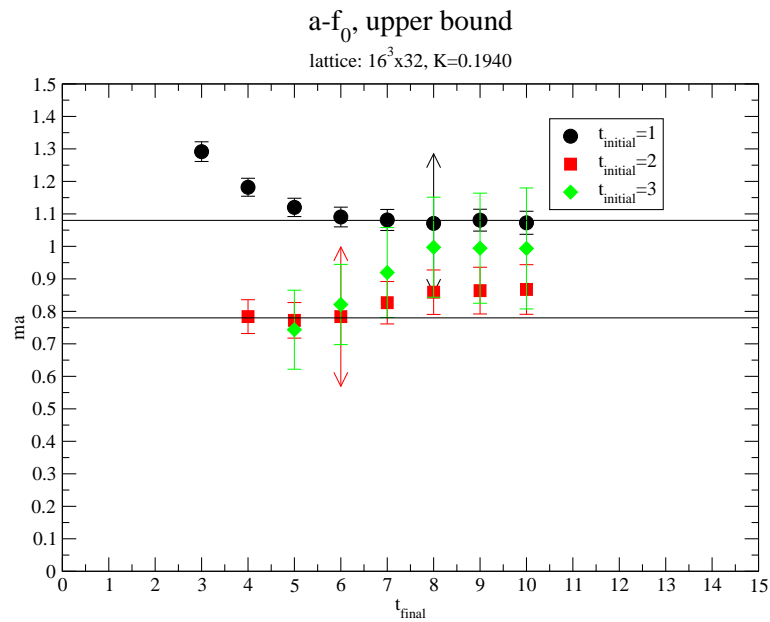


Figure 4.31: Upper bound for the lowest mass of the $a-f_0$ on the 1940.16c ensemble.

	$am_{a-\eta'}$	am_{a-f_0}
1925.12c	0.52(5)	
1940.12c	0.421(9)	
1940.16c	0.24(1)	
1955.12c	0.24(2)	0.24(9)

Table 4.5: Summary of results for the lightest masses of the adjoint mesons $a-\eta'$ and $a-f_0$, where the 1925.12c value was taken from [19].

4.4.4 Glueballs

Although the glueballs are a well known object in lattice gauge theory investigations, they belong to the most notorious particles to measure. This stems from the fact that their purely gluonic correlations are plagued by a relatively low signal/noise ratio. The operators for the $J^{PC} = 0^{++}, 0^{-+}$ glueballs were introduced in Section 3.4.2 in equations (3.91) and (3.92).

To increase the overlap of the operators with the respective lightest state and to improve the signal, we used APE smearing extensively, as described in the appendix, with parameters as quoted. We will proceed as in the previous sections, going from heavier to lighter gluino mass and from smaller lattices to the larger one.

Ensemble 1925.12c

We will confine ourselves again to the glueball states that have not been determined yet. As such we quote for reference the scalar glueball mass from [19] on the 1925.12c ensemble as

$$am_{0^{++}} = 0.53(10) , \quad (4.32)$$

which was obtained with smearing parameters $(\epsilon_{APE}, N_{APE}) = (0.285, 20)$.

The noisiness of the data is exemplified by the fact that in all cases during this study, it was not possible to obtain reliable mass fits for the glueballs, in contrast to the previous particles. This comes as a consequence that at high temporal separation Δt the signal is all but washed out. The traditional fitting routines, however, try to incorporate this signal too and thus are rendered unstable. Systematically lowering the higher end of the fit interval t_{final} has no perceivable effect either, so we rely on effective mass analyses for this section.

The pseudo-scalar glueball is more elusive than the scalar. On the 1925.12c ensemble it was not possible to optimize our smearing procedure such that one obtains a signal beyond timeslice $t = 3$. The local masses shown in Figure 4.32 were calculated, accord-

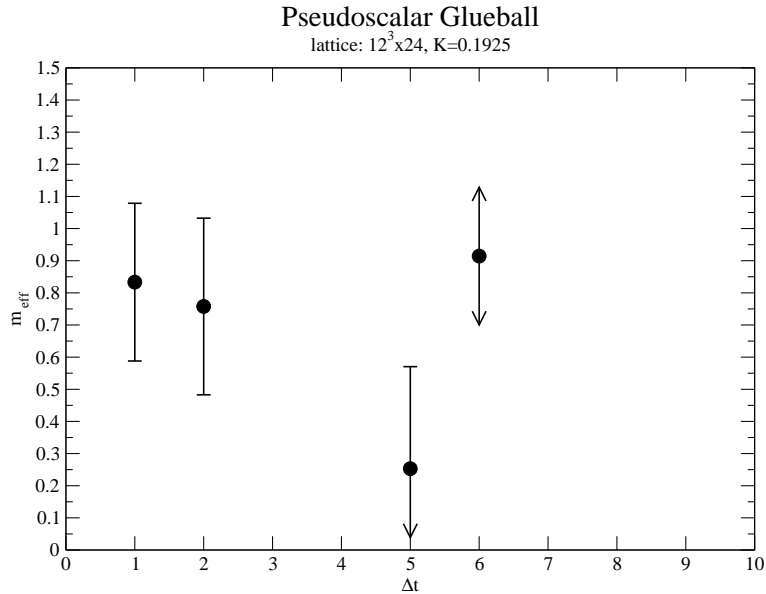


Figure 4.32: Effective masses of the 0^{-+} glueball for the 1925.12c ensemble.

ing to the formulae (3.80)-(3.83). For the final estimate we use $m(t_1, t_2, T) = m(1, 2, T)$ and $m(2, 3, T)$ after APE smearing with parameters $(\epsilon_{APE}, N_{APE}) = (0.285, 36)$. We discard the data at higher t as noise. Therefore, the estimated value of the mass should be interpreted with care since, as indicated in the previous Sections 4.4.2 and 4.4.3, at low time separations, the correlator possibly contains contamination of higher states in spite of smearing, which aims to reduce their influence. With this in mind, we find as the best estimate for the pseudo-scalar glueball on this ensemble

$$am_{0^{-+}} = 0.8(2) . \quad (4.33)$$

The true value of this state is likely to be somewhat below the estimated.

Ensemble 1940.12c

Here, for the pseudo-scalar glueball, we have a similar situation (see Figure 4.33). At higher t , it was not possible to extract a signal and again, the data points on the far end should be viewed as noise. The smearing parameters for this operator, as for the scalar glueballs, are $(\epsilon_{APE}, N_{APE}) = (0.285, 40)$, leading us to a tentative estimate for the pseudo-scalar of

$$am_{0^{-+}} = 1.1(3) , \quad (4.34)$$

with the same caveats as above.

The scalar glueball is more friendly with respect to its signal/noise ratio. As we pointed out in Section 3.4.2, we have the opportunity to cross check the correlator obtained by simple spatial plaquettes, labeled $v1$, with the parity even version of the operator

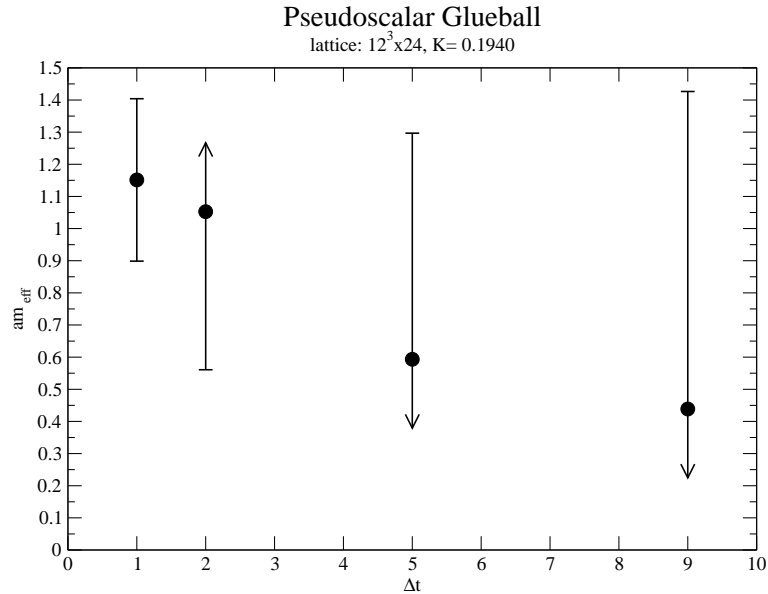


Figure 4.33: Effective masses for the 0^{-+} glueball obtained for the 1940.12c ensemble.

that was used for the 0^{-+} , labeled $v2$. The corresponding plots are shown in Figures 4.34 and 4.35. We see that they show almost exactly the same results, emphasizing the correctness of the interpretation of the operators. In fact, in both figures we see a signal up to timeslice $t = 5$, encoded in the effective mass $m(4, 5, T)$. We also observe a drop of approximately 10% in the mass values, leading us to the conclusion that we still have, albeit marginal, higher state contributions in the correlation function. Nevertheless, based on the better quality of the data, we can give a more sound estimation of the lowest mass for the scalar glueball, namely

$$am_{0^{++}} = 0.4(1) . \quad (4.35)$$

Ensemble 1955.12c

The scalar glueball on this ensemble presents us with a signal comparable to that of the previous. Smearing was found to be optimal when performed with the parameters $(\epsilon_{APE}, N_{APE}) = (0.285, 24)$. The resulting effective mass calculations, Figure 4.36 and 4.37, show a plateau almost from the beginning, within error. Note, however, that this is also due to the large error bars. In particular, the higher effective mass point at time distance $\Delta t = 4$ we interpret as a statistical outlier, similarly the data points for $\Delta t > 5$. We determine our estimate by the weighted average (A.19) of data points $\Delta t = 2, 3, 4, 5$ to be

$$am_{0^{++}} = 0.36(4) . \quad (4.36)$$

Using the second version of the operator gives the same estimate, although with a slightly larger error.

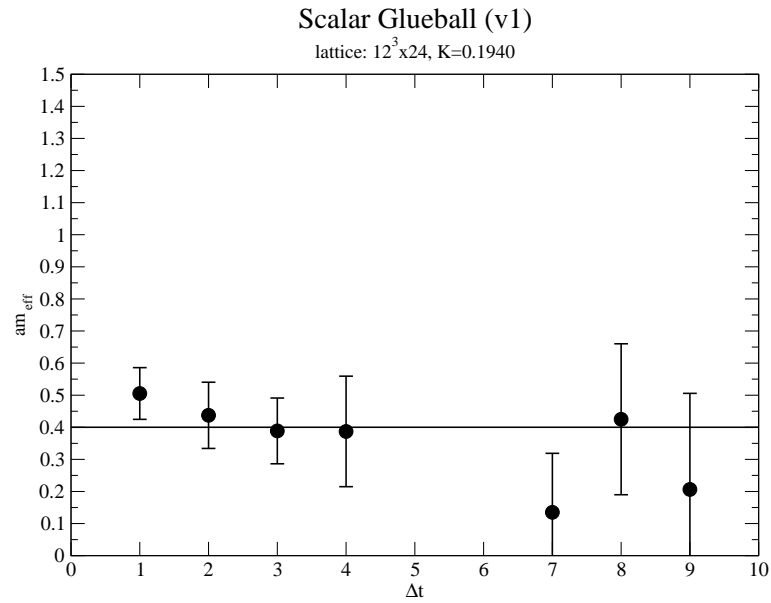


Figure 4.34: Effective masses for the 0^{++} glueball on the 1940.12c ensemble, using the sum of spatial plaquettes as the operator (v1).

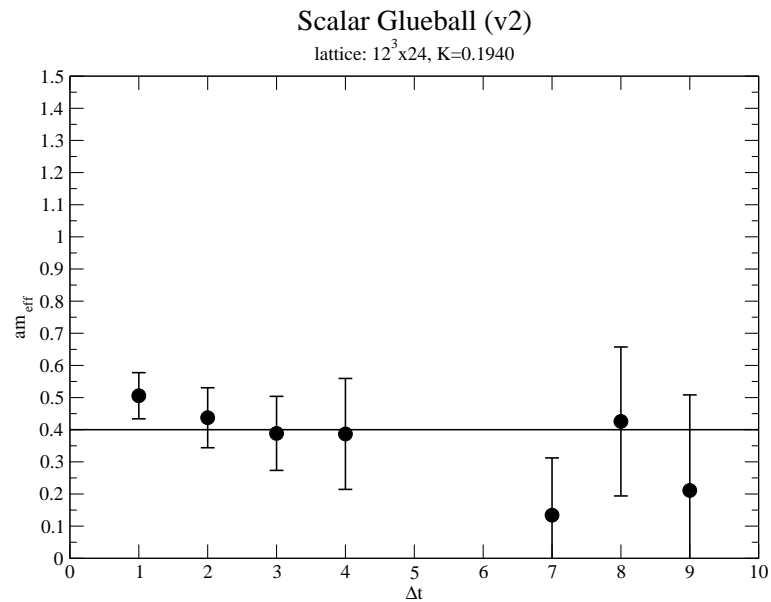


Figure 4.35: Effective masses for the 0^{++} glueball on the 1940.12c ensemble, using the parity even part of the 0^{-+} glueball operator (v2).

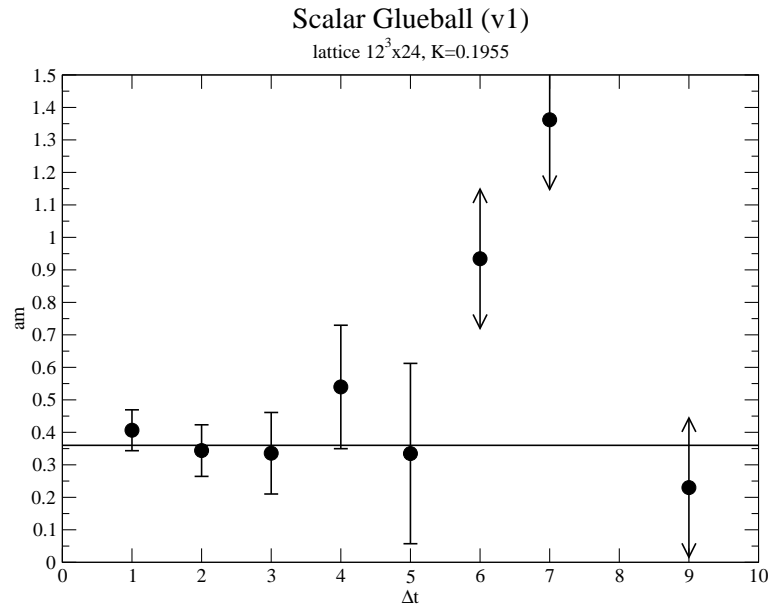


Figure 4.36: Effective masses for the 0^{++} glueball on the 1955.12c ensemble, using the sum of spatial plaquettes as the operator (v1).

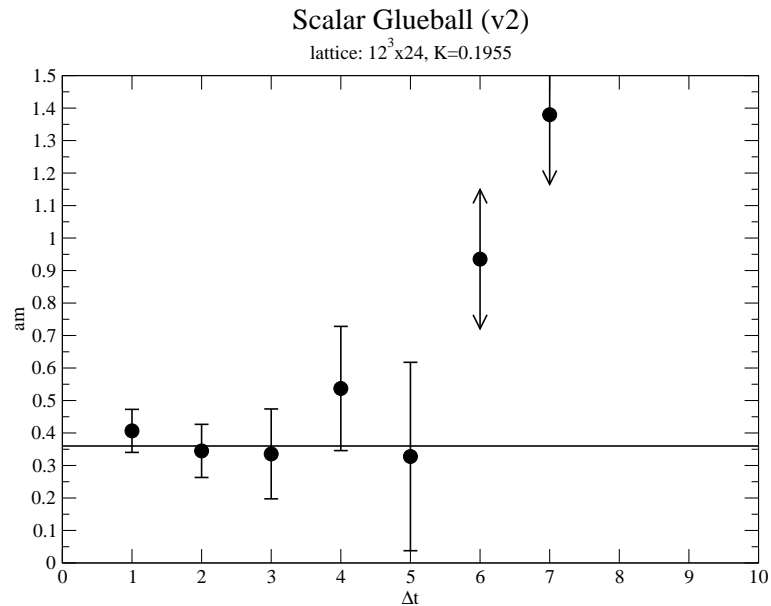


Figure 4.37: Effective masses for the 0^{++} glueball on the 1955.12c ensemble, using the parity even part of the 0^{-+} glueball operator (v2).

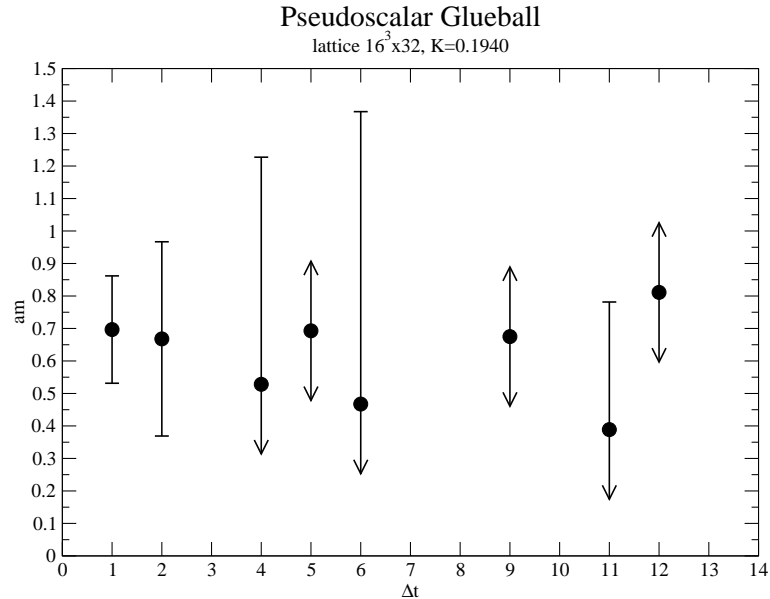


Figure 4.38: Effective masses for the 0^{-+} glueball obtained for the 1940.16c ensemble.

Unfortunately, we were not able to determine a reasonable mass estimate for the pseudo-scalar glueball on this ensemble. This is due to reasons laid out above, namely a remarkably low signal/noise ratio. We will comment on viable methods on how to approach this problem in Chapter 5.

Ensemble 1940.16c

For the pseudo-scalar glueball we are faced again with very low signal/noise ratio. Figure 4.38 shows a typical plot of attempts to determine a mass from the correlation function. The large noise is especially visible in the size of the error bars and that for $\Delta t = 3$, the numerical instabilities were too large to obtain an effective mass. The smearing parameters used in this case were $(\epsilon_{APE}, N_{APE}) = (0.1, 48)$. To estimate the mass, we include points from $\Delta t = 1, 2$, while discarding the higher points as unreliable. We then get

$$am_{0^{-+}} = 0.69(14) , \quad (4.37)$$

where again, this value should be treated with the appropriate caution. We once more suspect the true value to be somewhat below the estimated.

In contrast to the other ensembles, here the scalar glueball proves to be hardest to pin down because of the large fluctuations in the correlator. This outcome is somewhat surprising, since we find no argument for an increase in noise with larger lattice sizes. Since we were unable to extract a viable effective mass calculation beyond time separation $\Delta t = 3$, we estimate an upper bound to its mass in the following way. In Figure 4.39 we plot the dependence of the mass from $\Delta t = 2$, i.e. $m(1, 2, T)$, as a func-

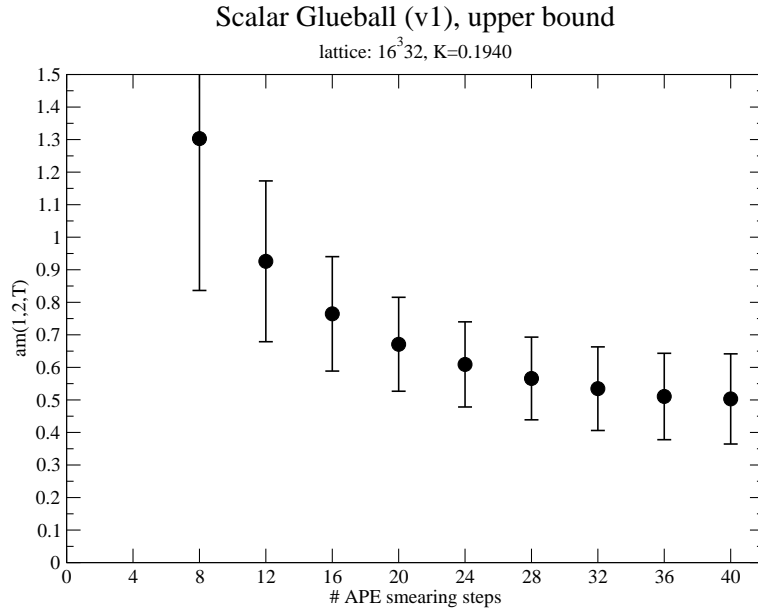


Figure 4.39: Effective masses $m(1, 2, T)$ for the 0^{++} as a function of smearing steps with $\epsilon_{APE} = 0.5$ on the 1940.16c ensemble.

tion of smearing steps at $\epsilon_{APE} = 0.5$. We see that, as N_{APE} grows larger, a plateau within error emerges. Smearing seeks to enhance the overlap of a given operator with the lightest state. If we observe a plateau after a number of smearing steps, it indicates that we have the lowest possible mass estimate at a given time separation, in this case $m(1, 2, T)$. Ideally, this is already the mass of interest, in our case the lowest in this channel. However, since we can not be completely sure that the effective masses at low time separations are free of higher states, or conversely that – if the data were good enough – the effective mass estimates would not drop at higher Δt to a lower plateau, this method can only serve as an upper bound to the lowest mass. In this spirit, we estimate the mass of the scalar glueball on this ensemble to be

$$am_{0^{++}} < 0.52(1) . \quad (4.38)$$

4.5 Ward Identities

We turn to the numerical determination of the ratios of the renormalization factors $am_S Z_S^{-1}$ and $Z_T Z_S^{-1}$, as defined in equations (3.150) and (3.151), through the supersymmetric Ward identities. These are obtained by solving the system of equations (3.161) for the insertion operator $\chi^{sp}(y)$. For our study, we will follow [19, 20] rather closely, where the analogous analysis was carried out on all the 12c lattices. We therefore use the 1940.16c ensemble in this section exclusively.

Since the experience by the collaboration is that the above point-like insertion operators

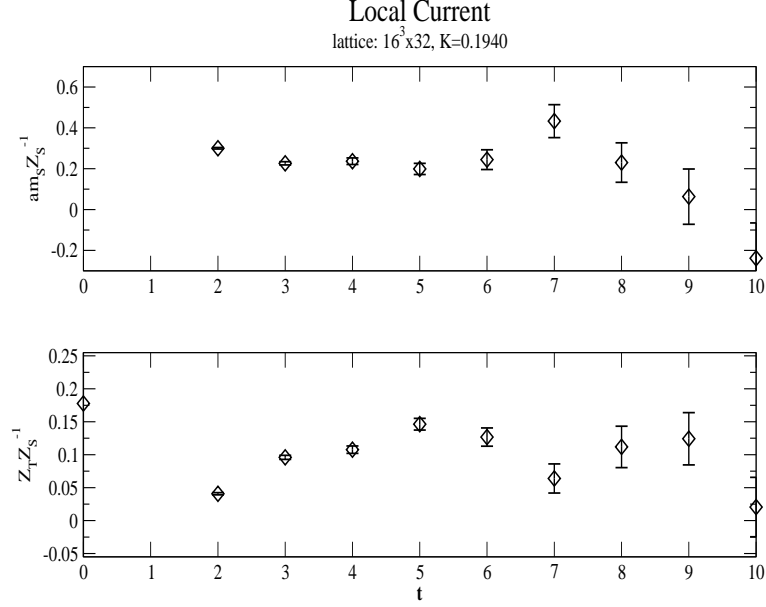


Figure 4.40: Renormalization factors $am_S Z_S^{-1}$ and $Z_T Z_S^{-1}$ for the insertion operator $\chi^{sp}(y)$ and the ensemble 1940.16c .

usually give a noisy signal, we used APE and Jacobi smearing concurrently on the gluon and gluinos. We find the optimal parameters to be the same as for the gluino-gluon, namely

$$N_{APE} = 9, \quad \epsilon_{APE} = 0.5 \quad \text{and} \quad N_{Jacobi} = 18, \quad \kappa_{Jacobi} = 0.2 . \quad (4.39)$$

As a further practical matter, we choose the point of insertion y for $\chi^{sp}(y)$ randomly on each configuration in order to decorrelate subsequent measurements. This approach is supported by the subsequent Jackknife error analysis, which hardly lets the error increase ($\mathcal{O}(0.5\%)$) if we move to larger block sizes, indicating mostly decorrelated measurements.

For the linear fit, we rewrite the equations (3.161) in compact notation as

$$x_i + ay_i = bz_i , \quad (4.40)$$

where a and b denote the ratios of renormalization factors $Z_T Z_S^{-1}$ and $am_S Z_S^{-1}$ and

$$x = \sum_{\vec{x}} \langle \nabla_0 S_0(x) \chi^{sp}(y) \rangle , \quad (4.41)$$

$$y = \sum_{\vec{x}} \langle \nabla_0 T_0(x) \chi^{sp}(y) \rangle , \quad (4.42)$$

$$z = \sum_{\vec{x}} \langle \chi(x) \chi^{sp}(y) \rangle . \quad (4.43)$$

For each time separation Δt the Ward identities are fulfilled independently, so we have as solutions

$$a = \frac{x_2 z_1 - x_1 z_2}{y_1 z_2 + y_2 z_1} \quad b = \frac{x_1 y_2 - x_2 y_1}{y_1 z_2 + y_2 z_1} . \quad (4.44)$$

with $i \in \{1, 2\}$ denoting the two different projections $\text{Tr}[\gamma_0, \mathbb{1}]$ performed in equations (4.41)-(4.43). In Figure 4.40 we show the resulting ratios of the renormalization factors as a function of their time separation t from y . We see that for low t , the correlation still contains contact terms, which loose their influence for $t \gtrsim 3$, resulting in a behavior consistent with a plateau. The signal is, however, washed out for large time separations. The onset of a plateau enables us to make a simultaneous linear fit for the system of equations (3.161) over all time separations, rather than at every time separation independently as was done in Figure 4.40. This results in an overdetermined system of equations.

Using the above notation, we want to minimize the corresponding $\chi^2 = \sum_k (x_k + ay_k - bz_k)^2$ with respect to the parameters a and b , where k now runs over the two traces and over time separations Δt , starting at t_{min} . We find as solutions

$$a = \frac{(y, x)(z, z) - (y, z)(x, z)}{(y, z)^2 - (y, y)(z, z)} \quad b = \frac{(y, x)(y, z) - (y, y)(x, z)}{(y, z)^2 - (y, y)(z, z)} \quad (4.45)$$

with $(x, y) = \sum_k x_k y_k$. Note that these reduce to the solution 4.44 for $k \in \{1, 2\}$. Thus we fit from $t_{min} \geq 3$ up to the maximum extent of the symmetrized correlation functions, $t = T/2$. The resulting values are collected in table 4.6, showing a relatively small dependence on the chosen t_{min} , supporting our view that indeed contact terms do not play a big role for $t \gtrsim 3$.

	$t_{min} =$	3	4	5
$Z_T Z_S^{-1}$		0.226(7)	0.23(1)	0.22(2)
$am_S Z_S^{-1}$		0.100(2)	0.115(4)	0.137(7)

Table 4.6: Dependence of $am_S Z_S^{-1}$ and $Z_T Z_S^{-1}$ on t_{min} on the ensemble 1940.16c.

Thus we find from the above data as our best estimates for the two ratios of renormalization factors

$$Z_T Z_S^{-1} = 0.226(7) \quad \text{and} \quad am_S Z_S^{-1} = 0.100(2) . \quad (4.46)$$

If we compare the values from [20] for the same operator and κ to ours, as listed in Table 4.7, we find agreement, up to approximately 10% for $Z_T Z_S^{-1}$ and 5% for $am_S Z_S^{-1}$. We would have been surprised to see substantial deviation simply stemming from the increase in lattice size, since the Ward identity as such holds for any lattice volume. For smaller lattices, $\mathcal{O}(a)$ discretization effects play a larger systematic role. In consequence, we attribute the discrepancy between the two results to this effect and the large statistical fluctuations at higher time separations. It is still an open question though, how the second possible insertion operator compares to the smaller lattice. An investigation of these issues can be used to study discretization effects as was carried out in [20]. It was not pursued here, however, as it was not the focus of our study.

		$t_{min} =$	3	4	5
$Z_T Z_S^{-1}$	12^3		0.202(15)	0.176(33)	0.186(6)
	16^3		0.226(7)	0.23(1)	0.22(2)
$am_S Z_S^{-1}$	12^3		0.124(6)	0.126(12)	0.142(24)
	16^3		0.100(2)	0.115(4)	0.137(7)

Table 4.7: Comparison of $am_S Z_S^{-1}$ and $Z_T Z_S^{-1}$ for the 1940.12c [20] and 1940.16c ensemble.

We conclude that our present findings do not change the scenario found in [20], namely that the renormalization of the operators is relatively small and that within our numerical accuracy the Ward identity as defined in (3.155) indeed holds.

4.6 The Massless Gluino Limit

As we discussed in the previous chapters, the massive gluino we encounter in our simulations breaks supersymmetric and chiral invariance softly. We have argued that to alleviate these effects and in particular to reach the region where the effects are linear in $m_{\tilde{g}}$, it is necessary to tune the bare gluino mass as the input parameter of the simulation, essentially κ , close to a value κ_c where the renormalized gluino mass vanishes. Conversely, a good estimate of κ_c provides a sound measure of proximity to the massless gluino limit. In Section 3.7 we presented two methods that can be used to arrive at such estimates. We will apply them here with the available data that was extracted in the previous sections of this chapter. As an addendum to the OZI picture borrowed from QCD, we also discuss the relative size of contributions of the partial correlation functions to the total $a-\eta'$ correlation function.

4.6.1 Critical Hopping Parameter from Ward Identities

The subtracted gluino mass m_S defined through the Ward identities in equation (3.150) is, by its definition, expected to vanish linearly if κ approaches its critical value. Supplementing our data with that from [20], we plot the dependence of the ratio $am_S Z_S^{-1}$ on $1/\kappa$ in Figure 4.41. We observe a dependence on $1/\kappa$ which is compatible with a linear decrease. Using the data for a linear regression fit, one can estimate the value of κ_c by extrapolating to $am_S Z_S^{-1} \rightarrow 0$. The result we obtain by this method is

$$\kappa_c = 0.19693(17) \quad (4.47)$$

with a surprisingly small error. Comparing the value to our previous estimate, i.e. the same data with the result from the large lattice excluded, one arrives at $\kappa_c =$

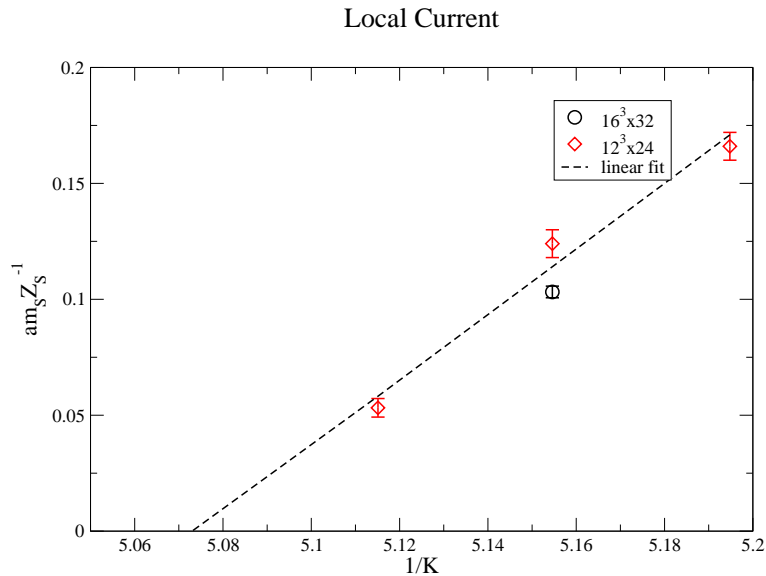


Figure 4.41: Dependence of $am_S Z_S^{-1}$ on κ^{-1} combined with results from [20], fitted linearly.

κ	0.1925	0.1940	0.1955
$am_{\tilde{g}}$	0.0593(64)	0.0392(64)	0.0195(64)

Table 4.8: $am_{\tilde{g}}$ obtained by (4.48) for $\kappa_c = 0.19693(17)$.

0.19750(38) [20]. It is interesting to note that although the results are compatible at the one standard deviation level, we get a slightly smaller value. It is naturally of considerable interest how this result varies, once the corresponding data from the larger lattice at $\kappa = 0.1955$ is available, where we expect to get sound estimates nearer to κ_c .

Turning the argumentation around, we can use the above value of κ_c to give an estimate of the subtracted gluino mass $am_{\tilde{g}}$ by plugging κ_c into the formula (3.162), assuming one is in its region of validity:

$$am_{\tilde{g}} = \frac{1}{2} \left(\frac{1}{\kappa} - \frac{1}{\kappa_c} \right). \quad (4.48)$$

Note that this definition is equivalent to that of the “bare quark mass” in QCD. The resulting values are collected in Table 4.8 for the various hopping parameters used in this study. Judging $m_{\tilde{g}}$ from QCD units, we would arrive for $\kappa = 0.194$ at an approximate value of $m_{\tilde{g}} \approx 125 \text{ MeV}$ using $am_{\tilde{g}} = 0.0392$ and $a \approx 3.15 \text{ GeV}$ from Section 4.3, which is of the order of the strange quark mass. For QCD calculations, such a value for the quark mass is considered to be far from the chiral limit. This suggests that from the point of view of the Ward identities, we are not yet very near to κ_c . We do, however, definitely see the linear behavior of $am_S Z_S^{-1}$ with respect to the inverse hopping parameter in Figure 4.41. This indicates that here the $\mathcal{O}(am_{\tilde{g}})$ effects are small.

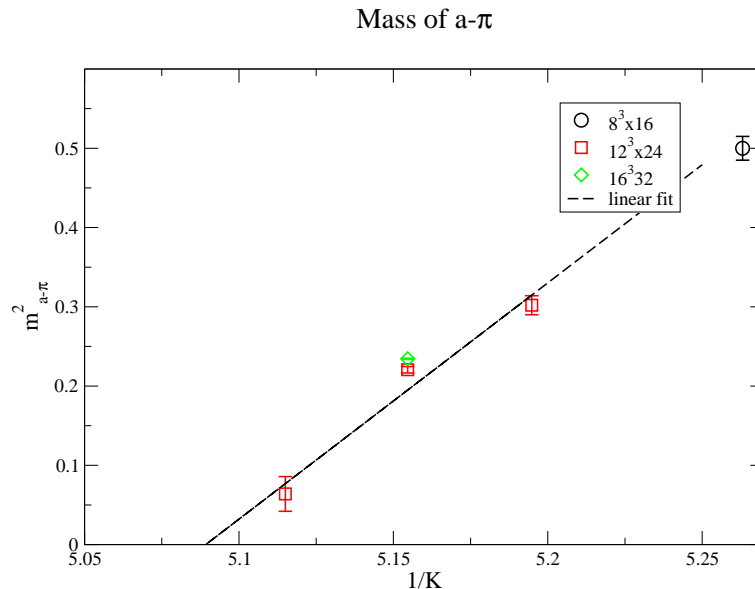


Figure 4.42: Squared Mass of OZI $a-\pi$ mode on κ^{-1} combined with a result from [19] as a function of κ^{-1} .

4.6.2 Critical Hopping Parameter from OZI Arguments

As described in Section 3.7, the second method used to estimate κ_c comes from OZI arguments in the quenched approximation made by G. Veneziano and S. Yankielowicz in [9]. The analogy to QCD is drawn, where firstly the pion becomes massless in the chiral limit, with $m_\pi^2 \propto m_q$, and therefore secondly, the η' correlation function should be purely governed by the two-loop correlator. Since the $N = 1$ SYM model behaves in many respects similarly to QCD, one can try to carry over these arguments.

To test the hypothesis, we plot the squared mass of what we call the $a-\pi$, i.e. the mass induced by the connected correlator

$$C(\Delta t) = \sum_{\vec{x}} \langle \text{Tr}[\gamma_5 Q_{x,y}^{-1} \gamma_5 Q_{y,x}^{-1}] \rangle \quad (4.49)$$

in equation (3.102), remembering the “unphysicalness” of the “state”, as a function of κ^{-1} in Figure 4.42. Indeed it shows the expected linear behavior. If we perform a fit and extrapolate to $am_{a-\pi}^2 \rightarrow 0$, we find as an estimate for the critical hopping parameter

$$\kappa_c^{(a-\pi)} = 0.1977(2) , \quad (4.50)$$

which disagrees slightly with the value of κ_c obtained from the Ward identities. However, it should be stressed that both values are compatible within error to that obtained in [20]. Since the deviation is only small, $\mathcal{O}(0.1\%)$, it would certainly be too soon to declare the failure of the QCD analogy.

On the other hand, the analogous behavior is reaffirmed impressively, if we compare

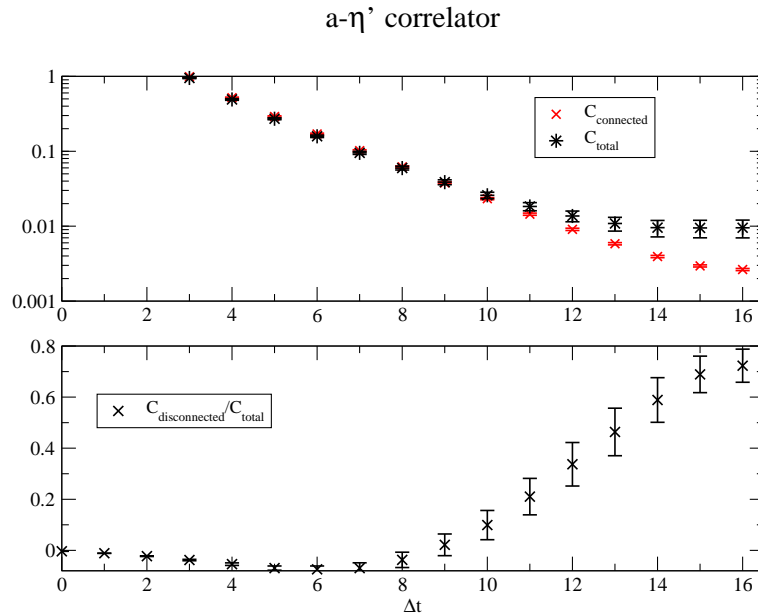


Figure 4.43: Comparison of the constituent correlations in the $a\text{-}\eta'$ propagator.

the relative contributions of the connected and the disconnected correlator to the $a\text{-}\eta'$ propagator (see Figure 4.43). In QCD, the structure of the η' correlation function is very similar. There, the one-loop piece is the pion. As we saw above, in the chiral limit, the pion becomes the massless Goldstone boson, while the η' retains its mass. Thus, the two-loop contribution has to be completely generated from the mass, which in QCD is attributed to the chiral anomaly. Again, it is not clear if we should see similar behavior in the case of $N = 1$ SYM theory, although we know from effective field theory (cf. Chapter 2) that in the supersymmetric limit the $a\text{-}\eta'$ remains massive. From Figure 4.43 we see that at high time separations, the correlator is dominated by the disconnected piece up to approximately 70% of the total (lower panel). This figure compares nicely with determinations of that ratio extracted from lattice QCD calculations [48]. There, one finds very similar relative contributions. Again, it would be most interesting to see the comparison with the corresponding data at $\kappa = 0.1955$ on the large lattice in order to test the hypothesis that the value of the ratio should grow for lighter gluino masses in accordance with the above analogy.

4.7 Finite Volume Effects

As we have two ensembles that have the same simulation parameters, except for their respective simulated lattice volume, we take the opportunity to search for systematical finite volume errors in the spectrum results, where possible.

Gluino Glue

Beginning with the Gluino Glue particle, we compare the bare correlators of the statistically better determined $C_{\gamma_0}(\Delta t)$ in Figure 4.44 for the 1940.12c and the 1940.16c ensembles on a logarithmic scale. For a clean correlation function of one particle, one expects a linearly falling function up to where the reflected correlator gains influence at $\Delta t \approx T/2$. We see that for the lower Δt this is the case for both correlators, although with the caveat that the smaller lattice exhibits a larger fall off, indicating a larger mass. This behavior is to some degree expected, since the smaller lattice “squeezes” a light state into a box, giving it more energy and a larger mass. The difference between the true mass of a particle in the infinite volume $M(\infty)$, and the mass of the particle $M(L)$, simulated on a lattice of size $L^3 \times T$, was calculated in [49]. Its functional dependence can be expressed as

$$\Delta M(L) = M(L) - M(\infty) \propto L^{-p} e^{-cmL} > 0 \quad (4.51)$$

where m is the mass of the lightest meson in the theory and the constants p and c , both of $\mathcal{O}(1)$, depend on the particle under consideration. The main feature to note here is the exponential fall off of the difference when going to larger lattice sizes.

If we now compare the respective mass determinations

$$am_{16^3} = 0.43(1) \quad \text{vs.} \quad am_{12^3} = 0.49(4) \quad (4.52)$$

we see a deviation which can be attributed to that effect, rendering the same particle on the large lattice approximately 10% lighter. The second striking feature is the much earlier onset of the influence of the reflected correlator. This is not a finite volume effect *per se*, but nevertheless gives us less points to fit the mass to. From the discussion in Section 4.4.2 we also saw that for the effective mass to be able to reach a plateau, with the current simulation parameters, a temporal extent of 32 is needed for a secure identification of the particle. In conclusion, we see in the case of the gluino glue quantitatively an effect of approximately 10% in the determined mass. Qualitatively, as was argued above, one needs larger lattices to obtain cleaner results for the unambiguous identification of particles (cf. discussion on $C_{\mathbb{1}}(\Delta t)$ vs. $C_{\gamma_0}(\Delta t)$ and particle identification in Section 4.4.2). This issue becomes particularly evident if we compare the effective mass determinations under the premise that they have the least dependence on other external fitting parameters, see Figure 4.45. Here we observe a somewhat clean signal emerge on the large lattice, while for the smaller no firm statement based on the effective mass can be made.

Adjoint Mesons

Looking at mesonic quantities, we focus on the $a-\eta'$, since here we obtained the most reliable results. We again choose to compare the effective masses in Figure 4.46. We

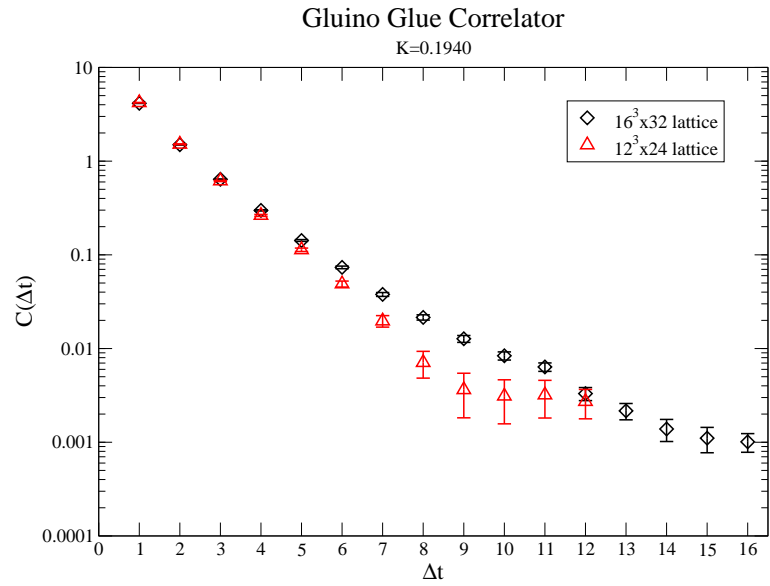


Figure 4.44: Comparison of the gluino glue correlator $C_{\gamma_0}(\Delta t)$ on the large and small lattices for $\kappa = 0.194$.

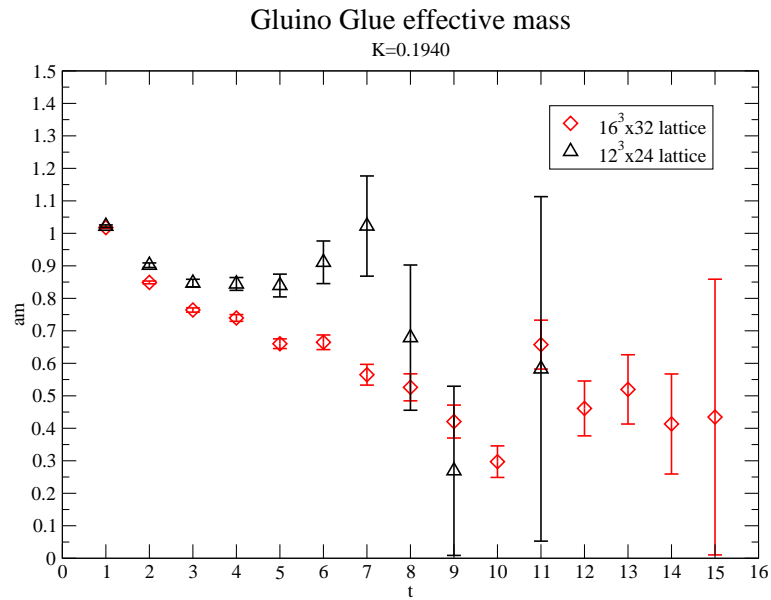


Figure 4.45: Comparison of the gluino glue effective mass of $C_{\gamma_0}(\Delta t)$ on the large and small lattices for $\kappa = 0.194$.

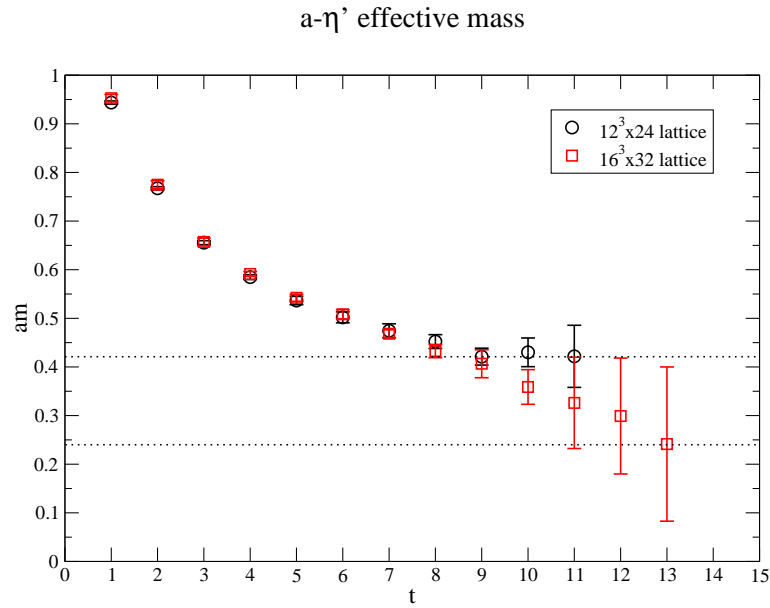


Figure 4.46: Comparison of the effective masses for the $a-\eta'$ on the large and small lattices for $\kappa = 0.194$.

see that for both masses, the onset of a plateau is delayed until extremely high Δt . The most obvious explanation is the contribution of higher states, which prompted us to devise alternative fitting procedures as described above. Nevertheless, we observe the onset of hugely differing plateaus for the two lattice sizes. Our analysis determined the $a-\eta'$ mass on the two lattices to be

$$am_{16^3} = 0.24(1) \quad \text{vs.} \quad am_{12^3} = 0.421(9) , \quad (4.53)$$

differing by approximately $\mathcal{O}(am)$ itself. This is even more surprising, as the assessment of the reliability of the individual values deemed them to be very sound. We are somewhat hesitant to attribute this difference completely to the finite volume effects when going from 12^3 to 16^3 lattices, since we do not observe such enormous effects in the other quantities. To get a clearer answer, however, one should employ Jacobi smearing or a similar method for future studies, in order to decrease the influence of the higher states and thus have a clearer view of a plateau for comparisons of effective masses.

Glueballs

In view of the tentative results obtained for the glueballs, especially in the case of the pseudo-scalar, we believe that a meaningful comparison between results from the small and the large lattice at $\kappa = 0.1940$ is not possible in this case. We saw from the determination of R_0 in Section 4.3 though, that purely gluonic states should not be affected dramatically by the finite volume of the lattice. However, this is a conjecture and it should be verified when reliable results on the glueballs are available.

	0^{++}	0^{-+}	$a-\eta'$	$a-f_0$	$\tilde{g}g$
0.1925.12c	0.53(10) [†]	0.80(10) ^{††}	0.52(10) [†]	<1.10(9) [†]	0.33(4)
0.1940.12c	0.40(11)	1.10(28) ^{††}	0.421(9)	0.3(3)	0.49(4)
0.1940.16c	0.52(1) ^{††}	0.69(14) ^{††}	0.24(1)	<0.78	0.43(1)
0.1955.12c	0.36(4)		0.24(2)	0.24(9)	0.35(4)

Table 4.9: Summary of spectrum results for the lightest states, (...) [†] were taken from [19]; (...) ^{††} should be regarded as upper bounds for the true value.

4.8 Summary and Discussion

We summarize this chapter by giving an overview of the results we obtained for the spectrum of the lightest particles in this calculation, collected in Table 4.9, and discussing their relevance. As we want to focus on the lightest states, we discard the results for the higher masses in the name of clarity. For a summary of all calculated masses, please refer to the appendix, Table B.1.

As we saw during our analysis, the particles obtained with the most confidence are the $a-\eta'$ and the gluino glue, here especially its $C_{\gamma_0}(\Delta t)$ component. For others, especially the $a-f_0$ and some glueballs, we found that various problems, such as small lattice size, low signal/noise ratios and other numerical issues, require a more cautious view of their estimates. We made clear that for the $a-f_0$ on the large lattice, we can only give an upper bound, while the true values for some masses in Table 4.9 are expected to be below the obtained. These, we marked by an additional superscript.

Graphing the results as a function of the hopping parameter κ in Figure 4.47, we get an overall picture of the lightest spectrum for this study. We find that at higher κ , two doublets of particles seem to form. The lighter of the two comprises the $a-\eta'$ and $a-f_0$, while the heavier one contains the gluino glue and the scalar glueball. The picture at $\kappa = 0.194$ and $\kappa = 0.1925$ is less clear. Making out multiplets here would amount to speculation, especially because of the larger error bars on the scalar glueball and the $a-f_0$. Generally, one can observe a slight trend to lighter masses for the bound states, as κ increases in the direction of the estimated κ_c . This is especially visible in the mass of the scalar glueball 0^{++} . However, in view of the comparably large error bars, it would be premature to interpret this as an effect that could be attributed to the soft breaking of SUSY, linear in $m_{\tilde{g}}$. In consequence, a linear extrapolation up to $\kappa = \kappa_c$ would not yield a reliable estimate for the states in the massless gluino limit. Note further, that we view the exact agreement of the $a-\eta'$ mass at $\kappa = 0.1955$ on the 12c lattice and at $\kappa = 0.194$ on the 16c lattice as coincidental.

Effective field theory calculations from [9, 10] predict the formation of two multiplets of similar mass (cf. Section 2.2). The lighter of the two contains the two glueballs 0^{++}

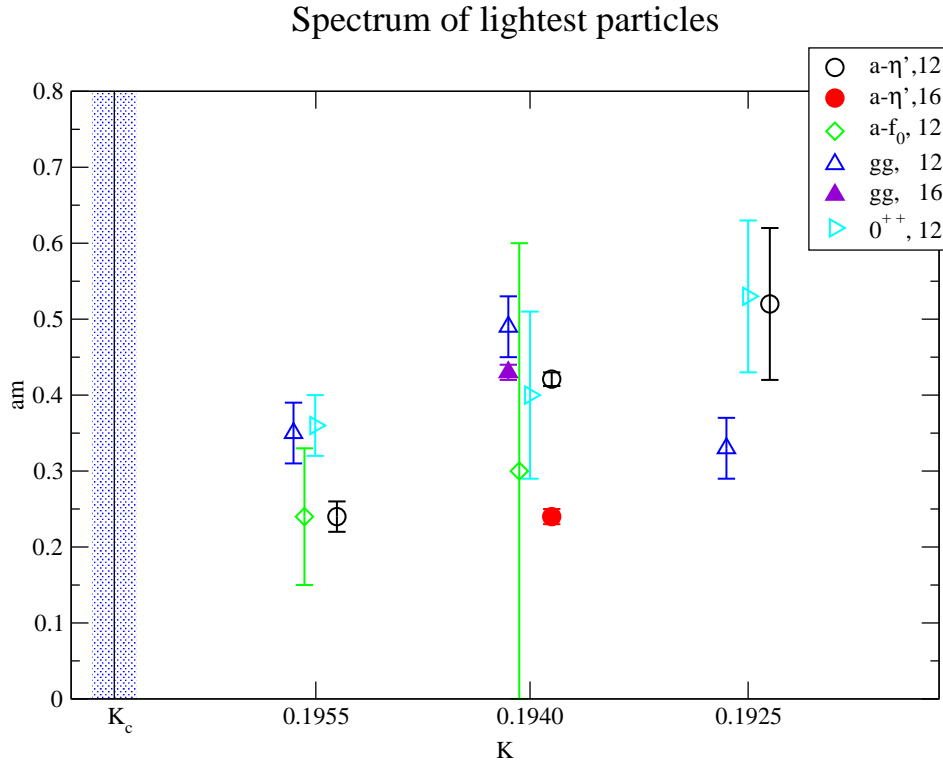


Figure 4.47: Overview of the lightest states as a function of κ^{-1} . Open symbols label results from the 12c lattice, filled symbols label 16c results. The shaded region marks the critical region where the gluino is expected to become massless.

and 0^{-+} and a gluino-gluon state $\tilde{g}g$ while the heavier should be made up of the adjoint mesons $a-\eta'$ and $a-f_0$ and another, heavier $\tilde{g}g$ [10]. Comparing this prediction with our results at $\kappa = 0.1955$ we do indeed find, as pointed out, a degenerate pair of adjoint mesons at $am \sim 0.24$ and additionally, an almost degenerate – within error – scalar glueball and gluino-gluon of larger mass, $am \sim 0.35$. At the risk of redundancy, we stress that these four values are determined with good confidence. We see, however, that the relative masses of the multiplets do not match the predicted form. In our view, the most probable reason is not that the lattice simulation produces results in contradiction to [9, 10], but rather that on the lattice a number of issues have to be addressed in order to rule out possible shortcomings.

Firstly, as we observed in Section 4.6, our “distance” to the massless gluino limit, as judged by Ward identities, seems to be non-negligible. It is entirely reasonable to expect individual masses to shift further, as we proceed further with $\kappa \rightarrow \kappa_c$. In particular, viewing the general trend of Figure 4.47, a possible scenario could even be the interchange or complete degeneracy of particle multiplets with respect to their masses. It was argued in [50] that a possible scenario is also a very small mass difference between the predicted multiplets. This would raise the principal question of the attainable resolution of mass extractions in a given lattice simulation.

Secondly, finite volume effects might be of influence for the values of the 1955.12c ensemble. As we found in Section 4.7, going to the larger lattice, the change in volume induces a drop in mass of approximately 10% for the gluino glue and of 50% for the $a-\eta'$. If these effects were present at $\kappa = 0.1955$, we would again expect an overall drop of values. Since the relative drops vary significantly, however, a reordering of the observed particle multiplets is also possible from this perspective.

And thirdly, for a final statement, a continuum extrapolation would have to be performed. This is currently not within reach of the project, as it would entail a complete spectrum analysis at different couplings β and the subsequent extrapolation to $\beta \rightarrow 0$. However, we do know from the numerical validity of the supersymmetric Ward identity that in the continuum limit, we arrive at a supersymmetric theory. This knowledge enables us to backup our results as nevertheless being indicative of the continuum supersymmetric theory.

Finally, comparing our findings with previous results from the project [18], we find a disagreement with the observed optimistic scenario therein. In [18] two multiplets were determined: a lighter containing the glueball 0^{++} , the $a-\eta'$ and a light gluino-gluon and a heavier multiplet containing the 0^{-+} glueball, the $a-f_0$ and a heavier gluino-gluon state. With the experience obtained throughout this work and especially in comparison with the results it produced with their varying quality, we conclude that the previous picture was to some degree influenced by the effects outlined above.

Chapter 5

Conclusions and Outlook

We want to conclude this study by providing an overview of the work and based on that, recommend specific directions for future research to improve results.

We examined the spectrum of $N = 1$ Super Yang Mills Theory on the lattice in the Curci and Veneziano formulation [14]. We aimed to obtain high quality results for the particles of the spectrum proposed in [9, 10] in order to compare these with the predicted form. We used several ensembles of configurations, differing in the hopping parameter κ and in lattice size.

To determine the masses of the adjoint mesons, we needed a viable method to estimate the disconnected part of the correlation function. A careful analysis of the previously employed volume source technique revealed the existence of a yet unaccounted for erroneous term. Within a numerical assessment, it was found to produce an immeasurable effect in the determination of the $a-\eta'$ masses, while at the examined precision, a clear comparison for the $a-f_0$ could not be made. The check itself was done by applying the VST in a novel way, namely as a variant of a stochastic estimator. By performing large enough $N_{est}^{VST} > 1$ estimates per configuration, we were able to decouple the Monte-Carlo errors of the simulation from the statistical errors made by the estimation of the two-loop graph. Increasing that value significantly beyond 15 should increase the precision on the error assessment to a satisfactory level. A further study is warranted for two reasons. Firstly, a considerable volume of lattice literature is based on the traditional use of the VST. It should be of interest to the community, exactly how to judge these results. Secondly, the correctly used VST could be an easy to implement and computationally cheaper alternative to other costly methods of estimating the two-loop graph. One should benchmark these against each other.

For the actual investigation of the adjoint mesons, we chose stochastic estimators with complex \mathbb{Z}_2 noise. It was found that $N_{est} \sim 150$ estimates produced an acceptable

precision for our ensembles. However, in the case of the $a-f_0$ a build up of numerical errors was observed. This was attributed to the choice of 32bit machine precision in combination with large lattices and the fact that the correlation is a large number obtained by the summation of small quantities. Increasing the numerical precision and an increase of N_{est} should mitigate that problem in the future. It is of great interest to obtain reliable results for the $a-f_0$ on large lattices, since it is an integral part of the predicted multiplet formation. In contrast, the $a-\eta'$ belongs to the best determined particles. Also, for the adjoint mesons, a smearing scheme, such as Jacobi smearing, should be used. This would lead to cleaner signal for the lowest mass and therefore reduce the reliance of their mass calculations on fitting techniques, thus giving cleaner results from a theoretical point of view.

The results from the gluino glue particle underlined the need for larger lattices. In some cases it was not possible to separate the higher states from the lowest in the correlator on the small lattices. From the large lattice we obtained an impressive confirmation of this problem, where it was possible to witness the higher states dying off by the use of effective masses, i.e. without fitting, leaving the lowest lying state to form a plateau. It should be most interesting to see result from the large lattice at $\kappa = 0.1955$ which is currently in production.

The glueballs proved to be the hardest to measure, due to a low signal/noise ratio. On most ensembles, mass fits produced no reliable estimates. The estimates were nevertheless obtained by using various degrees of smearing and calculating effective masses. Here, there are two directions one could pursue to improve on our results. One, the most straightforward, would be the use of variational methods [51] applied to smearing and to linear combinations of different operators. The main idea is to maximize the overlap for a given state by directly determining the most suitable linear combination of operators and smearing parameters. This should help significantly in getting better signals. The second, more dramatic option would be to explore the possibility of using anisotropic lattices. These provide a higher resolution in the time direction and therefore, independently of the noise present in the simulation, more data points for the correlation function before the signal disappears. In pure glueball calculations in lattice gauge theory, this option is widely used [35].

In passing, we analyzed the supersymmetric Ward identities on the large lattice along the lines of [20]. We found the results to be consistent with the previous work and therefore the breaking pattern of SUSY when formulated on the lattice. From these results, we estimated the critical hopping parameter κ_c and concluded by the use of QCD analogies, that $\kappa = 0.194$ is not near the $m_{\tilde{g}} \rightarrow 0$ limit since as in QCD units, the gluino mass is of the order of the strange quark mass. We therefore reiterate the need to go to larger κ on larger lattices. The current production run serves this purpose.

Comparing mass estimates at $\kappa = 0.194$ on different lattice sizes revealed considerable

finite size effects, ranging from 10 to 50%, the latter case being the $a\text{-}\eta'$. This somewhat dramatic drop is surprisingly large, reinforcing the case for larger lattices.

Finally, when bringing all the pieces together, we formulated our primary result, an overview of the spectrum of lightest particles in Table 4.9 and the corresponding Figure 4.47. We found the results to deviate from the predicted picture of [10] as we observe two doublets of lightest particles, one consisting of the adjoint mesons with a mass of $am \sim 0.24$, and the other containing the scalar glueball and a gluino glue with mass $am \sim 0.35$. We concluded in view of the analysis, that at the current parameters, the deviation should not be alarming. We outlined the possible reasons for the missing agreement. It was also found, that our results do not match the overall picture found in [18].

We conclude by restating that the next step should be the determination of the spectrum on the larger lattice at $\kappa = 0.1955$. The lattice size of $16^3 \times 32$ seems to be large enough under the criteria developed here. Prior to that, reliable results on the lightest masses for the glueballs, especially the pseudo-scalar, for the already available ensemble would be of great interest. This should be complemented by a reliable determination of the $a\text{-}f_0$, since firm statements about lattice results vs. continuum predictions can only be formulated on the basis of reliable estimates on all particles of the predicted multiplet.

Appendix A

Conventions and Methods

In this appendix we collect various notations, conventions and methods used in our work. On a fundamental level we assumed throughout that

$$2 + 2 = 4 \quad \text{and} \quad e^{i\pi} + 1 = 0 \quad (\text{A.1})$$

hold.

A.1 Gamma Matrices

We define our Euclidean γ -matrices to be in the chiral representation

$$\gamma_0 = \begin{pmatrix} 0 & \mathbb{1} \\ \mathbb{1} & 0 \end{pmatrix}, \gamma_k = -i \begin{pmatrix} 0 & \sigma_k \\ -\sigma_k & 0 \end{pmatrix}, \quad (\text{A.2})$$

where $\sigma_k = \tau_k$ are the venerable Pauli matrices

$$\sigma_1 = \begin{pmatrix} 0 & 1 \\ 1 & 0 \end{pmatrix}, \quad \sigma_2 = \begin{pmatrix} 0 & -i \\ i & 0 \end{pmatrix}, \quad \sigma_3 = \begin{pmatrix} 1 & 0 \\ 0 & -1 \end{pmatrix}. \quad (\text{A.3})$$

The Euclidean matrices fulfill

$$\gamma_\mu = \gamma_\mu^\dagger \quad (\text{A.4})$$

and

$$\{\gamma_\mu, \gamma_\nu\} = 2\delta_{\mu\nu}. \quad (\text{A.5})$$

We also define the following matrices to be

$$\gamma_5 = \prod_{i=0}^3 \gamma_i = \begin{pmatrix} \mathbb{1} & 0 \\ 0 & -\mathbb{1} \end{pmatrix} \quad (\text{A.6})$$

$$\mathcal{C} = \gamma_0 \gamma_2 = i \begin{pmatrix} \sigma_2 & 0 \\ 0 & -\sigma_2 \end{pmatrix} \quad (\text{A.7})$$

$$\sigma_{\mu\nu} \equiv \frac{1}{2} [\gamma_\mu, \gamma_\nu] . \quad (\text{A.8})$$

The γ_5 has the properties

$$\{\gamma_5, \gamma_\mu\} = 0 , \quad (\gamma_5)^2 = \mathbb{1} , \quad \gamma_5^\dagger = \gamma_5 , \quad (\text{A.9})$$

while the charge conjugation matrix obeys the relations

$$\mathcal{C}^{-1} = -\mathcal{C} = \mathcal{C}^T , \quad \mathcal{C}^{-1} \gamma_\mu \mathcal{C} = -\gamma_\mu^T , \quad (\text{A.10})$$

and finally the tensor $\sigma_{\mu\nu}$ obeys

$$\sigma_{\mu\nu}^\dagger = -\sigma_{\mu\nu} . \quad (\text{A.11})$$

A.2 Majorana Fermions

The Majorana condition for a spinor reads

$$\lambda^c = \lambda = \mathcal{C} \bar{\lambda}^T \quad \Leftrightarrow \quad \bar{\lambda} = \lambda^T \mathcal{C} . \quad (\text{A.12})$$

We can work out the Majorana fermion matrix Q defined in equation (3.10) to have the following convenient properties

$$\mathcal{C}^{-1} Q \mathcal{C} = Q^T \quad \text{and} \quad \gamma_5 Q^\dagger \gamma_5 = Q , \quad (\text{A.13})$$

which also hold for its inverse, Q^{-1} . This implies a linear dependence of entries in the fermion matrix. The redundancy can be used when calculating propagators to cut down the number of necessary inversions. In general, Q^{-1} therefore has the following form

$$Q^{-1} = \begin{pmatrix} a_{11} & -a_{21}^* & a_{13} & -a_{23}^* \\ a_{21} & a_{11}^* & a_{23} & a_{13}^* \\ a_{31} & -a_{41}^* & a_{33} & -a_{43}^* \\ a_{41} & a_{31}^* & a_{43} & a_{33}^* \end{pmatrix} , \quad (\text{A.14})$$

where the entries in the second and fourth column can be read off from the first and third columns respectively.

A.3 Smearing Techniques

Smearing seeks to increase the overlap of a given operator with the actual wave function of the particle one wants to measure, thus achieving a better signal/noise ratio and the reduction of contamination by higher states in the correlation function. On the lattice, particle masses are determined by investigating the fall-off of correlation functions of an operator for increasing time separation. At higher temporal separations, only the lightest state survives, rendering a plateau. The onset of this plateau is also determined by the relative amplitudes of the states in the linear combination of states (3.77). By smearing, we alter the coefficients of the series, such that the amplitude for the lowest mass is increased with respect to the others. This should then lead to an earlier plateau formation in the mass calculations and a preciser overall signal, thus increasing the signal/noise ratio.

There are several iterative smearing schemes available. We opted for the APE scheme [52] for gluonic and Jacobi smearing [53] for fermionic operators.

APE Smearing

At every iteration, APE smearing substitutes a given link $U_\mu(x)$ with the sum of itself and the sum of space-like staples surrounding it, perpendicular to its direction μ

$$U'_\mu(x) = \mathcal{P}_{SU(2)} \left[U_\mu(x) + \epsilon_{APE} \sum_{\substack{\nu=\pm 1 \\ \nu \neq \mu}}^{\pm 3} U_\nu^\dagger(x + \hat{\mu}) U_\mu(x + \hat{\nu}) U_\nu(x) \right]. \quad (\text{A.15})$$

The operator $\mathcal{P}_{SU(2)}$ projects the resulting link back into the $SU(2)$ group. Let $\bar{U}'_\mu(x) \notin SU(2)$ be the non-projected result after a smearing step. The projection is achieved by

$$\mathcal{P}_{SU(2)}[\bar{U}'_\mu(x)] = \frac{\bar{U}'_\mu(x)}{\sqrt{\frac{1}{2} \text{Tr}[\bar{U}'_\mu(x)^\dagger \bar{U}'_\mu(x)]}} \in SU(2). \quad (\text{A.16})$$

For gluonic operators, the algorithm is applied N_{APE} times to the complete lattice. It can easily be checked that this algorithm is gauge-invariant. At too high N_{APE} or ϵ_{APE} it is possible for any correlation to be washed out completely. We can qualitatively appreciate that such a scheme increases the spatial size of the object to be correlated. The physical picture one has, is that through the method, the physical wave function of, for example, a glueball is approximated more correctly.

Jacobi Smearing

From the point of view of analytical calculations, the easiest method to construct a source, i.e. a point source, does not serve the lattice method very well. The true wave function of a particle is again an extended object. By using the solution to the three dimensional Klein-Gordon equation as a guide, a spinor $\lambda(\vec{x}, t)$ is smeared as

$$\bar{\lambda}(\vec{x}, t) = \sum_{\vec{y}} F(\vec{x}, \vec{y}) \lambda(\vec{y}, t) \quad (\text{A.17})$$

where the kernel $F(\vec{x}, \vec{y})$ is defined through

$$F(\vec{x}, \vec{y}) = \delta^{ab} \delta_{\vec{x}, \vec{y}} + \sum_{i=1}^{N_{Jacobi}} \left(\kappa_{Jacobi} \sum_{\nu=1}^3 [\delta_{\vec{x}+\hat{\nu}, \vec{y}} U_{\nu}^{ab}(x) + \delta_{\vec{x}, \vec{y}+\hat{\nu}} U_{\nu}^{ab}(x)^{\dagger}] \right)^i, \quad (\text{A.18})$$

which amounts to the solution kernel to the Klein-Gordon equation for small κ_{Jacobi} and $N_{Jacobi} \rightarrow \infty$. On the lattice, the two parameters have to be tuned in order to get optimal results for the investigated correlators. Again, this scheme is gauge-invariant.

A.4 Combining Estimates

Sometimes one has a series of estimates with errors $x_i \pm \sigma_i$ where $i \in \{1, \dots, N\}$ one wants to average over, as in the case of N ensembles of lattices updated independently in parallel. The Maximum Likelihood Method tells us that under the assumption of Gaussian statistics, the correct way to combine the measurements is [46]

$$\bar{x} = \frac{\sum_i \frac{x_i}{\sigma_i^2}}{\sum_i \frac{1}{\sigma_i^2}}, \quad (\text{A.19})$$

and using the linear propagation of errors to calculate the variance:

$$\bar{\sigma}_x^2 = \frac{1}{\sum_i \frac{1}{\sigma_i^2}}. \quad (\text{A.20})$$

The assumption of Gaussian statistics is also justified in the context of lattice gauge theory if the estimated errors σ_i were obtained by Jackknife analysis, see 3.2.2 for details.

Appendix B

Overview of Spectrum Results

	0^{++}	0^{-+}	$a-\eta'$	$a-f_0$	$\tilde{g}g_{\gamma_0}$	$\tilde{g}g_{\mathbb{1}}$
0.1925.12c	0.53(10) [†]	0.80(10) ^{††}	0.52(10) [†]	<1.10(9) [†]	0.33(4)	
			1.09(5) [†]		0.95(3)	0.88(1)
0.1940.12c	0.40(11)	1.10(28) ^{††}	0.421(9)	0.3(3)	0.49(4)	
			0.99(1)		0.85(2)	0.80(2)
0.1940.16c	0.52(1) ^{††}	0.69(14) ^{††}	0.24(1)	<0.78	0.43(1)	0.40(7)
			0.65(2)		0.85(2)	
0.1955.12c	0.36(4)		0.24(2)	0.24(9)	0.35(4)	
			0.81(6)			0.66(4)

Table B.1: Summary of spectrum results for all states measured. The first/second row of an ensemble contains the lower/higher mass, if determination was possible. The values marked by (...) [†] were taken from [19] for reference while (...) ^{††} should be considered as upper bounds on the lowest masses.

Bibliography

- [1] N. Arkani-Hamed, A. G. Cohen and H. Georgi, Phys. Lett. B **513** (2001) 232 [arXiv:hep-ph/0105239].
- [2] H. P. Nilles, Phys. Rept. **110** (1984) 1.
- [3] M. Pospelov and A. Ritz, Nucl. Phys. B **573** (2000) 177 [arXiv:hep-ph/9908508].
- [4] D. B. Kaplan and A. V. Manohar, Phys. Rev. Lett. **56** (1986) 2004.
- [5] D. R. Nelson, G. T. Fleming and G. W. Kilcup, Phys. Rev. Lett. **90** (2003) 021601 [arXiv:hep-lat/0112029].
- [6] M. B. Green, J. H. Schwarz and E. Witten, “Superstring Theory. Vol. 1: Introduction”, Cambridge, UK: Univ. Pr. (1987).
- [7] R. Haag, J. T. Lopuszanski and M. Sohnius, Nucl. Phys. B **88** (1975) 257.
- [8] S. Weinberg, “The Quantum Theory Of Fields. Vol. 3: Supersymmetry”, Cambridge, UK: Univ. Pr. (2000).
- [9] G. Veneziano and S. Yankielowicz, Phys. Lett. B **113** (1982) 231.
- [10] G. R. Farrar, G. Gabadadze and M. Schwetz, Phys. Rev. D **58** (1998) 015009 [arXiv:hep-th/9711166].
- [11] K. G. Wilson, Phys. Rev. D **10** (1974) 2445.
- [12] M. Lüscher, Nucl. Phys. B **549** (1999) 295 [arXiv:hep-lat/9811032].
- [13] H. Neuberger, Phys. Lett. B **417** (1998) 141 [arXiv:hep-lat/9707022].
- [14] G. Curci and G. Veneziano, Nucl. Phys. B **292** (1987) 555.
- [15] I. Montvay, Nucl. Phys. B **466** (1996) 259 [arXiv:hep-lat/9510042].
- [16] I. Montvay, Int. J. Mod. Phys. A **17** (2002) 2377 [arXiv:hep-lat/0112007].

- [17] R. Kirchner, S. Luckmann, I. Montvay, K. Spanderen and J. Westphalen [DESY-Münster Collaboration], Nucl. Phys. Proc. Suppl. **73** (1999) 828 [arXiv:hep-lat/9808024].
- [18] I. Campos *et al.* [DESY-Münster Collaboration], Eur. Phys. J. C **11** (1999) 507 [arXiv:hep-lat/9903014].
- [19] R. Kirchner, DESY-THESIS-2000-043.
- [20] F. Farchioni *et al.*, Nucl. Phys. Proc. Suppl. **106**, 941 (2002).
- [21] F. Farchioni *et al.* [DESY-Münster-Roma Collaboration], Eur. Phys. J. C **23** (2002) 719 [arXiv:hep-lat/0111008].
- [22] S. Luckmann, PhD-thesis, Münster, 2001.
- [23] R. Peetz, F. Farchioni, C. Gebert and G. Münster, Nucl. Phys. Proc. Suppl. **119** (2003) 912 [arXiv:hep-lat/0209065].
- [24] R. Kirchner, I. Montvay, J. Westphalen, S. Luckmann and K. Spanderen [DESY-Münster Collaboration], Phys. Lett. B **446** (1999) 209 [arXiv:hep-lat/9810062].
- [25] S. Dimopoulos, Nucl. Phys. Proc. Suppl. **101** (2001) 183 [arXiv:hep-th/0105034].
- [26] V. A. Novikov, M. A. Shifman, A. I. Vainshtein and V. I. Zakharov, Nucl. Phys. B **229** (1983) 381.
- [27] H. B. Nielsen and M. Ninomiya, Nucl. Phys. B **185** (1981) 20 [Erratum-ibid. B **195** (1982) 541]. Phys. Lett. B **105** (1981) 219.
- [28] E. Witten, Phys. Lett. B **117** (1982) 324.
- [29] I. Montvay and G. Münster, “Quantum Fields On A Lattice,”, Cambridge, UK: Univ. Pr. (1994).
- [30] R. G. Edwards, U. M. Heller and R. Narayanan, Nucl. Phys. B **535** (1998) 403 [arXiv:hep-lat/9802016].
- [31] R. G. Edwards, U. M. Heller and T. R. Klassen, Nucl. Phys. B **517** (1998) 377 [arXiv:hep-lat/9711003].
- [32] C. Michael, Phys. Lett. B **283** (1992) 103 [arXiv:hep-lat/9205010].
- [33] R. Sommer, Nucl. Phys. B **411** (1994) 839 [arXiv:hep-lat/9310022].
- [34] T. Kalkreuter and H. Simma, Comput. Phys. Commun. **93** (1996) 33 [arXiv:hep-lat/9507023].
- [35] C. J. Morningstar and M. J. Peardon, Phys. Rev. D **60** (1999) 034509 [arXiv:hep-lat/9901004].

- [36] B. Berg, A. Billoire Nucl. Phys. B **221** (1983) 109.
- [37] H. Neff, N. Eicker, T. Lippert, J. W. Negele and K. Schilling, Phys. Rev. D **64** (2001) 114509 [arXiv:hep-lat/0106016].
- [38] S. Elitzur, Phys. Rev. D **12** (1975) 3978.
- [39] Y. Kuramashi, M. Fukugita, H. Mino, M. Okawa and A. Ukawa, Phys. Rev. Lett. **72** (1994) 3448.
- [40] A. Donini, M. Guagnelli, P. Hernandez and A. Vladikas, Nucl. Phys. B **523** (1998) 529 [arXiv:hep-lat/9710065].
- [41] Y. Taniguchi, Phys. Rev. D **63** (2001) 014502 [Chin. J. Phys. **38** (2000) 655] [arXiv:hep-lat/9906026].
- [42] T. Galla, Diploma thesis, Münster, 1999.
- [43] M. Bochicchio, L. Maiani, G. Martinelli, G. C. Rossi and M. Testa, Nucl. Phys. B **262** (1985) 331.
- [44] M. Testa, JHEP **9804** (1998) 002 [arXiv:hep-th/9803147].
- [45] C. McNeile and C. Michael [UKQCD Collaboration], Phys. Rev. D **63**, 114503 (2001) [arXiv:hep-lat/0010019].
- [46] W. H. Press, *et al.*, “Numerical Recipes in C: the art of scientific computing,” Cambridge, UK: Univ. Pr. (1992).
- [47] GNU Scientific Library, <http://www.gnu.org/software/gsl/>
- [48] V. I. Lesk *et al.* [CP-PACS Collaboration], Nucl. Phys. Proc. Suppl. **119** (2003) 691 [arXiv:hep-lat/0211041].
- [49] M. Lüscher, DESY-88-156 *Lectures given at Summer School 'Fields, Strings and Critical Phenomena', Les Houches, France, Jun 28 - Aug 5, 1988*
- [50] D. G. Cerdeno, A. Knauf and J. Louis, Eur. Phys. J. C **31** (2003) 415 [arXiv:hep-th/0307198].
- [51] M. Lüscher and U. Wolff, Nucl. Phys. B **339** (1990) 222.
- [52] M. Albanese *et al.* [APE Collaboration], Phys. Lett. B **192** (1987) 163.
- [53] C. R. Allton *et al.* [UKQCD Collaboration], Phys. Rev. D **47** (1993) 5128 [arXiv:hep-lat/9303009].

Curriculum Vitae

<i>Name:</i>	Roland Peetz	
<i>Geburtsdatum:</i>	18.3.1974	
<i>Geburtsort:</i>	Wrexham(GB)	
<i>Familienstand:</i>	ledig	
<i>Ausbildung:</i>	8/1980-7/1984	Grundschule am Falkenberg, Norderstedt
	8/1984-7/1993	Gymnasium Harksheide, Norderstedt
	17.6.1993	Abitur
	7/1993-6/1994	Wehrdienst, Marine
<i>Studium:</i>	10/1994-8/1997	Universität Hamburg, Studiengang Physik-Diplom
	22.8.1996	Vordiplom Physik
	9/1997-12/2000	Ohio State University, Graduate School, Dept. of Physics
	8.12.2000	Master of Science, Physics Thesis: <i>Non-perturbative quark-mass renormalization in full Lattice QCD</i>
<i>Tätigkeiten:</i>	2/1996-8/1997	Stud. Hilfskraft am Institut für Meereskunde, Universität Hamburg
	6/1998 - 12/2000	Graduate Teaching und Research Assistant Dept. of Physics, OSU und Ohio Supercomputer Center
	1/2001 - 4/2001	Wissenschaftl. Hilfskraft am Institut für theoretische Physik der WWU Münster
	seit 5/2001	Wissenschaftl. Mitarbeiter
<i>Promotions- studiengang</i>	seit 4/2000	Physik
<i>Beginn der Dissertation</i>	1/2001	bei Prof. Dr. G. Münster, Institut für theoretische Physik der WWU Münster

Acknowledgments

I would like to take the opportunity to offer thanks to the people, who made this work possible:

- My adviser Prof. G. Münster, for proposing such an interesting project. His continuous support and encouragement, the many interesting and enlightening discussions and the pleasant atmosphere were essential ingredients to this thesis.
- Very special thanks go to my collaborator, knowledge tank, mentor and guide to Bella Italia, Federico Farchioni. Without his enthusiasm, the countless hours spent in his office patiently answering random questions and his experience and finally the application of the Farchioni-Filter to the draft, there would be many big, blank and wrong spots in this work.
- Claus Gebert, who provided the excellent simulation code and at times very customer friendly and competent user support.
- The Mitbewohner of our Office-WG, Eicke Ruthotto and Andre Ewering, for the great atmosphere and the many hours we spent concentrating on not thinking about physics and research, but rising to more advanced topics like brewing beer or the currently best (and worst) deals on ebay.
- Federico Farchioni, Margaret Peetz and Nicole Thomas and for careful proofreading the various drafts of the manuscript. Any remaining mistakes are of course entirely attributable to the author.
- My parents Margaret and Rudolf Peetz for their unconditional and continuous support and interest during my studies.
- And finally, Nicole Thomas, for just being there, supporting and loving me, even at times, thousands of miles away.

